STARS

Electronic Theses and Dissertations, 2020-

2021

High-Density Neurochemical Microelectrode Array to Monitor Neurotransmitter Secretion

Kevin White
University of Central Florida

Showcase of Text, Archives, Research & Scholarship

HIGH-DENSITY NEUROCHEMICAL MICROELECTRODE ARRAY TO MONITOR
NEUROTRANSMITTER SECRETION

by

KEVIN A. WHITE
B.S. in Electrical Engineering University of Central Florida, 2016
M.S. in Electrical Engineering University of Central Florida, 2019

A dissertation submitted in partial fulfillment of the requirements
for the degree of Doctor of Philosophy
in the Department of Electrical and Computer Engineering
in the College of Engineering and Computer Science
at the University of Central Florida
Orlando, Florida

Summer Term
2021

Major Professor: Brian N. Kim

ABSTRACT

Neuronal exocytosis facilitates the propagation of information through the nervous system pertaining to bodily function, memory, and emotions. Using amperometry, an electrochemical technique that directly detects electroactive molecules, the sub-millisecond dynamics of exocytosis are revealed and the modulation of neurotransmitter secretion due to neurodegenerative diseases or pharmacological treatments can be studied. The method of detection using amperometry is the exchange of electrons due to a redox reaction at an electrochemically sensitive electrode. As electroactive molecules, such as dopamine, undergo oxidation, electrons are released from the molecule to the electrode and an oxidation current is generated and recorded. Despite the significance of traditional single-cell amperometry, it is a costly, labor-intensive, and low-throughput, procedure. The focus of this dissertation is the development of a monolithic CMOS-based neurochemical sensing system that can provide a high-throughput of up to 1024 single-cell recordings in a single experiment, significantly reducing the number of experiments required for studying the effects of neurodegenerative diseases or new pharmacological treatments on the exocytosis process. The neurochemical detection system detailed in this dissertation is based on a CMOS amplifier array that contains 1024 independent electrode-amplifier units, each of which contains a transimpedance amplifier with comparable noise performance to a high-quality electrophysiology amplifier that is used for traditional single-cell amperometry. Using this novel technology, single exocytosis events are monitored simultaneously from numerous single-cells in experiments to reveal the secretion characteristics from groups of cells before and after pharmacological treatments which target the modulation of neurotransmitters in the brain, such as drugs for depression or Parkinson's disease.

Dedicated to my father.

ACKNOWLEDGMENTS

I would like to thank my advisor. Dr. Brian N. Kim, for his support, guidance, and patience.

TABLE OF CONTENTS

vii

LIST OF FIGURES

LIST OF TABLES

LIST OF ABBREVIATIONS

ABS .... Acrylonitrile Butadiene Styrene

ADC .... Analog-to-Digital Converter

ANN .... Artificial Neural Networks

API .... Application Programming Interface

BNN .... Biological Neural Network

CDS .... Correlated Double Sampling

CFE .... Carbon Fiber Electrodes

CV .... Cyclic Voltammetry

CMOS .... Complementary Metal-Oxide-Semiconductor

DI .... Deionized

DIC .... Differential Interference Contract

DIO .... Digital Inputs and Outputs

ESD .... Electrostatic Discharge

FIFO .... First-In, First-Out

FPGA .... Field-Programmable Gate Array

MEA .... Microelectrode Array

NSD .... Noise Spectral Density

OPA .... Operational Amplifier

CHAPTER 1: INTRODUCTION

1.1   The Significance of Exocytosis

Chemical transmissions at the synapses are an essential component of neurons, and it allows information to travel throughout the nervous system for body functions, memories, and emotions. In secretory cells, neurotransmitters are membrane-bound at high concentration in secretory vesicles. Neuronal excitation causes vesicle fusion with the plasma membrane, also known as exocytosis, in which the membrane-bound neurotransmitters are released in quantal events through a fusion pore, a nanoscopic channel that connects the vesicular lumen to the cell's exterior (Fig. 1.1)[*].
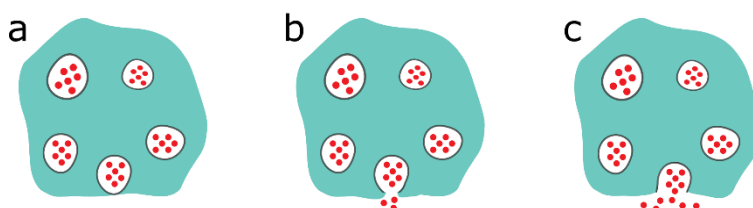
Figure 1.1: Process of exocytosis. (a) A vesicle fuses with the cell membrane and prepares to release neurotransmitters. (b) The fusion pore is formed and the membrane can expand, enabling secretion of the vesicle's quantal content. (c) The membrane fully expands and the neurotransmitters are released.

Neurotransmitter secretion is modulated by molecular manipulations related to neurological diseases [1] and drug treatments [2]. For example, Parkinson's disease can considerably reduce the quantity of dopamine release [3] while the drug L-Dopa can increase the amount of secretion [2]. By studying the secretion from individual vesicles, we gain rich information regarding the dynamics of membrane fusion [4], obtain insight into the mechanisms

---

[*] In this chapter, we use material published in Nature Communications, 2021 [114], IEEE Transactions on Biomedical Circuits and Systems 2018, [24], and IEEE Sensors Journal, 2020 [115]

of neurological diseases at the molecular level [5], and learn both the desirable and undesirable side effects of drug treatments [6], [7]. The quantal release of neurotransmitters is a fast event, typically occurs in milliseconds or less, and the quantal size is small, containing less than attomoles of neurotransmitter molecules per quanta (vesicle) [5], [8].

1.2   Electrochemical Monitoring of Exocytosis using CFE Amperometry

The amperometry technique is an electrochemical method which uses a microelectrode to measure the electrochemical current generated by the electroactive molecules, including dopamine, serotonin, epinephrine, and norepinephrine at an electrode's surface [9]. Amperometry is widely used to monitor neurotransmitter release with high temporal resolution [4] as it can reveal the sub-millisecond dynamics of neurotransmitter release. Thusly, the technique can be used to reveal the rich details of individual quantal release including quantal size (# of molecules per vesicle), frequency, as well as the kinetics of vesicle fusion [10].

The method of detection for amperometry is through the oxidation of an electroactive molecule at an electrode. Oxidation is the process of electroactive molecules, such as the neurotransmitters dopamine, epinephrine, norepinephrine, and serotonin, releasing electrons into the electrode, generating picoampere currents that can be measured with high-quality low-noise amplifiers as illustrated in Fig. 1.2. Cyclic voltammetry is also a commonly used electrochemical method which is capable of measuring neurotransmitter levels, but this technique suffers from a lower temporal resolution compared to amperometry and is adequate for detecting the neurotransmitter level in a slow dynamic system. Conventionally, amperometric recordings are performed by placing a carbon fiber electrode (CFE) in close proximity to a single cell, such as a

dopaminergic neuron, chromaffin cell, or pheochromocytoma (PC-12) cell. This electrophysiological method is called single-cell amperometry and an example recording of a single quantal event is illustrated in Fig. 1.3.
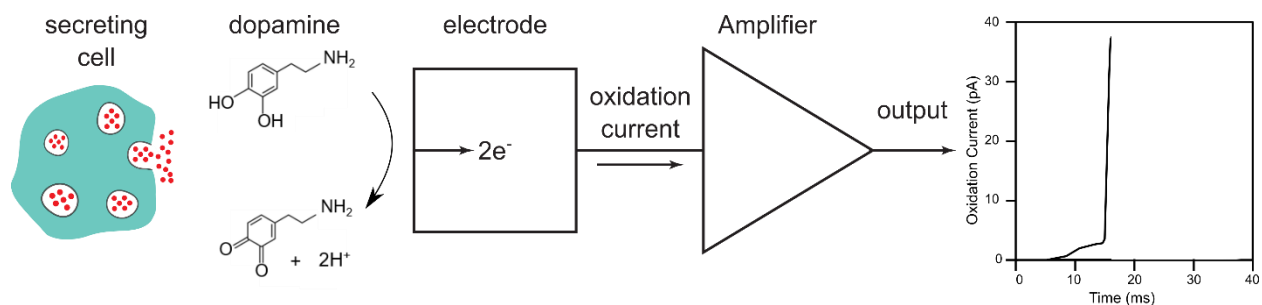
Figure 1.2: Illustration of dopamine detection by oxidation at an electrochemical electrode. Dopamine secreted from the secretory cell releases 2 electrons per molecule. The released electrons from numerous molecules create an oxidation current. The oxidation current is processed by a high-quality low-noise amplifier and outputs a readable signal.

Amperometric recordings using a CFE have been imperative in studying the fundamental mechanism of vesicle fusion as well as the molecular effects of disease/treatment modulations over many decades. A phenomenon of incomplete exocytosis events allowing recycling of vesicles for rapid reuse is called 'kiss-and-run' and has been studied extensively as this secretion regulation provides insights into neuronal communications and potentially the mechanisms of neuronal plasticity [11]. The study of this phenomenon is enabled by amperometry as these events require an enhanced temporal resolution to study these millisecond scale kiss-and-run phenomena at a single vesicle scale [8], [12]–[16]. Using traditional amperometry techniques researchers have discovered that extracellular calcium concentration directly affects the frequency of kiss-and-run events [12], and more recently discovered a relationship between the polymerization of the actin protein and the fraction of secreted neurotransmitters during kiss-and-run events [16]. Another protein that has been studied extensively is the SNAP-25 protein, part of the SNARE protein

complex, at it is directly related to the intracellular membrane fusion required for neurotransmitter secretion from intracellular vesicles [6], [7], [17]. Using amperometry, the C-terminus in SNAP-25 is revealed to modulate the rate at which neurotransmitters are secreted during exocytosis events and a lack of the C-terminus leads to prolonged secretion events [17]. Another protein that has been studied is alpha-synuclein as it has been implicated in the pathogenesis of Parkinson's disease and has been found to reduce the frequency of exocytotic events by inhibition of vesicle priming for fusion with the cellular membrane [18]. Amperometry is also used to study the effects of various treatments that modulate exocytosis characteristics, such as the effects of morphine and curcuminoids. A study has revealed that the serotonin secreted from mast cells is reduced from mast cells due to sickle cell disease and exposure to morphine, which is used to treat pain due to sickle cell disease, nearly reverses the modulation of serotonin release in the mast cells due to the disease [19]. Another study has examined the effects of curcuminoids, which have been thought to have potential therapeutic applications for neurodegenerative diseases [20]. This study has revealed the effects of curcumin and bisdemethoxycurcumin, which exist in turmeric spice, and have found that bisdemethoxycurcumin reduces the quantal size of the exocytotic events while curcumin accelerates the exocytotic process [21]. In addition to treatments for neurodegenerative diseases, amperometry is used to study/monitor biomarkers that can reveal signs of a neurological disease. Amperometry has enabled the study of the concentration of nitric oxide, which is linked to neuronal cell death, in a rat's brain by providing the high sensitivity and temporal response required to monitor the highly reactive molecule in its own physiological environment [22]. To monitor the concentration of neurotransmitters, such as acetylcholine, in vivo to enhance therapies
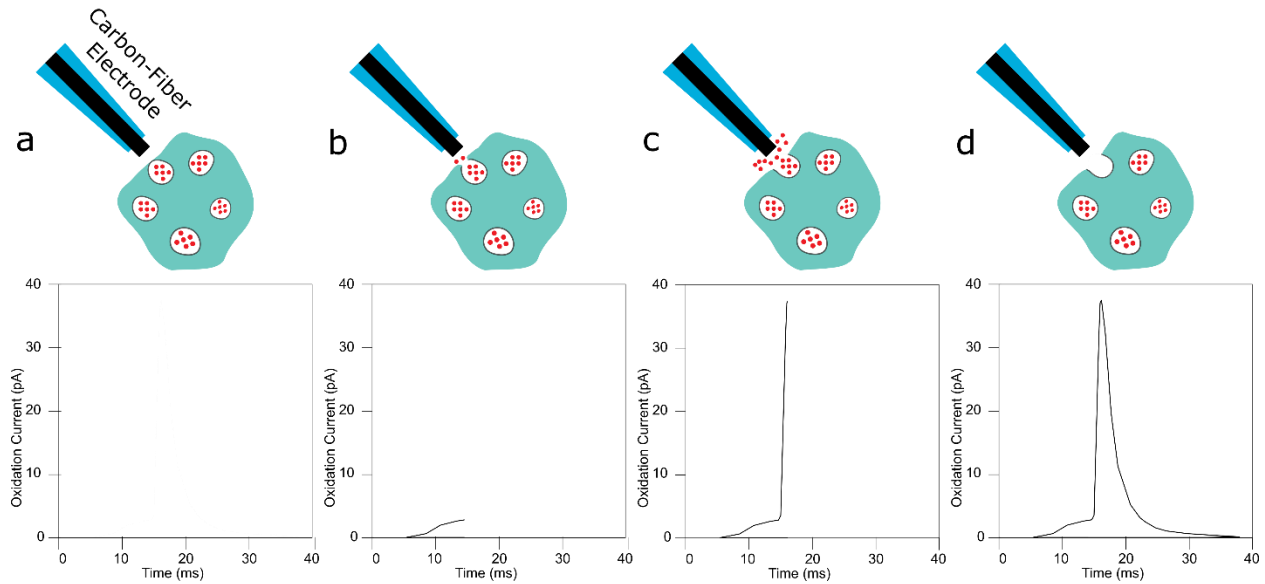
Figure 1.3: Illustration of an amperometric recording of a single secretion event using a CFE. (a) No signal is recorded before the quantal content of the vesicle is released. (b) A small foot signal is detected as a small concentration of quantal content is released through the small fusion pore. (c) The membrane fully expands and the signal intensity is directly related to the concentration of quantal content that is oxidized at the electrode. (d) Neurotransmitters diffuse out of the vesicle until the minimal signal is recorded as the quantal content is oxidized and depletes.

for neurological diseases, surface-modified electrodes are being developed to enable amperometry monitoring of biomolecules that are not inherently electroactive [23].

1.3   Transimpedance Amplification for Picoampere Level Oxidation Currents

The current generated from the oxidized quantal content during exocytosis is on the scale of picoamps. In order to convert this significantly small current into a readable voltage, transimpedance amplification is necessary. A basic transimpedance amplifier consists of an operational amplifier with a feedback resistor as shown in Fig. 1.4a. The current that is generated by the oxidized molecules at the electrode flows through the feedback resistor, thus resulting in an output voltage expressed as:

$$V_{out} = I_{oxidation}R \tag{1.1}$$

5

As seen in Eq. 1.1, the output voltage is directly related to the oxidation current (Fig. 1.4b-c) flowing through the amplifier and is scaled by the value of the resistor used. For example, using a GΩ resistor the transimpedance amplifier can convert picoamp levels of current (10^{-12}) to millivolts (10^{-3}).
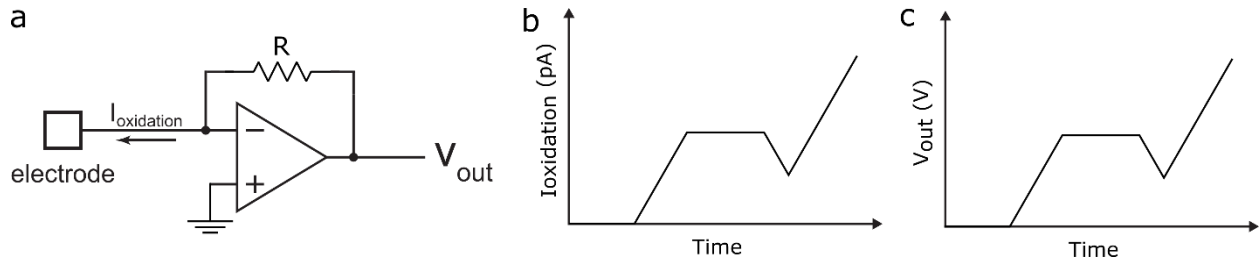
Figure 1.4: Transimpedance amplifier. (a) This transimpedance amplifier topology consists of an operational amplifier with a feedback resistor. (b) An example input current signal. (c) The output voltage of this transimpedance amplifier converts the pA level current input into a V level output.

Another topology for transimpedance amplification is a capacitor-based amplifier as shown in Fig. 1.5a. This amplifier specifically integrates the electrons released from the electroactive molecules onto the capacitor node labeled V_{out}. This results in a change in the voltage from the initial state of V_{DD} at the V_{out} node as the electrons accumulate (Fig. 1.5b), thus reducing the potential of the output voltage as more electrons are integrated onto the capacitor. At a periodic interval (T), the total voltage drop is readout from the amplifier and C_{int} is reset during readout by closing the switch SW (Fig. 1.5a) to begin the next integration cycle (Fig. 1.5b). The output voltage of this transimpedance amplifier is expressed as:

$$V_{out} = V_{DD} - \frac{1}{C_{int}} \int_0^T I_{oxidation} dt \qquad (1.2)$$
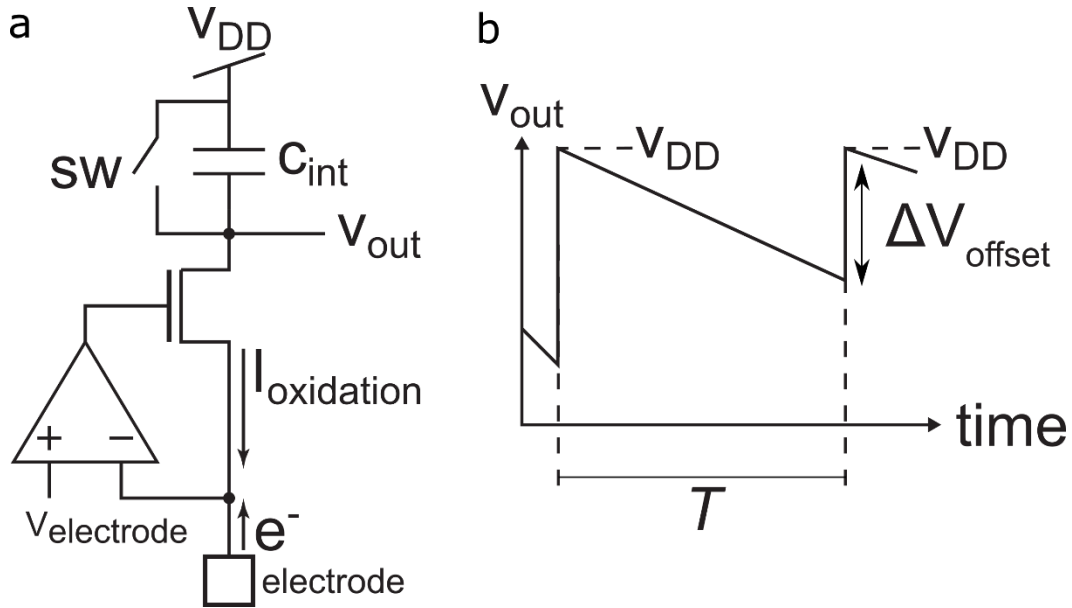
Figure 1.5: Capacitive Transimpedance Amplifier (a) The electrons from the oxidation reactions at the electrode are integrated onto Cint. (b) As the electrons accumulate at the Vout node, the output voltage decreases from the initial VDD potential. The change in voltage is periodically readout and the integration capacitor is reset to begin the next integration cycle.

As an example of this topology's output, if there is a constant 1 picoamp current that is integrated over 100 μs (10 kHz sampling rate) onto an integration capacitor of 116 fF [24], the resulting change in output voltage is ~0.86 mV.

A 116 fF capacitance is integrated into each amplifier of the neurochemical array [24] presented in this dissertation and occupies a small ~10μm × 10μm. Based on Eq 1.2, we can see that the amplification of the oxidation current can increase by either increasing the integration period or reducing the integration capacitor. However, by increasing the integration period the sampling rate is reduced, which is undesirable in capturing the fast exocytotic events. Therefore, reduction of the integration capacitor, which also reduces the space required for each amplifier, is the favorable technique to increase the transimpedance gain.

Either the resistor- or capacitor-based TIA topologies are acceptable for traditional single-cell amperometry as the space required to operate a few of these amplifiers does not present a significant constraint. However, research is moving towards high-throughput techniques to enable accelerated single-cell studies, such as neurodegenerative disorders and new emerging pharmacological treatments, as discussed in the next section. As the number of amplifiers increases from 10s, to 100s, and then 1000s, the area required for the amplifiers becomes prohibitive. A single GΩ resistor can occupy considerable space in the layout of a CMOS design, and thus the resistor-based transimpedance amplifier shown inf Fig. 1.4 becomes impractical when making amplifier arrays with 100s or 1000s of amplifiers. Alternatively, the small capacitive TIA shown in Fig. 1.5 can be used to enable large-scale transimpedance amplification arrays for neurochemical monitoring of fast exocytosis events from neurons.

1.4 Limitation of CFE-based Single-cell Amperometry

Despite the significance of the studies conducted and the discoveries made using amperometry, traditional amperometric measurements conducted at the single-cell level are traditionally a low-throughput method where each cell is measured individually with a microelectrode under microscopic observation. This makes the technology time-consuming to acquire sufficient data to derive statistically significant conclusions. Additionally, it is important that amperometry is performed at the single-cell level to account for heterogeneity in the characteristics of quantal release among the cell population [10], [25]. Therefore, to compare the kinetics of quantal release and the size of vesicle secretion with statistical significance, typically more than 30 independent cell measurements are collected for both the experimental and control

groups to develop meaningful conclusions. These low-throughput studies and can take from weeks to several months [26] to research the effects of neurological diseases or pharmacological treatments on exocytosis dynamics. Thusly, the prohibitive features of single-cell amperometry have limited the wide application of this technology to survey (or screen) the molecular effects of pharmacological modulations and neurodegenerative pathologies associated with the synaptic neurotransmitter secretion process.

To overcome the low-throughput nature of traditional single-cell techniques, large-scale MEAs offer high-throughput capability for single-cell studies. MEAs have been previously used for single-cell detection of quantal exocytosis from chromaffin cells [27], capturing the single-cell level exocytosis heterogeneity of PC-12 cells [28], real-time monitoring of the quantal release of dopamine from PC-12 cells during the culture or propagation process [29], and capturing the reuptake inhibition effects of nomifensine on PC-12 cells [30]. Additionally, MEAs have been useful in enhancing the spatial resolution of electrochemical recordings. Such as mapping the level of H_2O_2 in relation to neurological diseases in a brain slice [31], electrochemical imaging of redox molecules diffusing across an MEA [32], and imaging of metabolites in biofilms [33]. The high-throughput simultaneous measurements from a large number of cells enabled by MEAs results in a tremendous benefit in enabling rapid studies of neurodegenerative disorders and the effects of therapies as well as new drug discoveries that target the modulation of neurotransmitters.

However, the electrodes throughout an MEA must be connected to external amplifiers for signal amplification and processing. The use of external amplifiers becomes prohibitively expensive as the number of simultaneous recordings grows (for single-cell electrophysiology

~$15,000 per amplifier), but more importantly, it sets a limit on the total number of electrodes in an array because the external wiring becomes impractical.

1.5   CMOS-based Microelectrode Array

To resolve the challenges with increasing the density of parallel recordings using an MEA, we can integrate an array of amplifiers and on-chip electrodes in a CMOS chip. This method drastically lowers the cost per amplifier and removes the need for external wiring because the on-chip electrode and on-chip amplifier establish a connection within the chip. Therefore, the CMOS-based MEA opens the opportunity to increase the electrode count of an MEA to above 1000s.

Several CMOS-based biosensors have been proposed using this concept of MEA integration [34]–[39] to perform various types of electrophysiology. Developed CMOS-based biosensors have demonstrated their parallel recording capabilities through the mapping of the concentration of ferricyanide across a 16×16 electrode array [40], the diffusion of H_2O_2 in a 32×32 electrode array [32], and the flow injection of several analytes across a 128×128 electrode array [41]. For the purpose of measuring action potentials from a neuron with a high spatiotemporal resolution, a multifunctional CMOS chip with an array of 59,760 on-chip electrodes can provide a high channel count of up to 2048 electrodes for simultaneous recording [36], [42]. This multifunctional CMOS chip featured 28 amplifiers for neurotransmitter detection using cyclic voltammetry with a noise level of 100s of pA_{RMS}. Using an array of 11,011 electrodes, action potentials from axons in a neuronal network were measured with high spatiotemporal resolution [37], [43]. Impedance spectroscopy with a high spatial resolution and low-noise was performed with an array of 59,760 electrodes integrated onto a multifunctional CMOS chip [44]. To study

bursting events from neurons in a neuronal network, a device providing high spatial resolution with an array of 4096 electrodes was proposed [45]. Another proposed system contains 1024 pixels to provide a low-noise multifunctional CMOS device with enhanced spatiotemporal resolution for extracellular potential measurement, optical cell detection, current stimulation, and cellular impedance measuring [39]. Furthermore, these CMOS-based bioelectronic systems have been developed and used for high-throughput recordings of neurotransmitter secretion from bovine chromaffin cells with a 10×10 electrode array [26], [34].

1.6   Outline of Dissertation Organization and Contents

This dissertation outlines the development of a CMOS-based neurochemical MEA for high-throughput monitoring of neurotransmitter secretion at the single-cell level. The methodology supporting the development of this novel technology and the studies performed using this new instrumentation are summarized in the following chapters. A small 30 μm × 30 μm transimpedance amplifier, which is based on current integration onto a capacitor, was developed to detect the small pA currents from neurotransmitter secretion. Additionally, high-density integration of this small 30 μm × 30 μm amplifier is achieved by a half-shared amplifier design, wherein the half-shared structure improves the scalability of the amplifiers by sharing the non-inverting side of the operational amplifier with many inverting halves. The design and performance of this transimpedance amplifier array, enabling high-density neurochemical recordings, are discussed in chapter 2. In chapter 3, parallel 1024 cyclic voltammetry is performed using the integrated neurochemical electrode array. These cyclic voltammetry recordings are used to examine the quality of electrochemical electrodes by measuring the double-layer capacitance that

forms at the electrode-electrolyte interface as this capacitance is directly related to the effective area of the electrodes. This measured capacitance reveals the contamination on the electrodes and determines how much plasma treatment is needed to descum the surface of the electrode. Fast electrochemical imaging of the diffusion of dopamine and hydrogen peroxide is recorded at 40,000 frames per second across the developed neurochemical detector array. To support the high level of data generated by the neurochemical detection array for this electrochemical imaging, a custom FPGA-based data acquisition system is designed to interface with the high-density neurochemical detection array and is discussed in chapter 4. In chapter 5, the secretion of neurotransmitters from human neuroblastoma cells (SH-SY5Y) are recorded and characterized with single-cell resolution. Secretions from 76 cells are simultaneously recorded by loading the developed device with SH-SY5Y cells. The data presented in chapter 5 shows the device's capability of recording vesicle secretion at a single-cell level, with 1024 parallel channels, to provide high-throughput detailed information on the dynamics of dopamine release at a single-vesicle resolution. In chapter 6, the developed 1024 neurochemical microelectrode array is applied to study the modulation of neurotransmitter secretion after treating cells with drugs used for treating Parkinson's disease and depression. The modulation of neurotransmitter secretion dynamics due to L-Dopa (Parkinson's disease treatment), selegiline (Parkinson's disease treatment), or desvenlafaxine (depression treatment) are investigated and presented in this dissertation. In chapter 7, a novel biohybrid synapse that produces quantal neurotransmitter secretion to relay information to an artificial postsynaptic receptor is developed. This neurochemical biohybrid synapse paves the way for a new generation of brain-inspired computing by enabling single biological cell to single artificial neuron connectivity.

The presented novel CMOS-based neurotransmitter detection system can capture a large pool of quantal events in the span of minutes, providing rapid results compared to the conventional amperometry technique that can take from weeks to months to amass a comparable dataset [26]. Using this novel technology, we can significantly accelerate the study of neurodegenerative disorders, such as Parkinson's disease and Alzheimer's disease, as well as new pharmacological treatments that affect neurotransmitters in the brain at the single-cell level, such as drugs for depression or Parkinson's disease.

CHAPTER 2: HALF-SHARED TRANSIMPEDANCE AMPLIFIER FOR PICOAMPERE BIOSENSOR MEASUREMENTS

2.1   Chapter Notes

In this chapter, the design of a small 30 μm × 30 μm transimpedance amplifier, which is based on current integration onto a capacitor, is developed to detect the small pA currents from neurotransmitter secretion. High-density integration of this amplifier is achieved by a half-shared amplifier design. The half-shared amplifier improves the scalability of the amplifiers by sharing the non-inverting side of the operational amplifier with many inverting halves. The performance of the transimpedance amplifiers using the half-shared amplifier structure is characterized to demonstrate the isolation between the amplifiers in the shared structure, enabling high-density integration of amplifiers with independent neurotransmitter detection capability. The amplifier array discussed in this chapter is the basis for the single-cell neurochemical sensing device presented in this dissertation. The work described in this chapter was completed with Geoffrey Mulberry and Brian N. Kim [*].

2.2   Introduction

A transimpedance amplifier (TIA) is used in bioelectronic systems to measure currents in biological applications, including *in vivo* and *ex vivo* dopamine measurements [46]–[48], single-cell amperometry [24], [42], [49]–[51], photoplethysmography (PPG) [52]–[54], pulse oximetry [55], and nanopore recordings [35], [56]. They traditionally consist of a circuit to transform the current into the electrode into a voltage measurement. To implement a TIA, most low-noise

---

[*] In this chapter, we use material published in IEEE Transactions on Biomedical Circuits and Systems, 2019 [61].

measurements use an operational amplifier (OPA) to hold an electrode or a photodiode at a reference voltage while converting the current at the electrode or photodiode into voltage, thus forming a transimpedance amplifier. As such, TIAs on integrated CMOS devices usually contain OPAs within them. For high-throughput (large-scale) measurements from an array of detectors, a larger number of amplifiers is required. Thus, it is crucial to minimize the size requirements of each TIA if a larger scale recording is desired. One approach for minimization of TIAs is the half-shared structure of the OPA, which is explored and analyzed in this chapter. The approach is powerful, as it enables the doubling of amplifiers on a single chip, increasing throughput for demanding applications. However, few in the field have been using the technique for their designs, possibly due to a lack of awareness and analysis of the concept which will be addressed by this chapter.

The half-shared design has been successfully adapted in previous studies to yield large-scale recordings, ranging from tens to thousands of amplifiers [24], [34], [49], [51], [57], [58]. The design principle of a half-shared OPA is to allow for the non-inverting half to be shared between multiple OPAs, reducing the required die area for multiple OPAs by nearly a factor of two. In an effort to have high bandwidth and a wide dynamic range, a folded-cascode architecture was used for the early half-shared amplifiers [49]. This folded-cascode architecture achieves a wide dynamic range and bandwidth at the cost of high power (nearly double) and area consumption. However, if used for most electrophysiology or photodiode applications, the required bandwidth is small (< 20 kHz). Additionally, many CMOS detector arrays for biomedical applications operate below 20 kHz, usually in the 10 kHz region [57], [59]. This low bandwidth can be easily obtained with a traditional five transistor (5T) OPA, further eliminating significant benefits to the folded-cascode

architecture. Thus, the 5T OPA design is adapted in this work to minimize the power and area consumption.

The half-shared structure has been analyzed in the past for a limited amount of scalability, usually, two OPAs sharing one non-inverting half [49], [60]. In this chapter, we will expand the analysis for an unspecified number of sharing branches to evaluate the effect and implications for larger-scale recordings (Section 2.3). Using the half-shared design, an integration-based TIA is designed and tested. The noise analysis of non-stationary circuits, such as an integration amplifier, is a challenging task. This is because most noise simulations assume a steady-state in the time-domain for the frequency-domain analysis. In order to evaluate the noise characteristics of non-stationary TIAs, we produced a simple approach to convert the integration amplifier to a stationary circuit for the noise analysis and applied post-signal-processing to simulate the non-stationary effect (Section 2.4). To study the 5T half-shared OPA structure, a CMOS chip [51] was designed and fabricated using a 0.35 μm 4M2P process. Since the techniques described in this chapter are valid for all process nodes, a 0.35 μm process was chosen as a cost-effective means to fabricate this proof-of-concept work. These techniques can be implemented on any modern analog CMOS process to further reduce die area required for large arrays. In biological applications, the voltage required to monitor or stimulate the electrophysiological processes is often larger than few volts and the larger dynamic range of large process nodes, such as 0.18 and 0.35 μm, is useful. Section 2.3 discusses the design of the TIAs, OPAs, and array in detail. In short, the CMOS chip consists of a total of 1024 array elements arranged into a 32×32 grid. The TIAs within each array element are based on OPAs utilizing the half-shared design and have additional circuitry allowing for reconfiguration for testing and different modes of operation. Although each TIA relies on the half-

shared OPA architecture, they are effectively independent from the others, allowing 1024 parallel measurements. The fabricated circuit is used to characterize the performance of the half-shared design, including gain, linearity, noise, mismatch, bandwidth, and crosstalk (Section 2.5).

2.3   Transimpedance Amplifier Array Design

The half-shared OPA design is described within this section along with how they are used within the TIAs and array elements and the overall structure of the array. The TIAs used rely on a rather simple design of OPA. Although rudimentary, the 5T OPA's lend themselves well to half-sharing, use low power, require little die area, and their performance within the presented TIA design is sufficient as will be demonstrated in sections 2.4 and 2.5.

2.3.1   Half-shared Amplifier Design

The enabling feature of this array's high density is the half-shared architecture used for the OPAs within the TIAs. The basis of the half-shared design exploits redundancies that occur when traditional 5T OPAs in the negative feedback configuration are used in parallel, and their non-inverting inputs share the same voltage. A half-shared OPA schematic is presented in Fig. 2.1. Here, M_0 and M_1 form a differential pair, where M_{bias} provides a bias current, and M_{L0} and M_{L1} form a current mirror load for the differential pair. The non-inverting and inverting inputs are the gates of M_0 and M_1, respectively. The output is taken at the drains of M_{L1} and M_1.

Usually, if a second 5T OPA is added, five additional transistors would be required. However, if the bias current and the non-inverting input voltage are the same for the two OPAs, only two additional transistors are required. This is due to the redundancy within the non-inverting half. Thus M_{L0} and M_0 can be shared between the two OPAs. In this example, M_{L2} and M_2 are all

that is required to add a second OPA. For the second OPA, M_2 and M_0 form the differential pair where M_2's gate is the second inverting input. Conceptually, this method can be extended to any amount of additional OPAs.

2.3.2 Analysis of Half-shared Structure

The circuit in Fig. 2.2 shows multiple inverting half amplifiers sharing a single non-inverting half. To examine the tradeoff of multiple inverting halves sharing a single non-inverting
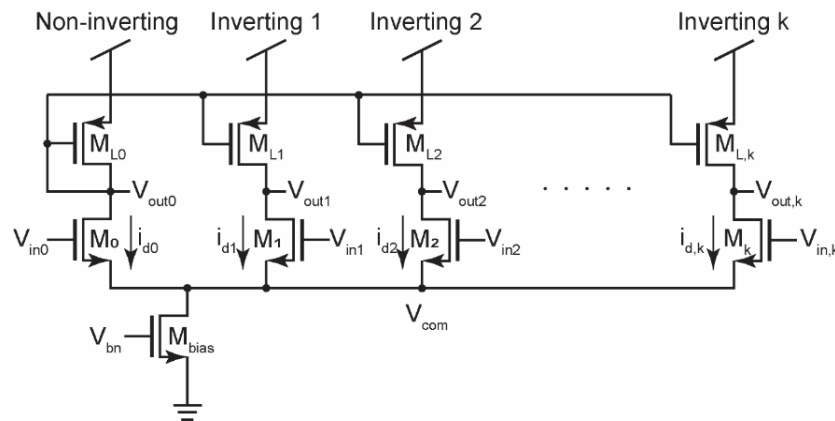
Figure 2.1: A half-shared design with k-counts of inverting amplifier shared a single non-inverting half. Transistors M0 and ML0 form the non-inverting half and M1-Mk, ML1-ML,k form inverting halves of additional OPAs. All NMOS and PMOS bulk connections are to ground and VDD respectively. 2019 © IEEE

half, the small-signal gain of each branch is analyzed. The purpose of this analysis is to evaluate the performance of the half-shared structures before it is placed and used as a part of our TIA. The current in the non-inverting half can be expressed:

$$i_{d0} = g_{m0}(v_{in0} - v_{com}) \tag{2.1}$$

where g_{m0} is the transconductance of M_0.

Assuming the transconductances of M_0, M_1, M_2, and M_k are equal, currents in inverting halves can be generally expressed:

$$i_{d,k} = g_m(v_{in,k} - v_{com}) \tag{2.2}$$

where k is the kth inverting half amplifier sharing the common non-inverting half. Because M_{bias} supplies constant current for biasing, it is removed from the small-signal circuit, thus

$$i_{d0} + i_{d1} + i_{d2} + \cdots + i_{d,k} = \sum_{n=0}^{k} i_{d,n} = 0. \tag{2.3}$$

From Eqs. (2.1), (2.2), and (2.3), we can establish V_{com}:

$$V_{com} = \frac{\sum_{n=0}^{k} v_{in,n}}{k+1}. \tag{2.4}$$

Load transistors, M_{L0}, M_{L1}, M_{L2}, and $M_{L,k}$, form a current mirror and thus currents through these transistors are equal.
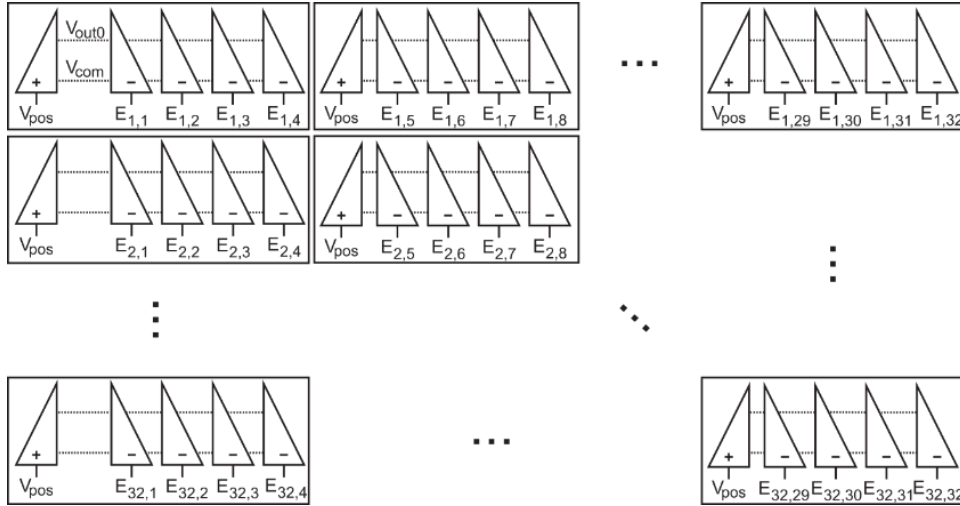
Figure 2.2: Block diagram of the CMOS design containing 1024 half-shared amplifier array elements. Each block consists of a group of four amplifiers using the half-shared architecture to save silicon area while increasing the number of on-chip amplifiers. Each OPA is represented as cut in half, with the right half being the inverting side located within a corresponding TIA, and the left half being the non-inverting half common to each block of four amplifiers. The array is eight groups of four amplifiers wide and 32 rows tall to create a total of 1024 amplifiers. Each inverting inputs are labeled with its row- and column- coordinate position as their indices. 2019 © IEEE

$$i_{L0} = i_{L1} = i_{L2} = i_{L,k} = i_{d0}. \tag{2.5}$$

The current entering the node V_{out1} is

$$i_{out,1} = i_{L0} - i_{d1} = i_{d0} - i_{d1}, \tag{2.6}$$

and this current used to generalize other halves' output current,

$$i_{out,k} = i_{d0} - i_{d,k}. \tag{2.7}$$

Because $v_{out,k}$ is loaded by the output resistance of $M_{L,k}$ and M_k, $r_{L,k}$ and r_k, $v_{out,k}$ can be expressed as:

$$v_{out,k} = (r_{L,k}//r_k) \cdot i_{out,k}. \tag{2.8}$$

Using Eqs. (2.2), (2.3), (2.4), and (2.7),

$$\begin{aligned}
v_{out,k} &= -(r_{L,k}//r_k) \cdot (\textstyle\sum_{n=1}^{k} i_{d,n} + i_{d,k}), \\
&= -g_m \cdot (r_{L,k}//r_k) \cdot [(\textstyle\sum_{n=1}^{k} v_{in,n}) + v_{in,k} - (k+1) \cdot v_{com}] \\
&= -g_m \cdot (r_{L,k}//r_k) \cdot [(\textstyle\sum_{n=1}^{k} v_{in,n}) + v_{in,k} - (\textstyle\sum_{n=0}^{k} v_{in,n})] \\
&= -g_m \cdot (r_{L,k}//r_k) \cdot (v_{in,k} - v_{in0}).
\end{aligned} \tag{2.9}$$

In Eq. 2.9, we can see that the output ($v_{out,k}$) of a particular inverting half is only dependent on $v_{in,k}$ and v_{in0}, not related to other inverting halves' inputs. Thus, multiple inverting halves can operate independently without suffering crosstalk. This analysis also reveals that there is no obvious limit on how many inverting halves can be attached to share a single non-inverting half.

In the half-shared design, the bias current of each amplifier is provided from M_{bias}. Therefore, if the number of inverting half amplifiers increases to share the single non-inverting half, the current level through M_{bias} should linearly increase to supply consistent levels of bias to individual amplifiers. This requires V_{bn} to be elevated. To operate M_{bias} in saturation, V_{com} needs to be increased with V_{bn}, which will limit $V_{bn} - V_{com}$ to be less than the threshold voltage. Thus, one apparent tradeoff of increasing the number of sharing amplifiers is the reduced dynamic range of $V_{in,k}$ and $V_{out,k}$. This effect could be reduced by increasing the width of M_{bias}, however, since

the objective of half-sharing is to reduce die area, M_{bias} must be sized as a compromise between size and number of shared branches.

2.3.3 Large Array Design using Half-shared Structure

The large array of densely packed TIAs consisting of 1024 amplifiers on a single CMOS chip uses the half-shared structure to its advantage. In this case, we chose to have four inverting amplifiers to share one non-inverting half considering the required dynamic range for biomedical applications. For the large array, an important design requirement is that, for this architecture to work properly, transistors M_0, M_1, M_2, M_3, and M_4 must all be matched sizes, as well as load transistors M_{L0}, M_{L1}, M_{L2}, M_{L3}, and M_{L4}. If the sizes are not matched, then the individual half currents will be unequal and Eqs. (2.5), (2.6), (2.7), and ultimately (2.9) will be invalid. The consequence of poor matching is that the inverting halves will no longer be independent. The arrangement of the TIAs for the large array is shown in Fig. 2.2. A 32×32 grid is used to arrange the 1024 amplifiers as densely as possible. Along any given row, eight half-shared blocks are used where every group of four amplifiers along the row are part of a half-shared block. Using this arrangement of eight half-shared blocks allows 32 TIAs to fit in the same die area that could fit only 17 TIAs using traditional 5T OPAs. This increase in packing density provides an effective method for increasing the throughput of parallel measurements. The V_{pos} terminals of the eight half-shared blocks in each row are connected together and are additionally connected to all 32 rows. This enables a global V_{pos} for setting all 1024 electrode potentials when performing current measurements in electrolytic solutions. Such measurements are the basis for single-cell electrophysiology and amperometry experiments. Each column has its own analog output enabling

21

entire rows of 32 TIAs to be read out simultaneously row after row. While one row is being read

out, the other 31 in the same column are performing integration of their electrode currents, enabling
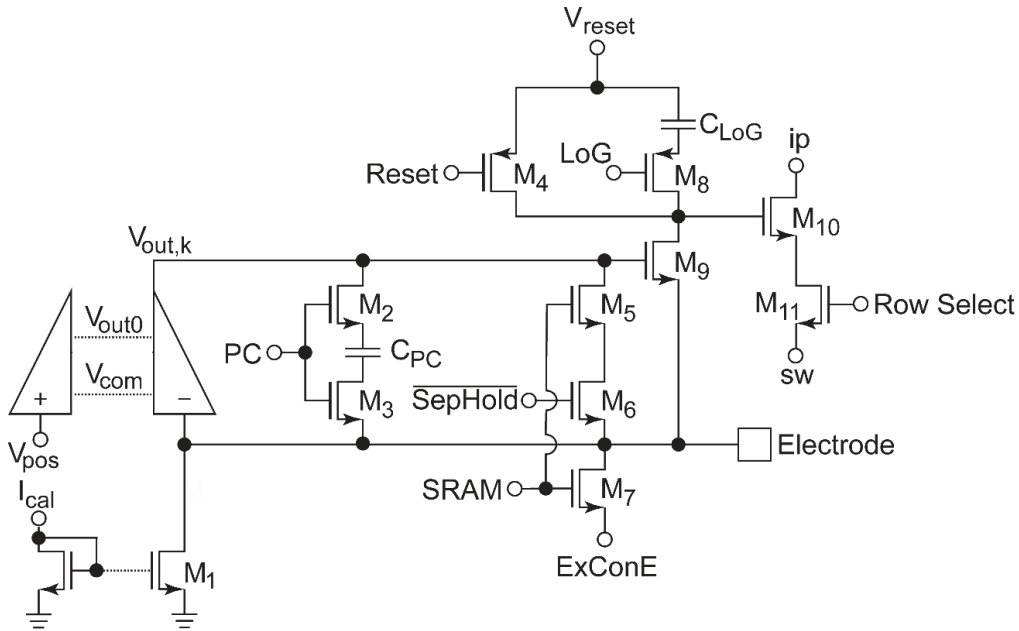
Figure 2.3: Schematic of an individual transimpedance amplifier element. The circuit is a reconfigurable and programmable using the embedded SRAM. The design includes the inverting half of an OPA and shares the non-inverting half which is separated so it can be shared with three other amplifiers. Similar to Fig. 2.1 and Fig. 2.2, the shared nodes V_{out0} and V_{com} are represented as dashed lines, showing the connections of the half-shared OPA blocks. $V_{out,k}$ is the output of the non-inverting OPA half for this TIA element. 2019 © IEEE

a true 1024 simultaneous measurements without deadtime. The detail of the staggered time-

division multiplexing is previously described by the authors [24], [34].

2.3.4   Programmable TIA

Fig. 2.3 shows the schematic for one of the 1024 TIAs using the half-shared amplifier.

Each TIA contains 11 MOSFETs, a half-shared OPA, an SRAM, and two capacitors. The TIA

design is based on a regulated cascode amplifier (RCA). The current at the electrode is integrated

at the drain node of M_9 which is then measured as a voltage by M_{10} and M_{11}, periodically (t_{int}).

Normally, an integrating capacitor (C_{int}) should be placed at the drain node of M_9 which sets the

transimpedance gain (G_Z) of the RCA. The gain can be expressed:

$$G_Z = \frac{t_{int}}{C_{int}} \ (V/I).$$

(2.10)

To maximize the transimpedance gain, the parasitic capacitance (<10 fF) which exists at

the drain node of M_9 is used. The integrating TIA design achieves similar or better noise

performance compared to a resistive TIA, but with a high area efficiency due to the lack of the

resistor. M_1 forms half of a current mirror used to set a calibration current through the TIA via I_{cal},

mainly for testing the transimpedance gain but also to allow the measurement of negative currents.

Because we intended to operate the OPA with extremely low power, the phase margin of the RCA

can be low with poles from the OPA and M_9 source, closely overlapping. Optional phase

compensation can be enabled when PC (phase compensation switch enable) is high by turning on

switches, M_2 and M_3, and inserting C_{PC} into the feedback loop, thus increasing the phase margin.

The integration capacitance is reset by switch M_4 every integration period (t_{int}). The TIA has two

programmable gain settings enabled by C_{LoG}. C_{LoG} can be added to the parasitic integration

capacitance by turning on switch M_8 to decrease the gain in low-gain mode by setting LoG low.

Thus, in the low-gain mode, the integration capacitance is a summation of C_{LoG} and the parasitic

capacitance. The TIA can be connected to an external electrode pad, ExConE, by turning on switch

M_7 when the SRAM is set high. An additional function of the SRAM is to use the OPA to be in

the unity-gain mode when $\overline{SepHold}$ and the SRAM are both high. When both M_5 and M_6 are on,

the inverting input of the OPA and the output are shorted, enabling unity-gain. Every TIA has a

dedicated SRAM within the 900 μm^2 for the fully-addressable programmable array. Switch M_{11}

allows for connection to the column's output buffer, where M_{10} is one of the output buffer transistors when Row Select is high. The minimum dimension is used for all switch transistors. For best matching characteristics, analog transistors M_9 and M_{10} are square.

For this array design, each array element is set to be 30 μm $\times$ 30 μm. This is to integrate the entire 1024 amplifier array in less than a 1-mm^2 area. Transistors for the OPAs, M_{bias}, M_k, and $M_{L,k}$, are sized at 10 μm $\times$ 10 μm to minimize mismatch. Without the half-shared architecture, the gates of the transistors alone for a single OPA require 500 μm^2 or 55.8% of the 900 μm^2 available for each array element. This would leave insufficient area for the remaining circuitry shown in Fig. 2.3. However, with the half-shared structure, only 2 OPA transistors must fit into each array element, requiring 200 μm^2 or 22.2% of the array element area, allowing for the addition of the extra circuitry.

2.4 Noise Analysis of Non-stationary Circuit

The integration TIA has an integrating node where voltage can swing up to 2 volts within the integration period, which then resets after each integration cycle. Thus, this circuit is non-stationary in the time-domain and the simulation in the frequency domain is difficult to implement. Thus, in this section, we are exploring a conversion method to estimate the noise performance for a non-stationary circuit using a typical simulation tool.

2.4.1 Non-stationary Circuit

The integrating circuit is only functional if the integration capacitor is periodically reset. Without the periodical reset, the charge in the integration node discharges completely which disables the TIA. Thus, the circuit in Fig. 2.3 cannot be used for a typical AC/noise analysis. This

non-stationary circuit can be converted to a stationary circuit by replacing the integration capacitor

with a resistor. The value of the resistor should be:

$$R = G_Z = \frac{t_{int}}{C_{int}} \; (V/I)$$

(2.11)

where the resistance is identical to the transimpedance gain set by the integration period

and integration capacitance. The resistor-based circuit is then used for the noise analysis with the

noise model provided by the semiconductor manufacturer. The noise measured at the integration

node consists of various noise sources from the OPA, cascode transistor (M_9), and the resistor.

This analysis does offer some insight into the characteristics of the TIA's noise but fails to capture

the effect of the current integration. The current integration for the set duration in a time domain

creates a convolution of a rectangular pulse (Fig. 2.4a).

$$i_{TIA}(t) = i_{int}(t) * rect(t)$$

(2.12)

where the *rect(t)* is the rectangular function (1 for arguments within a window of period

t_{int}, and 0 for all arguments outside of the window) and i_{int} is the current measured at the integration

node. This expression can be transformed to the following equation:

$$I_{TIA}(f) = I_{int}(f)Y(f)$$

(2.13)

where Y(f) is the Fourier transform of the rectangular function. The unitary Fourier

transform of *rect(t)* is

$$Y(f) = \int_{-\infty}^{\infty} rect(t) \cdot e^{-i2\pi ft} dt \;.$$

(2.14)

Thus, the frequency response can be expressed as a *sinc()* function.

$$Y(f) = \frac{\sin(f \cdot \pi \cdot t_{int})}{f \cdot \pi \cdot t_{int}} = sinc(f \cdot \pi \cdot t_{int}).$$

(2.15)
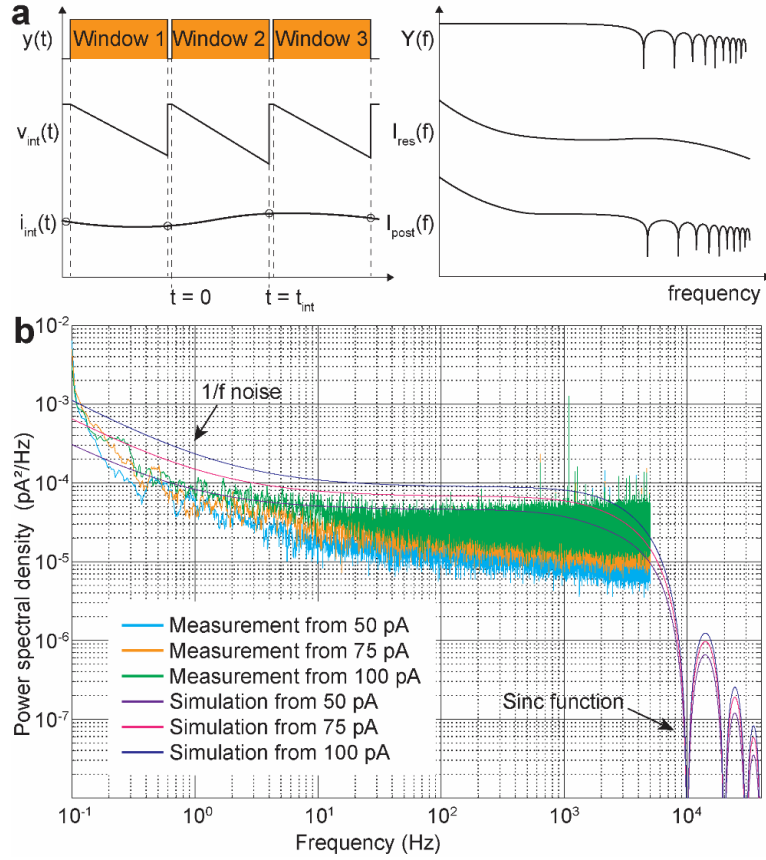
Figure 2.4: Characterization of noise using simulation and chip measurement. (a) The current integration creates windows for each integration period and reports the current level at the end of each integration cycle. The window in time-domain generates a sinc() function in the frequency domain which can be used to estimate the noise performance in the non-stationary circuit. (b) Noise analysis from the simulation is compared with the chip measurements for various input current levels, 50 pA, 75 pA, and 100pA. 2019 © IEEE

The multiplier, $\pi \cdot t_{int}$, is to adjust the *sinc()* filter for the specific rectangular function which has the t_{int} window. Any input passing $Y(f)$ with $1/t_{int}$ interval frequencies should have zero output. To generate the equivalent noise analysis from the stationary circuit to the non-stationary circuit, a post-signal-processing can be applied by multiplying the noise measurement from the simulation with Eq. 2.15.

$$I_{post}(f) = I_{res}(f)Y(f). \tag{2.16}$$

Therefore, $I_{post}(f)$ closely estimates $I_{TIA}(f)$ in Eq. 2.13. One difference is the thermal noise added by the resistor in the simulation. This effect can be extracted from Eq. 2.16 if relevant. Since the gain we are simulating is 7.00 mV/pA, the resistor we use is 7 GΩ. The thermal noise of the 7 GΩ resistor is only ~2×10^{-6} pA^2/Hz and is significantly smaller than the typical noise in the TIA, so we have ignored it in the analysis.

The simulated noise is shown in Fig. 2.4b with the measured noise from the CMOS chip at various input current levels, 50pA, 75pA, and 100 pA. All noise measurements show 1/f noise at low frequencies. At high frequency, the effect of post-signal-processing of adding *sinc( )* response is observed as expected. For all three input current levels, the noise levels between the measurement and the simulation are within a factor of 5, which reveals the discrepancy of the noise characteristic in deep weak inversion. The input current below nano-ampere is considered deep weak inversion and the noise model provided by the manufacturer are generally optimized for strong inversion transistors. Therefore, for any amplifiers operating with pico-ampere current levels, the noise characteristic can be better evaluated by measurements, rather than modeling and simulation. Nonetheless, the simulation method presented here does provide a viable method to estimate the noise level and the frequency characteristics within a factor of 5 before the CMOS fabrication.

2.5   Characterization and Measurement

To demonstrate the effectiveness of the half-shared architecture, the fabricated CMOS array was used for several experiments using the test setup shown in Fig. 2.5. This section contains

measurements of a representative column's output, transimpedance linearity, amplifier mismatch of the 1024 TIAs, and frequency response.

2.5.1 Transimpedance Measurement

The half-shared TIA's transimpedance conversion performance is studied by first configuring the amplifiers to low gain mode, applying a known DC I_{cal} input (from 0 to 1000 pA), and measuring the output waveforms. The array is equipped with multiplexers as previously described in [34], [51] to reduce the number of outputs. 32 TIAs in a column share a 32-to-1 time-division multiplexer. The waveforms resulting from this multiplexed transimpedance
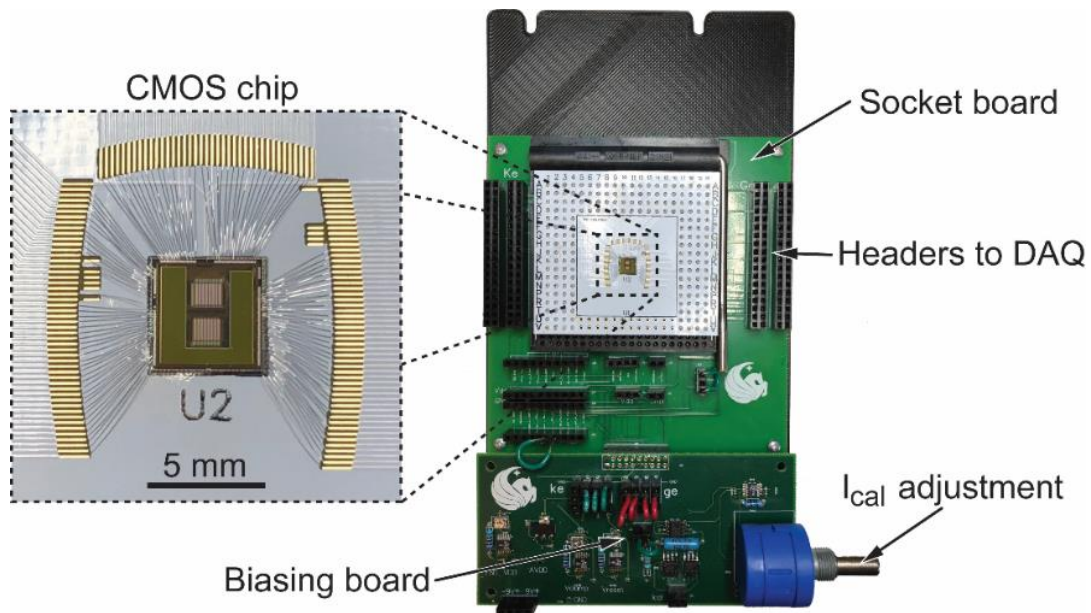
Figure 2.5: Overview of the measurement system. The CMOS chip is bonded to a PCB which is inserted into a socket on the socket board. The socket board allows for connections to the National Instruments DAQ unit and to the biasing board. The biasing board converts battery or power supply voltage into V_{DD}, V_{reset}, V_{pos}, and I_{cal}. I_{cal} is easily adjustable via the 10-turn potentiometer. 2019 © IEEE

28

measurement are shown in Fig. 2.6. The separate traces represent the voltage output versus time of a single column's output at a specific I_{cal} level. The square shape of the pulses resulting from the correlated double sampling (CDS) output stage are clearly shown. CDS allows for the removal of the offset produced by V_{reset} by sampling at both the reset and output values and performing a subtraction. The left plot shows the output from a single column measurement (the pulses are the 32 TIAs in that column). The inset plot shows only four rows of the same output, which more clearly shows the linearity of the output voltages for the first four TIAs in the column. The different heights of the pulses indicates a difference in the gain of each of the amplifiers. The difference in gain between the amplifiers is likely caused by process variations such as the dimensions of the transistors, causing mismatch of the OPA inputs, and the dimensions of the integrating capacitors. Parasitic capacitance variation across the array could also affect the gain, so care must be taken in the layout to ensure that the array elements are identical. It is important to note, however, that these variations may vary between array elements but should be consistent within any given array element. As a result, the variations can be calibrated out by applying known signals via I_{cal} and recording the gain of each amplifier before taking measurements.

2.5.2 Transimpedance Gain Linearity

The TIA's linearity performance is evaluated by using the data from the transimpedance recording shown in Fig. 2.6 and creating the voltage versus current plot shown in Fig. 7a. The results from all 32 TIAs' outputs are used to create a least-squares linear fit of V_{out} against I_{cal}. Based on the fit, the transimpedance gain of the low-gain mode is 0.86 mV/pA. The resulting fit has an R^2 value of 0.999, indicating a high-quality linear performance of the TIAs. We have

performed the same measurement for the high-gain mode. The transimpedance gain of the high-gain mode is 7.00 mV/pA, and the R^2 value is 0.988. The relatively low coefficient of determination in the linear fitting for the high-gain mode is apparent in Fig. 2.7a which has a small curvature around 50 – 60 pA. This is likely due to the nature of parasitic capacitance which is mainly composed of junction and gate capacitors at the integration node. To study the linearity of the entire array, I_{cal} is also measured from all 1024 amplifiers at 700 pA and 200 pA and the gain of each amplifier is calculated. For this measurement, the gain is 0.862 mV/pA with a standard deviation of 0.034 mV/pA.
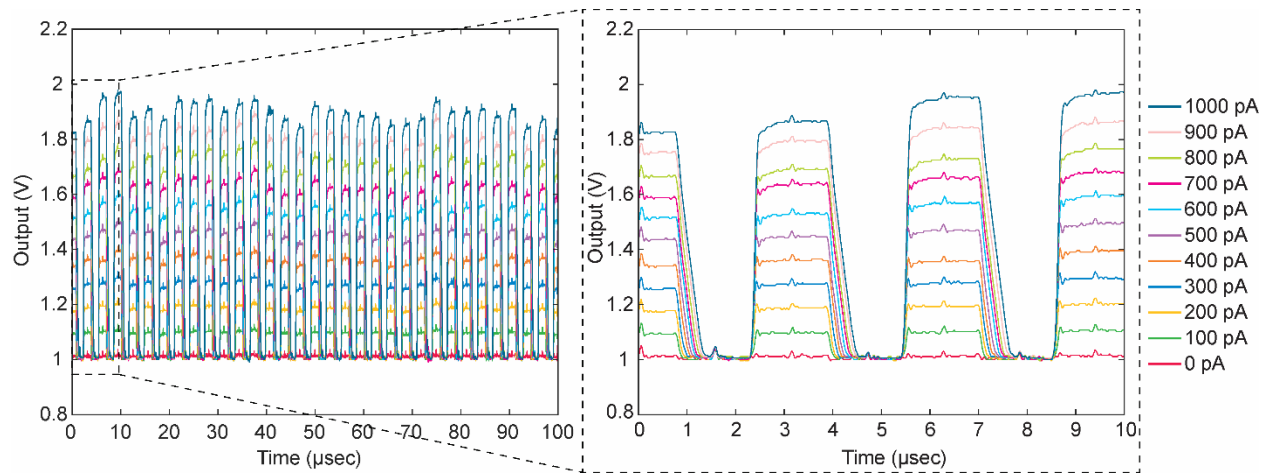
Figure 2.6: Chip's output waveforms show a multiplexed output of 32 TIAs for various input current levels into I_{cal} from 0 pA to 1000 pA. Each pulse represents the output of a single TIA. 2019 © IEEE

2.5.3 Mismatch

Small differences in transistors' sizes within the OPA can cause a voltage mismatch between the inverting and non-inverting inputs. The mismatch is due to the fabrication process variation. Depending on the application, the inverting inputs control the electrode voltage and the accuracy of this voltage can be important. Because the CMOS chip designed in this work features

30

1024 OPAs, the matching performance is worth evaluating. To test this, the array elements are

programmed to unity gain mode and individually connected to the external electrode so that a

simple mismatch measurement could be performed. As discussed in Section 2.3.4 and shown in

Fig. 2.3, unity gain mode connects the OPA's output directly to the inverting input. The non-

inverting input is held at V_{pos}, and the output voltage is measured at the ExConE. If the OPAs have

no mismatch, every OPA will produce exactly V_{pos} at its output.
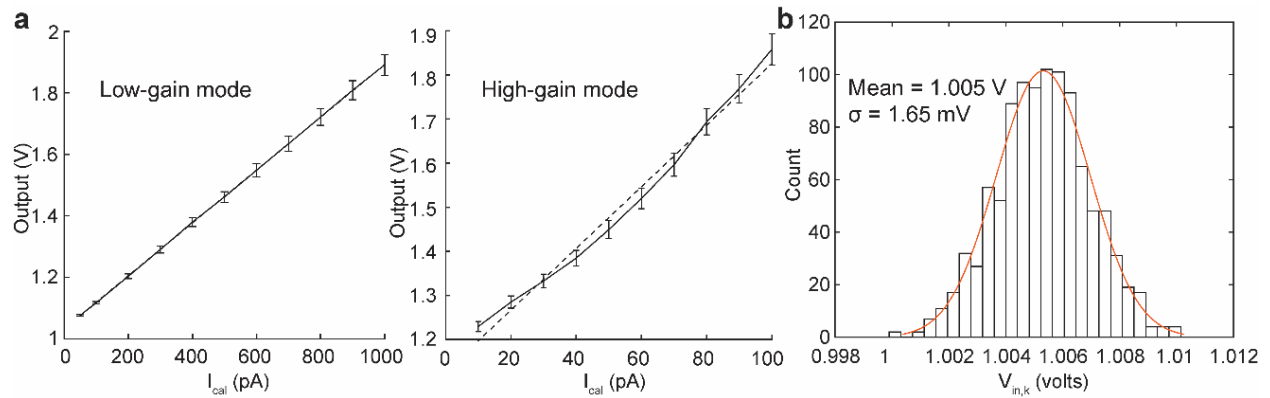
Figure 2.7 The current-to-voltage and mismatch characteristics of TIAs. (a) For each input current between 0 pA – 1000 pA, TIAs' outputs are plotted for both high-gain mode and low-gain mode. Based on the linear fittings, the transimpedance gains of each mode are 0.86 mV/pA and 7.00 mV/pA, for low-gain and high-gain modes, respectively. Linearity fittings indicate a high-quality linearity. The error bars are used to show the standard deviation of 32 TIAs. The dashed line shows the linear fits. The line's equation is $V_{out} = a + b \cdot I_{cal}$, where a = 1.03 V, b = 0.86 mV/pA for the low-gain mode, and a = 1.13 V, b = 7.00 mV/pA for the high-gain mode. (b) The voltage mismatch of each TIA for the entire array is 1.65 mV, which is a small variation due to the closely-matching transistor size (input transistor and load transistor). 2019 © IEEE

A custom-made LabVIEW program is used to control a National Instruments data

acquisition system automating the SRAM programming and measurement of each individual array

element's output as quickly as possible to reduce deviation due to environmental variables such as

temperature. Each measurement is used to plot a histogram of output voltage measured at the

ExConE (Fig. 2.7b). The measurement results in a mean output voltage of 1.005 V and a mismatch

standard deviation of 1.65 mV for the entire 1024 TIAs. Mainly, the large area investment to $M_{L,k}$

and M_k in each OPA (Fig. 2.2) contributes to the small deviation.

2.5.4 Bandwidth

In operating the TIA design, it is ideal to have the dominant pole of the transimpedance

measurement to be determined by the *sinc()* function created by the current integration (discussed

in Section 2.4.1) This can only be achieved if the other poles from the OPA and M_9 (in Fig. 2.3)

are higher than the pole from the *sinc()* function. The pole from the *sinc()* function is a function of

the integration window size based on Eq. 2.15,

$$sinc^2(f_{BW} \cdot \pi \cdot t_{int}) = \frac{1}{2}. \tag{2.17}$$

Thus, the pole can be determined based on the following expression,

$$sin(f_{BW} \cdot \pi \cdot t_{int}) - \frac{1}{2} \cdot f_{BW} \cdot \pi \cdot t_{int} = 0. \tag{2.18}$$

In the case when t_{int} is 100 μs, f_{BW} is ~4.43 kHz. So long as the other poles do not fall below

4.43 kHz, the dominant pole of this TIA design is the pole from the *sinc()* function.

The bandwidth of the half-shared TIA is measured using three different bias currents, 36.8

nA, 45.9 nA, and 55.4 nA, for each TIA. Phase compensation is also enabled. V_{pos} is set to 1 V. A

TIA is set to connect to ExConE, and the ExConE terminal is connected through a 1 MΩ resistor

to an analog output of a National Instruments data acquisition unit, allowing for the generation of

an AC sinusoid current to be applied to the amplifier. Various frequencies are input while the TIA

outputs are measured and plotted as shown in Fig. 2.8. When t_{int} is set to 100 μs, the TIA produces

the expected ~4.4 kHz bandwidth as well as the expected $sinc^2()$ aliasing sidelobes caused by the

integration period. For all three measurements, no observable difference is shown indicating that for any tested biasing levels, the OPA's pole remains higher than 4.4 kHz.

2.5.5   Crosstalk

A major concern for the half-sharing concept is crosstalk between shared channels. Although the small-signal analysis from section 2.3.2 shows that the design should not suffer from crosstalk, a measurement is presented in Fig. 2.9. For this measurement, row one columns one through four are measured. A 100 Hz sine wave of 400 µV peak-to-peak is injected into the chip's ExConE through a 1 MΩ resistor to produce a 400 pA peak-to-peak current signal. The row one column one TIA is configured to connect to ExConE so the TIA received this current input. Columns two, three, and four exhibit little to no crosstalk from the 100 Hz signal as demonstrated by Fig. 2.9. The noise floor discrepancy between the four channels is caused by parasitic capacitance being added to the input of the amplifier for column one due to its connection to ExConE and the wire leading to the signal generator.

2.6   Conclusion

In this chapter, we are presenting a simple half-shared amplifier structure which can be used for large-scale recordings. Analytical evaluation as well as simulation, and measurement of the fabricated circuit are discussed in detail to show the efficacy of the half-shared design and how it can scale into a large array without a significant trade-off. Many similar arrays require more die area for their amplifiers [34], [38], [39], [42], [49], [57]. Several arrays have increased throughput and reduced die area by using the half-shared architecture [34], [49]. Others have a high electrode
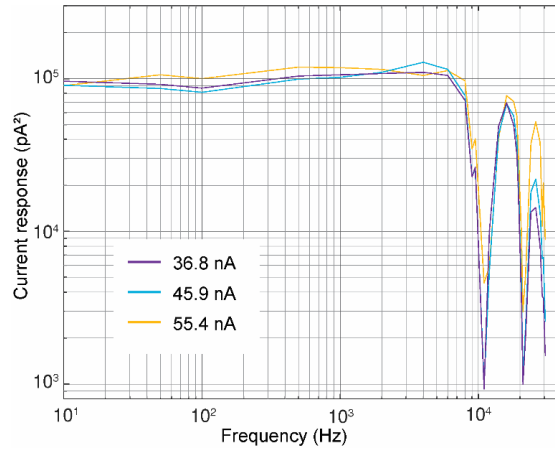
Figure 2.8: Frequency response showing the bandwidth of the TIA at different subthreshold biasing levels, 36.8 nA, 45.9 nA, and 55.4 nA. All recordings show near 4.4 kHz bandwidth which is caused by the dominant pole generated by the current integration performed at 10 kHz. This measurement indicates at any given biasing levels, the dominant pole is produced by the *sinc()* function, instead of the pole from the OPA. 2019 © IEEE

count, but a low amplifier count, disabling simultaneous full-array measurement [39], [42], [57].

This work builds on previous work and has a high electrode count, with simultaneous full-array measurement, enabled by the half-shared architecture. The performance of the array is compared with other similar arrays in Table 2-1. As discussed in Section 2.3.2, the measurement of each TIA does not suffer from crosstalk because the gain is completely independent (Eq. 2.9). One notable trade-off is the reduced dynamic range on each inverting input, due to the elevated V_{com}. A simulation method is presented which can closely estimate the noise performance of a non-stationary circuit, which has been traditionally difficult to analyze in the frequency domain. The transimpedance gain, mismatch performance, bandwidth, and crosstalk performance are measured from the fabricated circuit to validate the performance. This minimal deviation in mismatch will allow this CMOS device to be useful for most biosensor applications, including single-cell amperometry and nanopore-based nucleic acid measurements. It is interesting to note that, the common-mode rejection ratio (CMRR) of current-measurement amplifiers is not often discussed
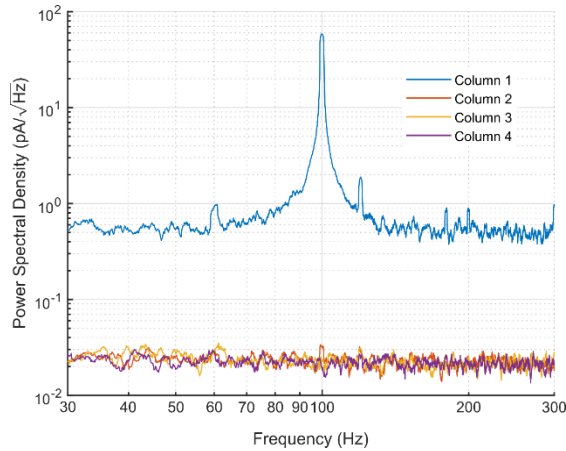
Figure 2.9: Measurement of a half-shared block's crosstalk performance. A 100 Hz signal is injected into column 1 via ExConE, the three shared amplifiers show a heavily attenuated signal present at 100 Hz. The rise in noise floor between column 1 and the others is due to the extra capacitance noise caused by the connection to ExConE and the wire to the signal generator. 2019 © IEEE

because the current signal source does not typically carry common-mode signals, in contrast to the voltage sources which almost always have a common-mode signal. However, the implication of the sharing structure to CMRR is worth studying and we are planning on conducting a future research project to investigate the CMRR of a TIA and how it can be quantified in both analytical and experimental settings.

Table 2-1: Comparison to Similar Amplifier Arrays 2019 © IEEE

Reference	[49]	[42]	[57]	[34]	[39]	[38]	This Work [8]
Technology Node	0.5 μm	0.18 μm	0.5 μm	0.5 μm	0.13 μm	0.18 μm	0.35 μm
Die Size	-	12 mm × 8.9 mm	2.5 mm × 2.5 mm	3 mm × 3 mm	3 mm × 2 mm	5 mm × 2.65 mm	5 mm × 5 mm
Number of Electrodes	25	59760	100	100	1024	200	1024
Amplifier Size	525 μm^2	≥0.04 mm^2	0.06 mm^2	900 μm^2	8000 μm^2	0.03 mm^2	90 μm^2
Simultaneous Channels	25	28	25 (4 to 1 multiplex)	100	4	200	1024
Noise performance	~ 110 fA$_{RMS}$	120 pA$_{RMS}$	7.2 pA$_{RMS}$	~ 100 fA$_{RMS}$	56 pA$_{RMS}$	480 fA$_{RMS}$ at 110 Hz filtered	415 fA$_{RMS}$
Bandwidth	2 kHz	16 kHz	11.5 kHz	~1 kHz	700 Hz	110 Hz - 10 kHz	4.4 kHz
Total Power	-	86 mW	2.1 mW	-	-	3.21 mW	12.5 mW

The presented method for reducing the die area required for OPAs in TIAs by half-sharing is an effective technique as demonstrated by measurements taken from the fabricated 0.35 μm CMOS chip. A four-way half-shared OPA scheme has proven to enable the miniaturization of 32 TIAs into the same space that would traditionally only be able to fit 17 TIAs, which is nearly 50% area reduction while retaining the similar performance. This enables future chips to be designed with an even higher number of electrodes and amplifiers for high-throughput biomedical measurements.

CHAPTER 3: PARALLEL 1024-CH CYCLIC VOLTAMMETRY FOR CMOS ELECTROCHEMICAL DETECTOR ARRAY CHARACTERIZATION

3.1   Chapter Notes

In this chapter, an electrochemical detector array was developed for parallel 1024 cyclic voltammetry recordings. Cyclic voltammetry, an electrochemical recording technique which monitors the electrochemical reactions at an electrode while sweeping the electrode potential, can reveal the nanoscopic contaminations of the electrode array which are not visible using a microscope. The electrode array can be contaminated after photolithography processing or by molecule adsorption. To remove this contamination the electrodes are treated with plasma to descum the surface of the electrode. Cyclic voltammetry can be used to examine the quality of electrochemical electrodes by measuring the double-layer capacitance that forms at the electrode-electrolyte interface as this capacitance is directly related to the effective area of the electrodes. Additionally, the bipolar capabilities for measuring both negative and positive electrochemical currents due to reduction and oxidation reactions are discussed in this chapter. The work described in this chapter was completed with Geoffrey Mulberry and Brian N. Kim [*].

3.2   Introduction

Large-scale microelectrode arrays (MEA) offer high spatiotemporal resolution for electrophysiology studies. MEAs have been useful in enhancing the spatial resolution of electrochemical recordings, such as mapping the level of H_2O_2 in relation to neurological diseases in a brain slice [31], electrochemical imaging of redox molecules diffusing across an MEA [32],

---

[*] In this chapter, we use material published in IEEE Sensors Journal, 2020 [115]

and imaging of metabolites in biofilms [33]. Large-scale MEA is especially useful in single-cell electrophysiology in which a large number of simultaneous recordings take place in order to account for heterogeneity in the characteristics of quantal release among the cell population [25]. For these reasons, high-throughput simultaneous measurements from a large number of cells would result in a tremendous benefit in enabling rapid studies of neurodegenerative disorders, the effects of therapies as well as new drug discoveries that target neurotransmitter release. Significant cost reduction in the single-cell electrophysiological analysis will also allow the evaluation of emerging treatments for side effects on molecular and cellular levels before it is clinically used.

A large number of electrodes in the MEA must be connected to external electronic amplifiers for signal amplification and processing. The use of external amplifiers becomes prohibitively expensive as the number of simultaneous recordings grows (for single-cell electrophysiology ~$15,000 per amplifier), but more importantly, it sets a limit on the total number of electrodes in an array because the external wiring becomes impractical. To resolve this challenge, complementary metal-oxide-silicon (CMOS) chips which monolithically integrate an amplifier for every on-chip electrode can be used. This method drastically lowers the cost per amplifier and removes the need for external wiring because the on-chip electrode and on-chip amplifier establish a connection within the chip. Therefore, the monolithic CMOS-based MEA opens the opportunity to increase the electrode count of an MEA to above 1000s. Previously, we have developed a monolithic CMOS-based MEA [24], [51], [61] using a 0.35-µm CMOS process for electrochemically measuring neurotransmitter secretions from single cells. We designed high-quality transimpedance amplifiers which can measure transient amperometric currents, resulted from the quantal dopamine release with sub-millisecond time resolution and pA current resolution.

38

Half-shared operational amplifiers were designed to maximize the number of amplifiers that can fit into a single CMOS chip to 1024 amplifiers, arranged in 32 columns × 32 rows. Measurements from the chip revealed low RMS amplifier noise levels ~400 fA at a 10-kHz sampling rate [24]. The noise performance of individual amplifiers in the CMOS chip closely matched that of high-end electrophysiology amplifiers [24], [34], [51], [61].

The quality control of individual electrodes (sensitivity and other electrical properties of electrode-electrolyte interface) becomes difficult as the number of electrodes increases beyond 1000. Microelectrodes are prone to damage or contamination which can affect the sensitivity and background noise. This is especially true if the device is made reusable and the device is used repeatedly. Therefore, the quality of microelectrodes must be individually evaluated after fabrication or repeated use by characterizing the electrodes for possible contamination and its effective surface area. This evaluation step is crucial to perform controlled analytical experiments using the well-characterized electrodes [57], [59], [62]. Because nanoscopic contaminations are not visible under the microscope, one of the effective ways of characterizing is using cyclic voltammetry (CV) which monitors the electrochemical reaction of the electrode while sweeping the applied potential (Fig. 3.1a). As such, it can be used to study various characteristics of the electrode, such as its impedance as well as sensitivity to oxidation and reduction reactions [57], [59], [62]. The large portion of the measured impedance is from the double-layer capacitance, created by the interface created between an electrode and the electrolyte, which is proportional to the effective surface area of the electrode-electrolyte interface (Fig. 3.1b). When the electrode is contaminated, the effective area to interface with the electrolyte is reduced, diminishing the sensitivity of the electrode. As the contamination is removed from the surface of the electrode, the

increased area of the electrode-electrolyte interface can be measured through the larger double-layer capacitance by CV (Fig. 3.1c). In order to evaluate a large electrode array with 1000s of
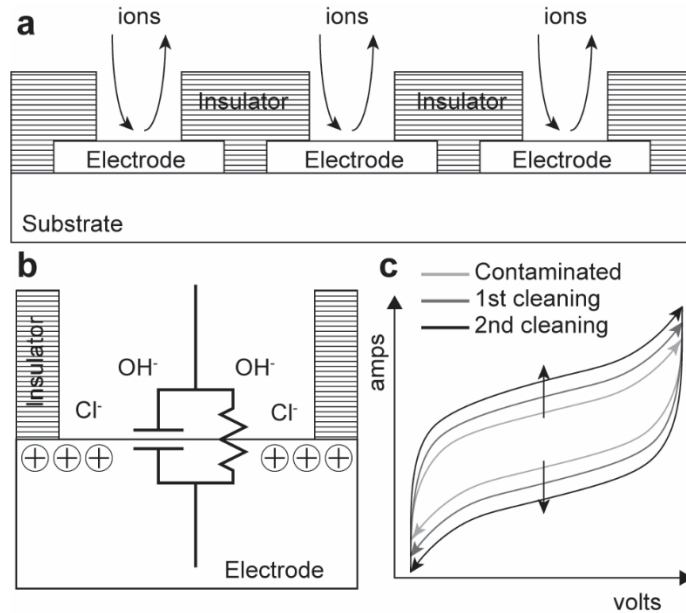
Figure 3.1: Double-layer capacitance and cyclic voltammetry progression of a contaminated electrode. (a) The electrolytic solution put on the CMOS electrochemical device introduces ions to the electrode. (b) The electrode is held at a potential for electrochemical measurements, attracting oppositely charged ions in the electrolytic solution and creating a double-layer capacitance at the electrode-electrolyte interface. (c) A contaminated electrode exhibits less sensitivity compared to a pristine electrode. As the electrode is cleaned, the progression of the response shows an increase in sensitivity. 2020 © IEEE

electrodes, parallel CV can be performed to collect the electrode-electrolyte interface capacitance from 1000s of electrodes simultaneously. This way the researcher can quickly determine the quality of the electrode array and apply an appropriate cleaning procedure, such as short piranha etching or plasma etching, before reevaluating the electrode quality until satisfactory.

In this chapter, we present the design of a monolithic CMOS-based MEA which has the parallel CV capability to perform the characterization of the integrated electrode array. Characterization of the electrode array reveals the state of the surface of individual electrodes.

Also, the effectiveness of plasma treatment towards removing contaminants is quantified through characterization of the electrode. In this chapter, electrode characterization is performed on the monolithic CMOS electrochemical detector array using parallel CV measurements. In Section 3.3, the design and performance of the designed bipolar transimpedance amplifier (TIA) are discussed as well as the methodology used to integrate the TIA into an electrochemical detector array. In Section 3.4, we discuss the post-CMOS processing used to integrate the electrodes and insulation onto the CMOS chip as well as parallel CV measurements on an electrode array. In Section 3.5, we discuss the characterization of the integrated electrode array on the monolithic CMOS device using CV before and after a plasma cleaning process.

3.3 Design of Bipolar Transimpedance Amplifier

To identify oxidation and reduction reactions using CV, bipolar current measurement is required. In this section, we detail the design of a bipolar TIA and its integration into a 1024 electrochemical detector array which enables CV measurements.

3.3.1 Bipolar Capacitive Transimpedance Amplifier

A TIA design based on the regulated cascode amplifier allows for a high-injection efficiency of input current which is beneficial in measuring small picoampere currents [49] (Fig. 3.2). Our TIA design uses an integrating capacitor to integrate the input current and convert it to voltage using the transimpedance gain. A TIA with a regulated cascode cannot inherently measure bipolar current because the cascode transistor only allows for a downward current direction. To enable bipolar measurement, we introduced a DC offset (I_{offset}) to the input of the TIA (Fig. 3.2a). With I_{offset} introduced as a baseline measurement, the current from electrochemical reactions at the

41

electrode (I_{elect}) can be either positive (+I_{elect}) or negative (-I_{elect}) due to oxidation or reduction respectively. Power consumption and area of the amplifier is minimized by using a simple design using five transistors for the operational amplifier (OPA) [24]. Negative feedback through the cascode transistor regulates the potential of the electrode to be the same as the non-inverting input V_{pos}. As the total current (I_{int}) is integrated onto the integration capacitor (C_{int}), the voltage of the readout node V_{out} is reduced. At a periodic interval (Δt), the total voltage drop is readout from the amplifier and C_{int} is reset during readout to begin the next integration cycle. This periodic interval determines the sampling rate of the amplifier. To achieve a 10 kS/s sampling rate, the period readout interval is 100 µs. In the absence of electrochemical reactions at the electrode, only I_{offset} is integrated resulting in a readout of ΔV_{offset} (Fig. 3.2a). During oxidation reactions, electrons are being released into the electrode, creating a current entering the electrode node which results in an integration current above the offset of $I_{int} = I_{offset} + I_{elect}$. The total integrated current is larger during oxidation, resulting in a larger readout of $\Delta(V_{offset} + V_{elect})$ (Fig. 3.2b). Conversely, in reduction reactions electrons are being taken from the electrode resulting in a total integration current below the offset of $I_{int} = I_{offset} - I_{elect}$. This reduction in integration will result in a smaller readout of $\Delta(V_{offset} - V_{elect})$ (Fig. 3.2c) during reduction reactions. To sustain the negative feedback of the amplifier, I_{elect} can be as low as -I_{offset} before the TIA effectively turns off. The TIA's transimpedance gain is determined by both C_{int}, estimated to be 116 fF, and Δt. Knowing the transimpedance gain, the bipolar dynamic range of the TIA is -I_{offset} to + ($C_{int} \times (V_{DD}-V_{pos})/\Delta t$) – I_{offset}. With a V_{DD} of 3.3 V, V_{pos} of 1.0 V, I_{offset} of 700 pA, C_{int} of 116 fF, and Δt of 100 µs, the dynamic range is -700 pA – 1968 pA.
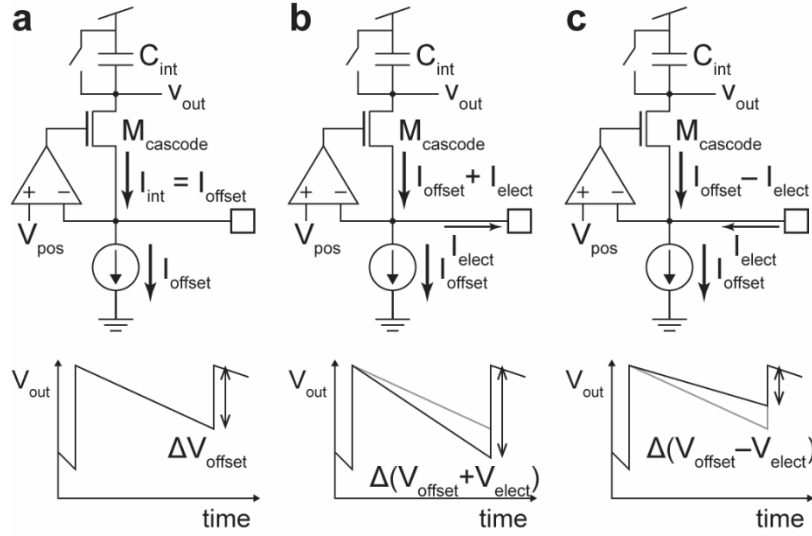
Figure 3.2: Designed bipolar capacitive TIA. (a) In the absence of electrons transferred to/from the electrode, only Ioffset integrated and ΔVoffset is readout. (b) During oxidation reactions, the current integrated is increased to Ioffset + Ielect, increasing the readout to Δ(Voffset + Velect). (c) During reduction reactions, the current integrated is decreased to Ioffset - Ielect, reducing the readout to Δ(Voffset - Velect). 2020 © IEEE

3.3.2 Bipolar Measurements and Characteristics

To validate the bipolar measurement functionality of the designed amplifier, an external current with both positive and negative polarity is injected into the electrode node of the amplifier while I_{offset} remains constant. The external current is injected by connecting an external l-GΩ resistor to the electrode node and applying a DC voltage to the other terminal of the resistor. Because the voltage at the electrode node is regulated through the feedback, the voltage drop across the resistor can be precisely controlled for current injection into the TIA. The linearity of the amplifier's output is studied by applying various levels of bipolar current. For this particular experiment, the non-inverting input V_{pos}, used to set the electrode potential, is set to 1.0 V. The external input current ranges from -700 pA – 700 pA by applying the DC voltage drop of -0.7 V – 0.7 V on the external resistor. The output of the amplifier, as the voltage applied to the 1-GΩ

resistor is changed by a small increment every 5 seconds, is shown in Fig. 3.3a and the reference of 0 pA corresponds to the integration of only the I_{offset} current, set to 700 pA. The recording showed a successful demonstration of bipolar transimpedance measurements. By mapping the output voltage versus the injected current, the linearity of the TIA can be determined as shown in Fig. 3.3b. The fit shown in the figure gives a transimpedance gain of 0.679 mV/pA with a coefficient of determination, R^2, of 0.998, indicating a high level of linearity for bipolar current measurement from -700 pA to 700 pA.
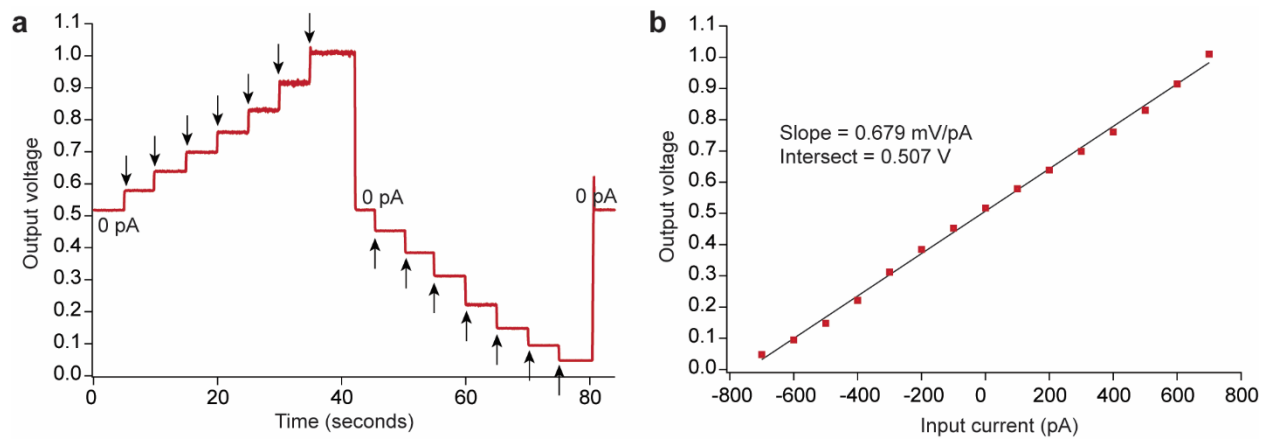
Figure 3.3: Bipolar current measurement of the designed TIA (a) Voltage readout of the TIA at different levels of current injected into the electrode. (b) Linear curve fitting illustrating the input current vs output voltage linearity. The TIA used exhibits a transimpedance gain of 0.679 mV/pA with an R2 value of 0.998, indicating the highly linear performance of the TIA. 2020 © IEEE

Further characterization of the amplifier's bipolar capabilities is studied by recording alternating signals. Alternating current is injected into the electrode node using the same method as above. A 1-MΩ resistor is chosen for this experiment to remove the influence of a zero in the frequency response to the circuit. Most component resistors have a parasitic capacitance near 500-fF and thus the zero created by the 1- MΩ resistor is ~318 kHz, which is outside of the sampling rate of 10 kS. The introduction of a zero can result in an inaccurate measurement by increasing the
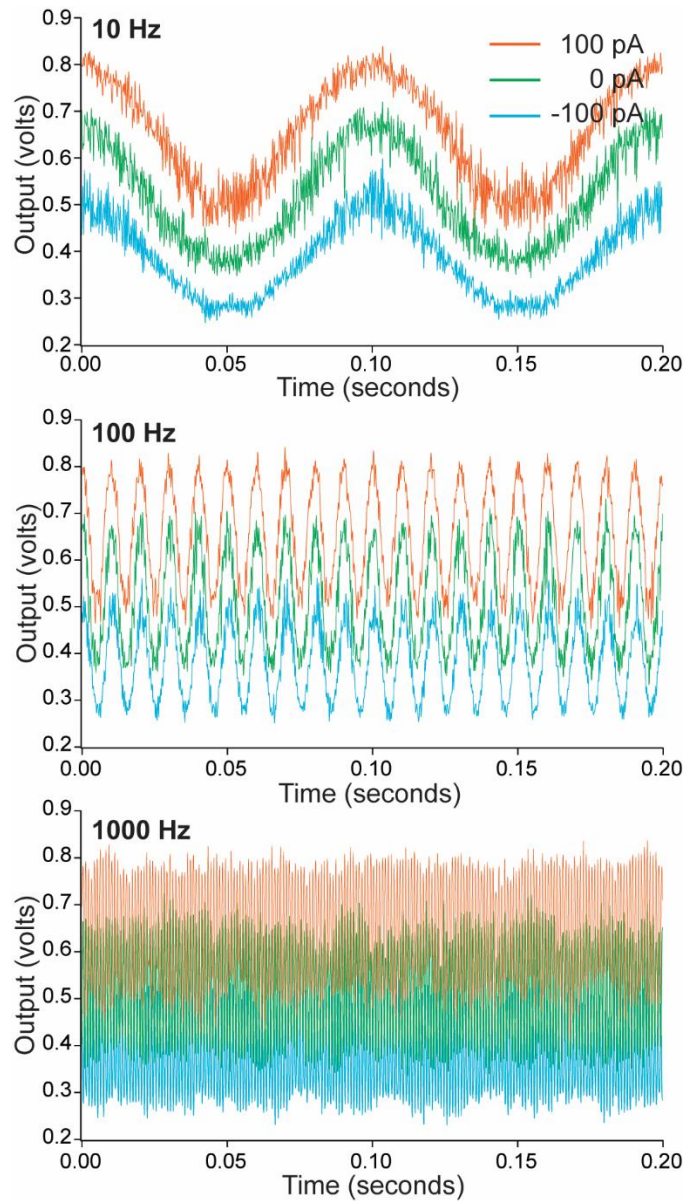
Figure 3.4: Measurement of alternating picoampere current at different levels of DC injection and at frequencies of 10, 100, and 1000 Hz. 2020 © IEEE

amplitude of the input current and distort the results in the low-frequency range. The tested cases are at frequencies of 10, 100, and 1 kHz with each frequency using the same AC amplitude of 200μV and at super-imposed DC levels of +100pA, 0pA, and -100pA (Fig. 3.4). The recordings validate the amplifier's ability to measure bipolar alternating current at various frequencies.

3.3.3 Integration of 1024-ch Amplifier Array

To integrate an array of amplifiers for parallel electrochemical measurements, a half-shared OPA structure is used, which has been previously studied [24], [61]. The purpose of the half-shared OPA design is to reduce the area required to create a dense sensor array by sharing one non-inverting input with multiple inverting inputs (Fig. 3.5). In the presented device, one non-inverting half of an OPA is shared by groups of 4 TIAs, each of which occupies 30×30 µm^2. The monolithic CMOS device, fabricated in a standard 2-poly 4-metal 0.35-µm process, has an array of 32×32 electrochemical detectors (Fig. 3.6a).

The entire array is operated through the application of two clock signals to the internal timing circuitry which generates a comprehensive set of clock signals required to achieve correlated double sampling, resetting of the integration capacitor in each TIA, and time-division multiplexing. To condense the output of the 1024 electrochemical detectors to 32 parallel outputs on a column basis, time-division multiplexing is used. The time-division multiplexing staggers the readout period, as well as the integration period, of the 32 rows in a column to minimize integration deadtime of the array.

3.4 Cyclic Voltammetry on an Electrode Array

It is common for semiconductor foundries to fabricate CMOS chips with an aluminum-copper alloy as the top metal layer. However, aluminum is highly reactive to electrolytic solutions and introduces significant offsets and shot noise to electrochemical recordings. To prepare the device for electrochemical measurements, post-CMOS processing is used to integrate polarizable electrode materials with low reactivity, such as platinum or gold, onto the CMOS chip.
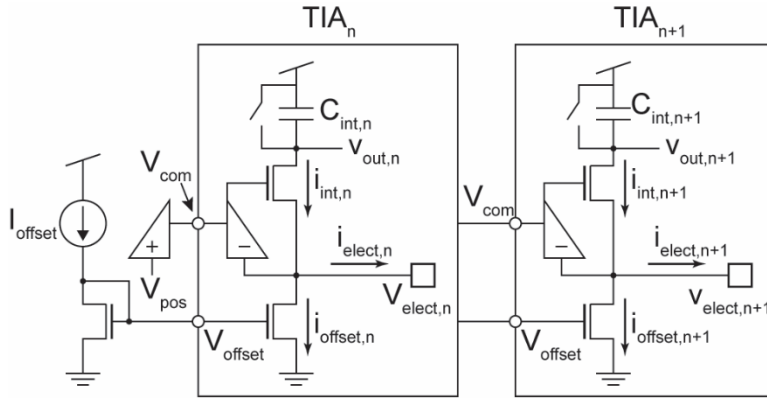
Figure 3.5: Half-shared OPA and TIA schematic. The non-inverting half of the OPA is shared among multiple TIAs. Each TIA has a dedicated electrode, integration capacitor, and current mirror generating Ioffset. 2020 © IEEE

3.4.1 Monolithic Integration of the Electrode Array

To integrate the platinum electrode array onto the CMOS chip, photolithography is used to perform a lift-off process. The chips are processed individually after they have been attached to a coverslip (25 mm × 25 mm) to ease the handling of the small devices (5 mm × 5 mm). After the chips have been attached to the coverslips, they are cleaned using acetone, isopropanol, and deionized water. For the lift-off process, a sacrificial layer of photoresist is created before metal deposition. This layer is created by spin coating, exposing, and developing a negative photoresist, NR9-1500PY, on the surface of the chip, removing photoresist where the electrodes will be patterned. The electrode materials are then deposited onto the processed chips, starting with the deposition of 20 nm of Ti and then 200 nm of Pt through sputtering (AJA Six-Gun Sputtering System, AJA International Inc., N Scituate, MA). After the metal is deposited onto the chip's surface, the sacrificial layer of photoresist is removed by rinsing the sample with acetone. Removal of the sacrificial layer leaves only the desired electrodes on top of the amplifier array.

To prepare the monolithic CMOS device for electrochemical applications such as single-cell amperometry, a biocompatible epoxy-based photoresist, SU-8 3010, is used to provide isolation between the electrodes in the electrochemical detector array (Fig. 3.6b). After the lift-off process has been completed, the chips are again cleaned with acetone, isopropanol, and deionized water. The SU-8 photoresist is spin coated, exposed, and developed for patterning. The SU-8 patterns are an array of 15 µm × 15 µm wells atop the electrodes. The SU-8 layer that remains on the surface of the monolithic CMOS device is approximately 20 –30 µm thick.

3.4.2 Cyclic Voltammetry on Individual Electrode

Cyclic voltammetry is demonstrated by applying a sweeping electrode potential from 1.2 – 2.0 V in a 20-second period while simultaneously measuring the electrochemical current resulting from reactions occurring at the electrode's surface (Fig. 3.7). Phosphate-buffered saline (PBS) (2mL) is placed on the electrode array and an Ag|AgCl reference electrode, which is connected to 1.2 V, is placed in the electrolytic solution to form the CV setup. As the potential of the integrated electrodes sweep from 1.2 – 2.0 V against the reference of the Ag|AgCl electrode that is held at 1.2 V, the resulting differential voltage drop at the electrode-electrolytic interface is 0 – 0.8 V (Fig. 3.7a), resulting in a CV scan rate of 80 mV/s. To increase the dynamic range for the CV measurements, the array is run at a sampling rate of 20 kHz. The time-domain current measurements from a representative electrochemical detector (Fig. 3.7b), comprised of a bipolar TIA and its platinum electrode, are done with and without PBS on the array. When there is no PBS on the array, the voltammogram in grey (Fig. 3.7c) shows a response that is predominantly resistive. After placing PBS on the array, the effects of the double-layer capacitance can be seen.
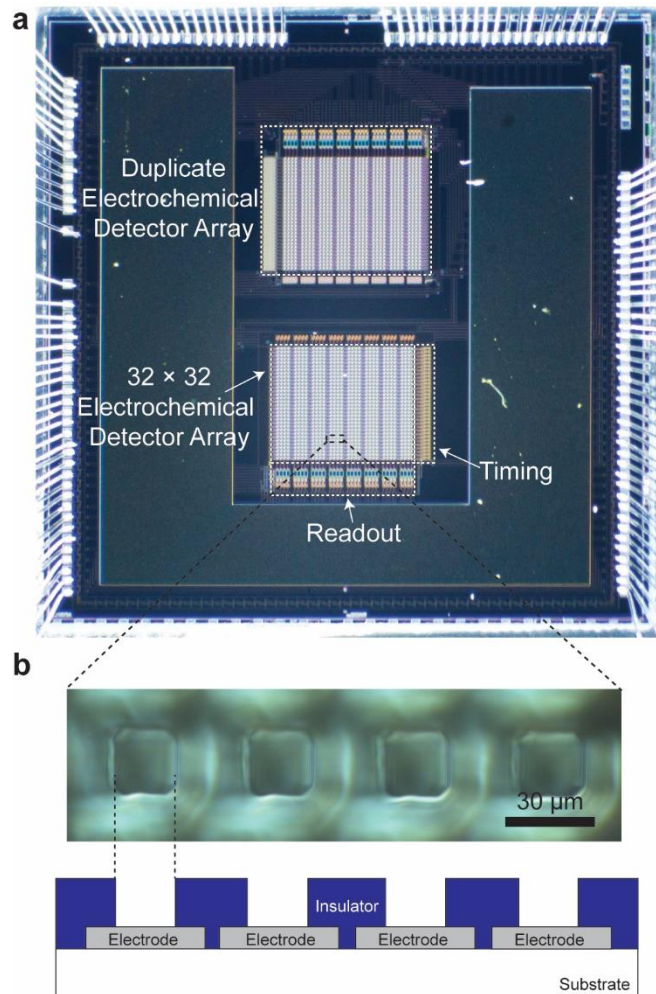
Figure 3.6: Photograph of the CMOS chip and the electrochemical detector arrays. (a) Microphotograph of the CMOS chip. To operate the array, two clocks are applied to the timing circuitry. The readout circuitry consists of the 32-to-1 multiplexers and output buffers to drive off-chip ADCs. A duplicate array is on the chip for characterization and testing. (b) The cross-sectional view of the electrode array and four electrodes with the focal plane set to the top of the insulator layer. 2020 © IEEE

This double-layer capacitance introduces a component to the measured current that reacts to change in the applied potential's slope (Fig. 3.7b). When dealing with a purely capacitive system, the capacitance can be found by measuring the current that results from the applied potential's slope through the relationship $C = I/(dV/dt)$. However, the presented system has both resistive and capacitive impedance. To remove the influence of current due to resistive impedance, the change

in current due to both the positive and negative cycles of the applied potential is examined. To maintain an objectiveness, 400 mV is chosen as a standard to review the change in current across the electrode array. For our CV setup, there is a change of 800 mV over a 10 s period for both the rising and falling cycles of our applied potential, resulting in a dV/dt of 80 mV/s. Examining this change in current at 400 mV and the symmetric slope of the applied potential (Fig. 3.7a), we can estimate the capacitance using the following Eq. (3.1):

$$C = \frac{\Delta I_{bipolar}}{2 \times \frac{dV}{dt}} \quad (3.1)$$

For this particular electrode (Fig. 3.7c), the bipolar change in current is 1.19 pA when the electrode array is dry and 104.8 pA when there is electrolytic solution on top of the electrodes. When the array is dry, the voltammogram exhibits 7 pF of capacitance. When electrolytic solution is placed over the array the calculated double-layer capacitance is 660 pF. This significant increase in capacitance demonstrates the dominant capacitance for our CV recordings is from the double-layer capacitance formed by the electrode-electrolyte interface.

3.5   Parallel Electrode Array Characterization

To study the quality of the monolithically integrated electrodes, parallel CV is performed to characterize individual electrodes. For the designed electrochemical detector array the input V_{pos} is shared across the array, enabling simultaneous CV measurements. When measuring from the array of electrodes the setup is as previously described, the integrated electrode is swept from 1.2 – 2.0 V, the reference electrode is held at 1.2 V in 2 mL of PBS, and the sampling rate of each amplifier is 20 kHz.
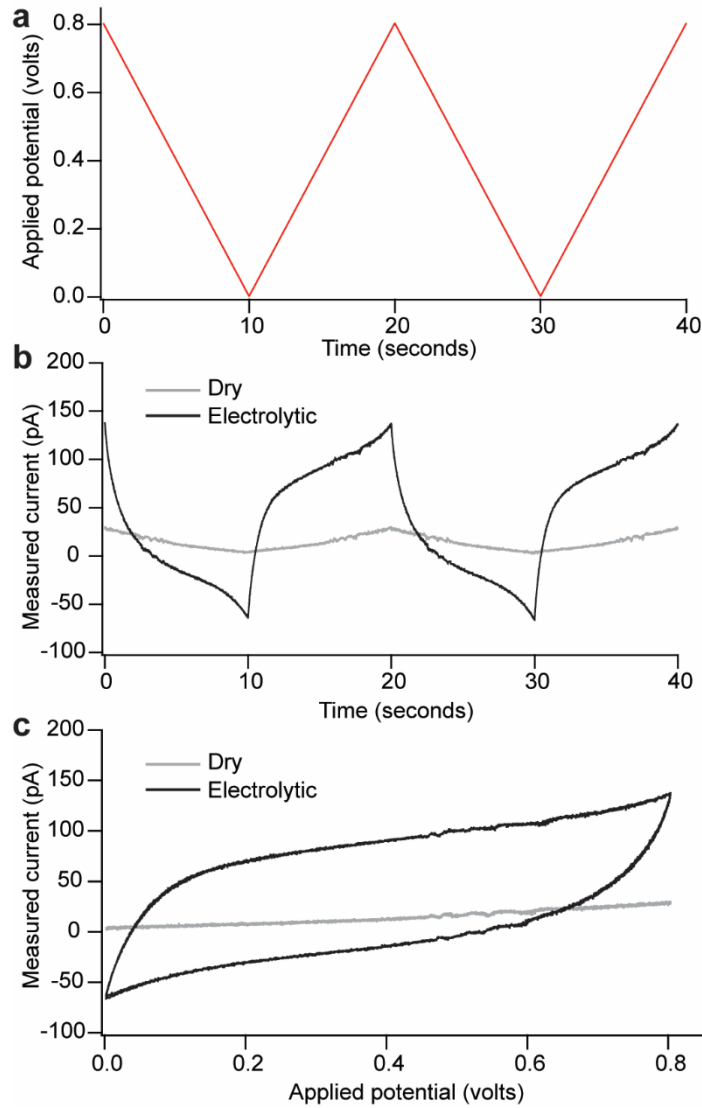
Figure 3.7: CV measurement from one TIA electrode. (a) Applied potential vs the reference electrode in the electrolytic solution. (b) Time-domain current measurement from a TIA when the device is dry and when PBS is put on the array. (c) Voltammogram of the measured current versus the applied potential. The dry measurement is nearly resistive, and the electrolytic measurement reveals the double-layer capacitance of the electrode. 2020 © IEEE

3.5.1   Electrode Surface Cleaning

After post-CMOS fabrication, cleaning of the electrode surface is required to ensure that the surface is pristine for use in electrochemical detections because contamination of the

electrode's surface reduces its effectiveness for electrochemical measurements. An electrode's surface can be contaminated during the photolithography processes as well as through repeated use of the electrode for electrochemical measurements. In post-CMOS processing, the last step to create an insulation layer using SU-8 has been reported to often leave a thin film on the electrodes after development [63], [64]. Also, molecules, such as dopamine, can also adsorb onto the surface of the electrode [65], [66] after an electrochemical measurement and reduce the sensitivity of the electrode [67]. In this study, we used a plasma cleaner (PDC-32G, Harrick Plasma, Ithaca, NY) to remove organic material from the surface of the electrodes using ionized gas.

3.5.2 Parallel Cyclic Voltammograms

The resulting voltammograms from one parallel CV recording are shown in Fig. 3.8. The levels of contamination of an electrode array can be monitored by measuring the double-layer capacitance across the array through parallel CV recordings. As the area of the electrode's surface is contaminated, the effective area that creates an interface between the electrode and the electrolyte, the double-layer capacitance, is reduced. Modeling the double-layer capacitance as $C = \varepsilon A/d$, the reduction of the electrode-electrolytic interface area (A) is directly related to the reduction of capacitance. The electrochemical electrode array, which was previously used for several experiments involving the oxidization of dopamine, is used for electrode array characterization using CV (Fig. 3.8, orange trace). The recorded set of voltammograms is used to calculate the double-layer capacitance formed at each electrode-electrolytic interface. The average capacitance of the electrode array is 0.47 nF with a standard deviation of 0.14 nF. To remove the contaminants, the electrode array is given a 10-minute plasma treatment, and the response of the

electrodes is re-characterized (Fig. 3.8, red trace). The mean capacitance of the array after plasma treatment is 1.36 nF with a standard deviation of 84.5 pF, nearly tripled compared to the initial characterization. The increased mean capacitance reveals that the electrodes could have been previously contaminated and plasma treatment improved the surface condition, increasing the area of the electrode-electrolyte interface and thus the double-layer capacitance.
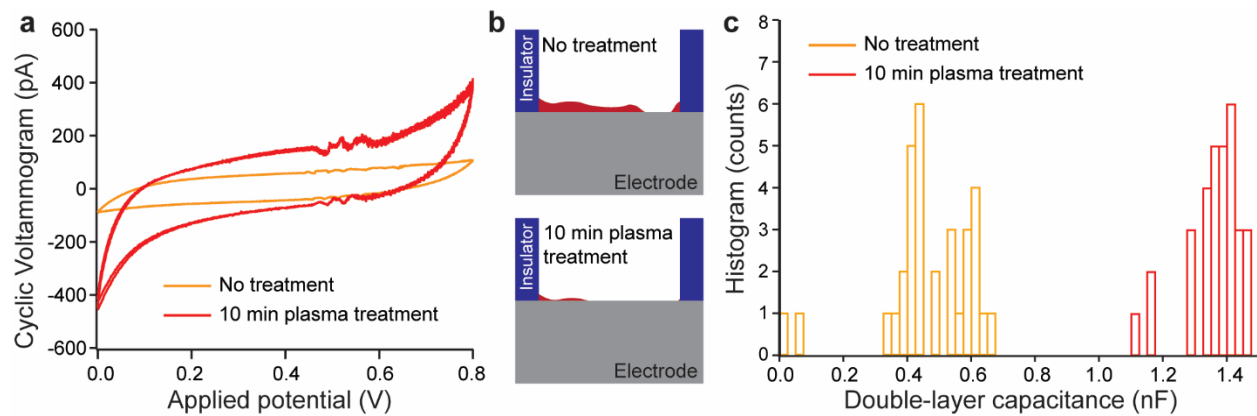
Figure 3.8: CV recordings from an electrode array. (a) A representative CV of an electrode before and after 10-min plasma treatment. The electrodes are initially contaminated and exhibit reduced sensitivity as shown in the orange lines. (b) The electrode with contamination on the surface can have reduced surface area where the plasma treatment is anticipated to increase the surface area by etching the contaminant. (c)After plasma treatment, the capacitance of the electrode array is increased consistently throughout the array, reflecting the increased surface area. 2020 © IEEE

3.6   Conclusion

In this chapter, we study the quality of an electrode array through parallel CV measurements, as well as present the design and performance of a bipolar capacitive TIA used in a 1024-channel monolithic CMOS device for high-throughput electrochemical recordings. The presented capacitive TIA is capable of measuring bipolar current from oxidation and reduction reactions through the introduction of a DC offset, I_{offset}. The bipolar capabilities of the capacitive TIA are demonstrated by measuring alternating current that is injected into the electrode node.

Integration of the bipolar capacitive TIA for large-scale parallel electrochemical recordings in a 1024-channel CMOS device is achieved through the use of the half-shared OPA structure. Through post-CMOS processing, the platinum electrode array and the SU-8 insulation is monolithically integrated on the CMOS device. To examine the quality of the electrode array after repeated use for electrochemical recordings, parallel CV is performed before and after plasma treatment. The contaminations on the electrode surface, such as adsorbed molecules or a thin film of photoresist, reduce the effective area for the electrode-electrolyte interface and thus the double-layer capacitance. After plasma treatment of the electrode array, the capacitance increased substantially, indicating that the surface of the electrodes could have been contaminated and plasma treatment improved the surface of the electrode, thus increasing the electrode-electrolyte interface and the double-layer capacitance. Using parallel CV, characterization of the 1024 electrode array can be accelerated and conducted within minutes before it is used for analytical purposes.

CHAPTER 4: MULTIFUNCTIONAL DATA ACQUISITION SYSTEM FOR HIGH-SPEED 1,024-PIXEL CMOS ELECTROCHEMICAL SENSING

4.1   Chapter Notes

Here, we developed a multifunctional data acquisition system that enables high-speed 1024-pixel CMOS electrochemical imaging. Fast electrochemical imaging of the diffusion of dopamine and hydrogen peroxide is recorded at 40,000 frames per second across the 32×32 neurochemical detector array and presented in this chapter. To support the high level of data generated by the neurochemical detection array, a custom data acquisition system is designed to interface with the high-density neurochemical detection array. The FPGA-based acquisition system discussed in this chapter provides an interface to control the neurochemical sensing array with a computer. Additionally, the system's data acquisition capabilities transfer the high-density of detected neurochemical signals to a computer for further analysis. The work described in this chapter was completed with Matthew A. Crocker and Brian N. Kim.

4.2   Introduction

Recent advancements have provided enhanced spatiotemporal resolution for electrochemical studies such as the imaging of diffusing electroactive molecules [32], [51], detection of toxic metabolites such as pyocyanin [68], [69], and mapping of H_2O_2 levels, in association with neurological diseases, throughout a brain slice [31] using electrochemical sensor arrays. Using electrochemical techniques, the redox molecules present in electrochemical studies will either release electrons, oxidization, producing a negative current as the electrons are accepted by the electrode, or will take electrons from the electrode, reduction, producing a positive current.

For example, the presence of neurotransmitters, such as dopamine, can be studied by direct measurement of the released electrons during an oxidation reaction at an electrode. The dynamics of redox molecule diffusion may only last milliseconds to microseconds, as such, the high temporal resolution provided by electrochemical recordings provides a unique advantage in capturing details of the reaction. Additionally, it is possible to be highly specific to, and highly sensitive of, the electroactive molecules using electrochemical detection techniques. To further enhance the high specificity and temporal resolution of electrochemical recordings, the miniaturization and parallelization of the electronics and sensors is prevalent in emerging devices that explore the integration of microelectrode arrays (MEA) and complementary metal-oxide-semiconductor (CMOS) technology. The parallelization of the sensor array enables the construction of spatial data sets based on the sensor array's geometric arrangement. However, as the electrode count of MEAs increases, the expansion of parallel electrochemical recordings introduces an instrumentation challenge. Direct wiring of electrodes to their corresponding amplifiers becomes impractical and using commercially available amplifiers is costly. To support the increasing throughput of electrochemical recordings, CMOS technology is being explored as an interface, as it can provide arrays of readout circuitry which amplify and process the electrochemical signals detected by MEAs. Through on-chip integration of MEAs, interconnections are simplified and readout circuitry is scalable, allowing large-scale electrochemical sensor arrays on small silicon chips. Recently developed devices include an array of 59,760 electrodes capable of up to 2048 simultaneous recordings [36], [42], an array of 10×20 electrodes with the capability of performing voltammetry as well as amperometry [38], a 32×32 array that provides electrochemical images

at 90 frames per second [32], and an array of 100 electrodes for up to 100 parallel recordings of neurotransmitter release from chromaffin cells [34], [64].

The monolithic integration of the electrochemical sensors simplifies the connections between the electrodes and the readout circuitry, but an external data acquisition system remains necessary to support the operation of the complex functionality of the sensor arrays and transfer of the recorded electrochemical signals to a computer for storage and analysis. The external system can be simplified through the integration of analog-to-digital converters (ADCs) in the CMOS chip. However, the integration of ADCs in the CMOS chip requires a large area, as such, it can be preferable to instead use external ADCs. Additionally, external ADCs have additional benefits, such as cost-effectiveness, as a direct result of the sensors generally being treated as single-use devices, due to their need to make direct contact with the biological or chemical substances being investigated. Future advancements in biotechnology will require high-throughput data acquisition to enable high-throughput gene sequencing [35], [70], high-throughput drug screening studies [39], [71], high density brain-machine interfacing [72]–[74], and high-throughput single-cell electrophysiology [24], [34], [64]. To support high-throughput applications, the external acquisition system must support fast analog-to-digital conversion, extensive data transmission, and highly parallelized signal processing. For an electrochemical imaging device with 1,000 sensors operating at 40,000 frames per second, a minimum cumulative sampling rate of 40 million samples per second (S/s) is required. If 16-bit ADCs are used for digitization, 2 bytes are created per sample and the minimum data transmission rate is 80 Mbytes per second (MB/s). Redundant sampling can improve the noise and accuracy of recorded electrochemical signals, however, the minimum data transmission speed will increase by a factor of two or more [34]. A high-performance acquisition

system was designed using commercially available data acquisition modules and is capable of digitizing 16 analog inputs at a maximum sampling rate of 120 MS/s at a 16-bit resolution [75], [76]. However, this system is very costly and lacks a sufficient number of analog inputs for a high-throughput CMOS device used for parallel recordings of neurotransmitter release from single cells [24], [51], [61]. As an alternative to commercially available systems, low-cost data acquisition systems have been presented using Arduinos [77] and custom acquisition systems controlled by microcontrollers [78] or field-programmable gate arrays (FPGAs) [79], [80]. However, the sampling rates of these alternative systems are inadequate for high-throughput electrochemical imaging with fine temporal resolution. To support the data transmission demands for high-throughput applications, the selected interface must be taken into account. Common interfaces used for data acquisition systems are universal serial bus (USB), peripheral component interconnect (PCI), and PCI Express (PCIe). Among these interfaces, USB is the most accessible due to its availability on virtually all desktop computers as well as laptops, whereas PCI and PCIe interfaces are limited on desktop computers and require external adapters for use on laptops. For high-throughput electrochemical imaging, the growing prevalence of the USB 3.0 interface provides sufficient data transmission at up to 625 MB/s and broadens the applications of data acquisition systems outside of well-equipped research laboratories. By using the power delivered through the USB interface, ranging from 4.5 watts (W) for USB 3.0 and up to 15 W for type-C, the data acquisition systems can be designed for applications requiring portable high-performance devices.

In this chapter, we present the design of an electrochemical sensing platform that is capable of 1024 simultaneous electrochemical recordings at a frame rate of 40,000 per second, one of the

fastest devices reported to date with high spatial resolution. The designed system provides significant benefits for studies that require high-throughput and high spatial and/or temporal resolution, such as high-throughput single-cell amperometry to study the mechanisms of neurological diseases, the mechanisms of vesicle secretion, and the dynamics of neurotransmitter release. In the following sections, the design of the 1024-pixel electrochemical imaging sensor will be presented alongside the custom data acquisition system that enables the frame rate of 40,000 frames per second. In section 4.3.1 the design of the CMOS electrochemical detector is discussed, while in section 4.3.2 the post-processing stage of the CMOS chip is discussed. Section 4.3.3 discusses the packaging of the CMOS chip to ensure the device is both biocompatible and waterproof. In section 4.3.4 the data acquisition system and its parts are discussed, while in section 4.3.5 the design of the FPGA architecture is discussed. Section 4.3.6 presents the experiment taken to characterize the noise performance of the data acquisition system and 4.3.7 presents the experimental procedures for the electrochemical imaging of dopamine and H_2O_2 diffusion using the designed electrochemical imaging sensor. Section 4.4.1 discusses the noise characterization of the data acquisition system and section 4.4.2 discusses the successful imaging of dopamine and hydrogen peroxide diffusing over the electrochemical sensor array.

4.3   Material and methods

4.3.1   CMOS Electrochemical Detector Design

For two-dimensional imaging of dopamine diffusion, a CMOS device with an electrochemical detector array is designed to measure the electrochemical signals from electroactive molecules diffusing on the surface of the chip in parallel. The signals from these molecules are small currents that range from pA to nA. To record these small currents, an

electrochemical detector is designed which consists of an integration capacitor-based

transimpedance amplifier (TIA) and an on-chip electrode as described in section 4.3.2 (Fig. 4.1).
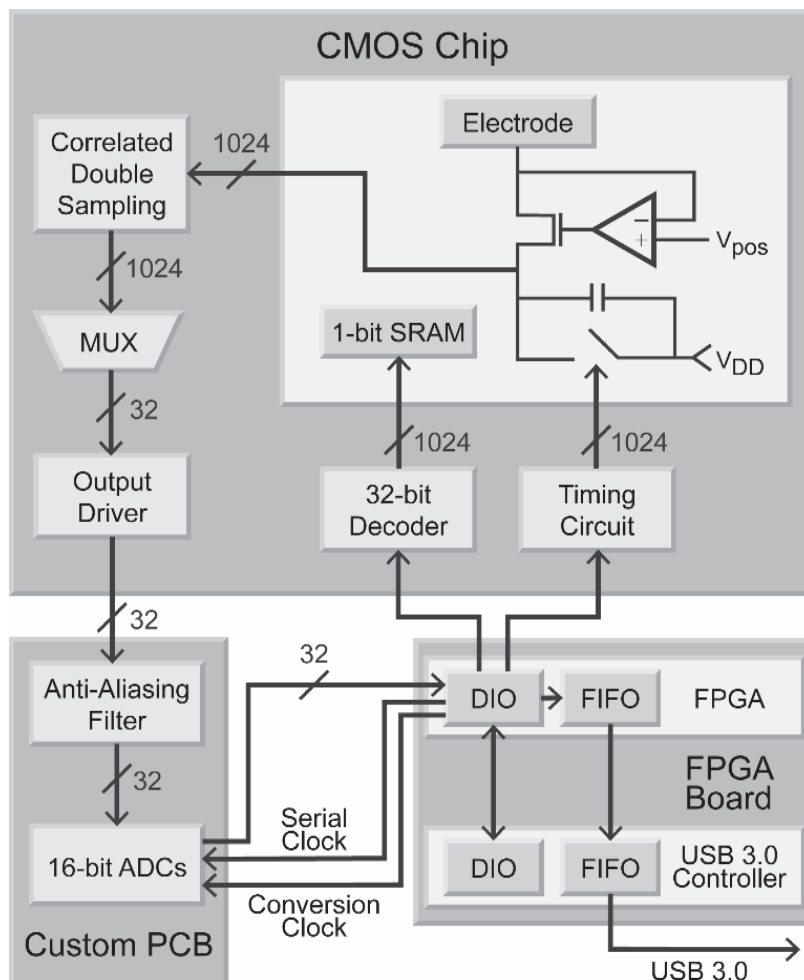
Figure 4.1: Overview of the electrochemical imaging system's architecture.

To set the voltage of the electrode to a redox potential for electrochemical experiments, the

feedback through the operational amplifier (OPA) regulates the voltage of the electrode to be equal

to the OPA's input, V_{pos}. As electrons flow through the electrode by way of oxidation or reduction,

the current resulting from an electrochemical reaction is integrated onto a capacitor. To minimize

the reduction of the electrochemical current due to the input impedance of the TIA, a regulated

cascode topology is used for high injection efficiency [49]. The integration of current on the capacitor results in a reduction in voltage at the TIA's readout node. The voltage at the readout node is read periodically and the voltage of the integration capacitor is reset during the readout phase to start the next integration cycle. The length of the periodic readout and subsequent reset of the integration capacitor determines the sampling rate of the TIA. To achieve a 40 kS/s sampling rate, the periodic readout occurs every 25 µs. The designed TIA occupies an area of 30×30 µm^2 and also includes a 1-bit static random-access memory (SRAM) to enable testing circuitry or adjustment of the total integration capacitance, thus changing the current to voltage gain of the TIA.

To enable large-scale electrochemical recordings, the CMOS chip has an array of 32×32 electrochemical detectors. The recordings of the 1024 detectors is reduced to 32 parallel outputs, on a column basis, using time-division multiplexing. Time-division multiplexing sequentially staggers the readout period of the rows such that one detector is being read while the rest are integrating, eliminating dead time due to readout [24]. To operate the integrating TIAs and multiplex the 1024 electrochemical detectors, the timing circuits are designed to generate all necessary signals using two external clock inputs. To send the electrochemical recordings to a computer for analysis, the CMOS chip interfaces with external ADCs in the FPGA-based data acquisition system described in Section 4.3.4. The multiplexed outputs of the detector array are fed into output buffers in order to drive the capacitive load from the output lines, bonding pads, and the input capacitance of the ADCs. The CMOS electrochemical detector array is designed using Cadence Virtuoso Analog Design Environment and fabricated using a standard 2-poly 4-metal 0.35 µm CMOS process.

4.3.2   Post-CMOS Processing

A common material used for the top metal layer for CMOS fabrication is an aluminum/copper alloy, which is reactive to solutions used for electrochemical experiments and is inadequate for applications requiring high signal-to-noise performance. To achieve a high signal-to-noise ratio, polarizable electrode materials, such as platinum or gold, are used because of their low reactivity to electrolytic solutions. Through post-CMOS processing, an MEA using a polarizable material, platinum, is integrated onto the surface of the CMOS chip. To integrate the MEA onto the device, a lift-off process is used, this process is accomplished through photolithography using negative photoresist. The lift-off process starts by creating a sacrificial layer of photoresist, patterning the desired electrode patterns into the sacrificial layer permitting access to the surface of the CMOS chip, deposition of metal materials, and removal of the sacrificial layer, leaving only the desired electrode patterns on the surface of the device. Prior to the photolithography process, each CMOS die (5 mm $\times$ 5 mm) is bonded to a coverslip (25 mm $\times$ 25 mm) using epoxy in order to reduce the complications of handling small samples for post-CMOS processing. The bonded die is then cleaned by bathing it in acetone, isopropanol, and then DI water. The bonded die is spin coated with a negative photoresist, NR9-1500PY, to cover the surface of the device. The device is then put into a contact aligner (EVG 620, EV Group, St. Florian am Inn, Austria) with a custom-designed photomask to correctly position the desired MEA pattern on the CMOS chip. The chip is exposed to UV light in the aligner and then developed to remove photoresist from the surface of the device where metal deposition is desired. To integrate the platinum MEA, 20 nm of Ti is first deposited to act as an adhesion layer between the Al/Cu and Pt, then 200 nm of Pt is deposited using a sputtering machine (AJA Six-Gun Sputtering System,

AJA International Inc., N Scituate, MA). To remove the sacrificial layer of photoresist, the dies are repeatedly rinsed with acetone and the layer of NR9 photoresist washes away. The metal that is deposited on top of the NR9 layer is removed from the device completely, leaving only the desired MEA as patterned during UV exposure. To prepare the CMOS device for single-cell electrophysiology [24], a biocompatible epoxy-based photoresist, SU-8, well structure is created atop each electrode throughout the array to permit one cell to sit atop each electrode for single-cell recordings and to reduce the effects of adjacent electrodes and cells [24]. The wells are created through a subsequent photolithography process using SU-8 3010 negative photoresist. After the lift-off process, the dies are cleaned by bathing the chips in acetone, isopropanol, and then DI water. The chip is spin coated to cover the CMOS chip with SU-8 photoresist, exposed to UV light using a contact aligner (EVG 620, EV Group, St. Florian am Inn, Austria), and a second image on the designed photomask containing an array of well structures that are 15 μm × 15 μm in size. Finally, the exposed SU-8 is developed to remove undesired SU-8 from the surface of the CMOS chip and permit access to the platinum electrodes throughout the MEA.

4.3.3   Biocompatible Packaging

After the MEA is integrated onto the CMOS chip, it is bonded onto a custom-designed PCB die holder using epoxy. After the epoxy has cured, the pads on the CMOS chip are wire bonded to the PCB pads to provide an interface between the CMOS electrochemical detector array and the external data acquisition system. To protect the wire bonds when handling the device, and from liquids during electrochemical experiments, a 3D-printed well made of acrylonitrile butadiene styrene (ABS) plastic is coated with polydimethylsiloxane (PDMS), for waterproofing

and biocompatibility, and then bonded to the surface of the CMOS chip using additional PDMS. The custom-designed ABS well provides an opening to access the surface of the CMOS device and accommodates 2mL of liquid for electrochemical experiments [24].

4.3.4 Design of FPGA-based Data Acquisition System

To operate the integration and readout functions of the electrochemical detector array and to read the data output from the array, an FPGA-based data acquisition system is developed to interface with the CMOS chip. The acquisition systems includes 32 ADCs with 16-bit resolution, 1 adjustable regulator, 16 digital inputs and outputs (DIO), and a USB 3.0 SuperSpeed interface. The acquisition system consists of an Opal Kelly FPGA board and a custom-designed PCB (Fig. 4.2). On the FPGA board, there is a Cypress FX3 chip that provides a SuperSpeed USB 3.0 interface that can receive commands to control the IO of the Kintex-7 FPGA chip. The FPGA chip generates the DIO used to operate the electrochemical detector array, such as providing the clock signals for the CMOS' internal timing circuitry, and receives the parallel streams of data from the 32 parallel ADCs. To achieve synchronous operation of the electrochemical detector array and the ADCs, the FPGA generates all clock signals used throughout the electrochemical sensing system.

On the custom-designed PCB, there are 16 ADC chips (LTC2323-16, Liner Technology), each of which have two embedded ADCs that can individually sample their respective inputs up to 5 MS/s, providing 32 high-speed 16-bit ADCs (Fig. 4.2). A 4-pole Low-Pass filter is designed using the Sallen-Key topology and is used as an anti-aliasing filter for each ADC. The ADCs convert the 32 parallel outputs of the electrochemical detector array to their 16-bit digital representations and then sends this data serially to the DIO pins of the FPGA. The received data

is then processed and packaged by the FPGA to be transferred to a PC through the USB 3.0

interface chip.
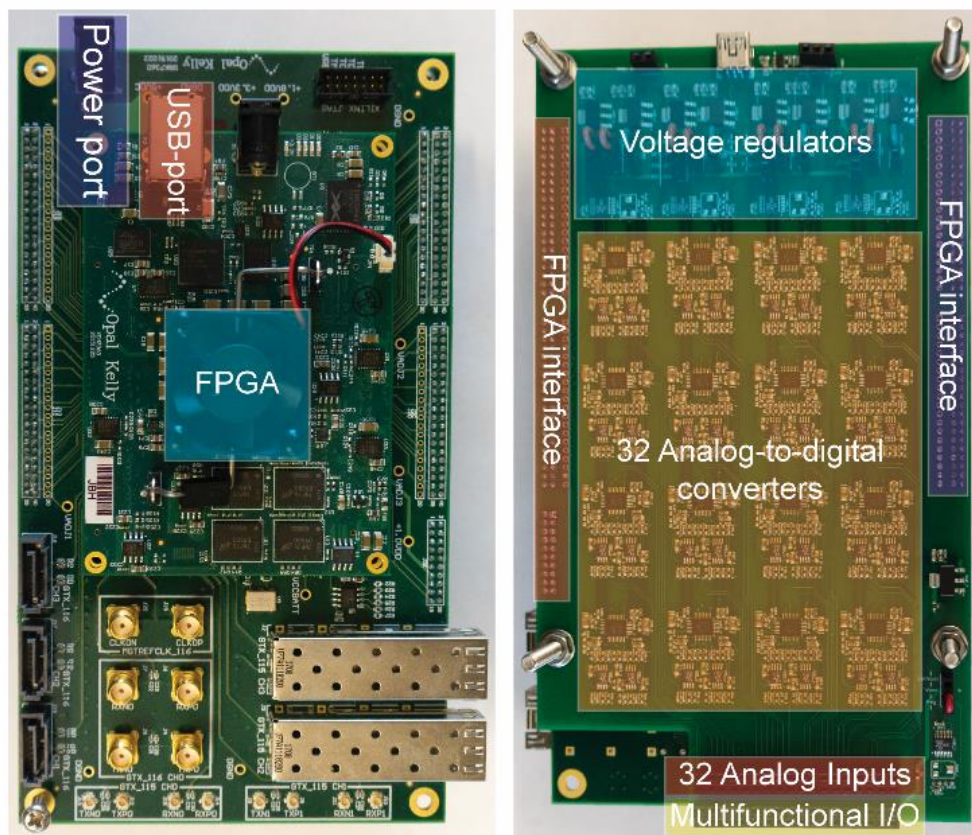
Figure 4.2: Images of the FPGA-based data acquisition system. (left) The system uses a USB 3.0 interface to interface with a computer to receive data from the electrochemical imaging array and send commands to the FPGA chip, which controls all clock signals and digital IO. (right) 32 parallel ADCs simultaneously digitize data from the 32 parallel outputs of the electrochemical imaging device.

4.3.5   FPGA Architecture

The architecture of the FPGA consists of clock generation, shift registers for parallel serial

streams of data, a first-in, first-out (FIFO) data manager, and a USB 3.0 interface to control the

functionality of the electrochemical sensing system and send data to a computer (Fig. 4.3). Using

a 200 MHz oscillator as a master source, the FPGA synchronously generates all of the clocks

required to initiate sampling and readout of the ADCs as well as integration and readout of the electrochemical detector array. The generated clocks are subdivided from a master clock of 128MHz into 32 MHz, 2.56 MHz, 1.28 MHz, and 40 kHz. In addition to synchronously running the CMOS chip and the ADCs, the generated clocks are also repurposed inside the FPGA to operate the input shift registers and the FIFO. The 40 kHz clock initiates the readout for the first row in the electrochemical detector array, and the 2.56 MHz clock propagates the readout period across the 32 columns to the next row in the array while also returning the previous row to an integration period, resulting in an effective frame rate of 40,000 frames per second. With a 2.56 MHz operation frequency for the CMOS chip, the output rate of the columns results in a 1.28 MHz signal. Each of the 32 ADCs sample the 32 parallel CMOS outputs simultaneously at 1.28 MHz
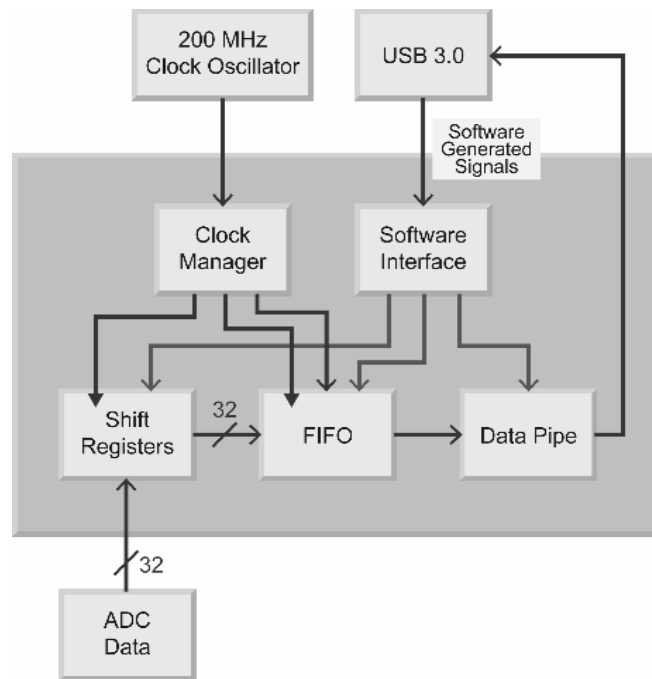
Figure 4.3: An overview of the FPGA's architecture. Data from the ADCs is serially output to 32 parallel pins on the FPGA chip, where it is processed and packaged before being transferred to the computer through the USB 3.0 interface. The data is stored in a FIFO queue until the data is requested through the FPGA's API, once a request is made the data will be transmitted through the USB 3.0 interface.

and the 16-bit digital conversions are output from the ADCs in serial data streams at a rate of 32 MHz. The data from the ADCs are input to shift registers in the FPGA to allow parallel processing of the data. The data from the ADCs is then packaged through column-based multiplexing so that the first data package contains the data from column 1, the next package contains data from column 2, and so on. The packaged data is then passed into a FIFO data queue that continuously fills until the computer asks for data from the FPGA via USB 3.0 interface. The connected computer uses a C++ program to send the system reset signals and initialize the system prior to data collection. To obtain the data stored in the FIFO, requests are made through the FPGA's application programming interface (API). The program allows the desired data amount to be specified and multiple sets of data to be continuously transferred, useful for multiple successive experiments.

4.3.6   Characterization of Noise and Performance

To characterize the noise performance of the inputs to the data acquisition system, a linear voltage regulator is powered by one 9V lithium-ion battery and used as an input to the custom PCB, wherein the input is first filtered by a 4-pole anti-aliasing filter and then input into an ADC, for our noise characterization. The linear regulator is set to output a voltage of 0.92 V, which is the output voltage of the CMOS chip when no current is integrated by the TIA. The input to the data acquisition is recorded for ~12s so that the noise spectrum can be examined down to ~0.1 Hz.

4.3.7   Experimental Procedure for Electrochemical Imaging

To demonstrate the capabilities of the electrochemical sensor array, the diffusion of dopamine and hydrogen peroxide are recorded. For the dopamine diffusion experiment, 1mL of a phosphate-buffered saline (PBS) solution is first added to the electrochemical sensor's well and a

reference Ag|AgCl electrode is connected to ground and put in the well. To ensure that no bubbles are blocking access to the electrodes throughout the array, preventing an interface between the electrode and the electrolytic solution used for electrochemical experiments, the sensor and solution is agitated until no bubbles remain. When performing consecutive experiments, the electrolytic solutions used are never fully removed from the well to avoid drying of the electrodes, thus preventing bubbles from reappearing and blocking the electrode/electrolyte interface. To purify the electrolytic solution on the sensor array between experiments, half of the 2mL solution (the maximum capacity of the well) in the well is removed, then the remaining solution is thoroughly diluted by adding an additional 1 mL of PBS solution into the well, and then 1 mL is removed from the well for either another dilution injection or an electrochemical experiment. This process is repeated multiple times to dilute the previous electroactive molecule to a non-detectable concentration. To obtain a baseline recording of the MEA, a recording with only 1mL of PBS solution on the electrochemical sensor is taken to ensure functionality of the array. Then a control experiment is performed by injecting 1 mL of PBS into the well. The control experiment is performed (data not shown) to ensure that the signals recorded from the later injected redox molecules are not a result from a contamination in the PBS or changing influence of the reference electrode's interface with the increasing electrolytic solution volume. When injecting into the well, for all experiments, the pipette is pointed into the corner of the well to avoid directly injecting onto the electrodes. This prevents signal saturation throughout the array immediately after injection, allowing the imaging of redox molecules diffusing across the sensor array. Following the control experiment, we record the injection of 1mL of an 800 μM dopamine solution into the well (data not shown), and then an injection of 8 mM dopamine solution after cleaning out the well from the

68

800 µM dopamine experiment. For these recordings, amperometry is the electrochemical technique used to detect the presence of dopamine throughout the array. The electrode is held at a potential of 920 mV, enabling the oxidation of the dopamine molecules. The H_2O_2 experiment follows the same procedure outlined for the dopamine experiments, with the exclusion of an 800 µM injection. As such, only an 8 mM H_2O_2 injection experiment is performed for electrochemical imaging.

4.4   Results and Discussion
4.4.1   Noise Characteristic and Performance

For the noise characterization of the ADCs in the data acquisition system, the filters setup on the custom-designed PCB are 4th order low-pass filters with a cutoff frequency of 1 MHz. The noise is characterized at a 1.3 MHz sampling rate, the minimum rate required to operate the CMOS imaging sensor at a frame rate of 40 kHz. With the battery-powered voltage input, the recorded noise spectral density (NSD) is presented in Fig. 4.4. The filtered noise in the measured density starting at 20 kHz is an improvement over a previous acquisition system that was suitable for electrochemical imaging using a similar CMOS imaging sensor at a frame rate of 10 kHz with a noise density of $1.01 \times 10^{-12}\ V^2/Hz$ [51].

4.4.2   Fast Frame Rate Electrochemical Imaging

To demonstrate the parallel recording capability of the presented electrochemical sensor array, this section presents the diffusion of both dopamine and hydrogen peroxide on the CMOS device.
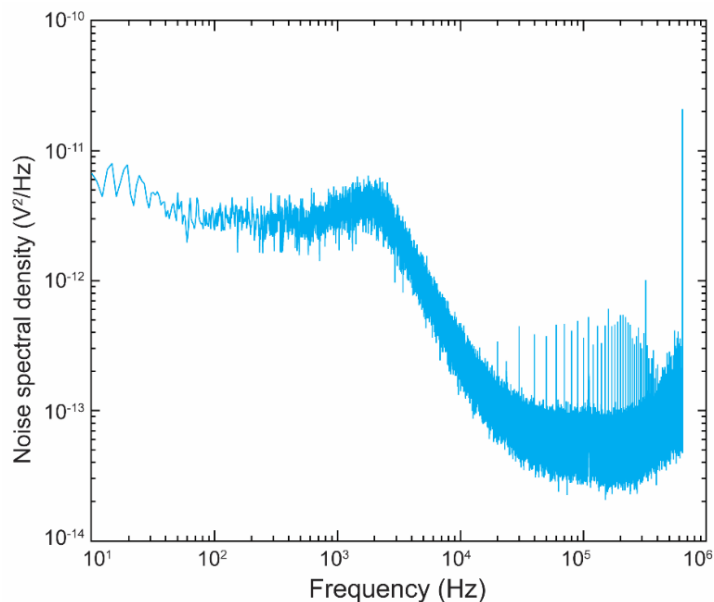
Figure 4.4: A plot of the noise spectral density versus frequency.

Dynamic Dopamine Imaging: The dopamine diffusion through the PBS solution and across the sensor array can be observed in Fig. 4.5 where the sensor array's data is presented over a 160 millisecond period. In the presented figure, the levels have been normalized and are represented by the yellow to black gradient, with yellow denoting the largest recorded current levels, which directly relates to the amount of dopamine detected by the sensor until it reaches an oxidation steady-state. Here the dopamine traverses from the right side to the left side of the sensor array and is presented in 9 frames at 20 millisecond intervals. Beyond the time presented in Fig. 4.5, the dopamine continues to diffuse across the entire array until roughly all of the sensors report the same approximate steady-state levels of oxidation current. Due to the temporal resolution of the device, it is capable of capturing events that last at least $1/10^{th}$ of a millisecond, providing the opportunity to observe electrochemical events with very limited lifetimes. In the figure in the top right corner, it is possible to observe that a sensor is broken and does not register the dopamine as
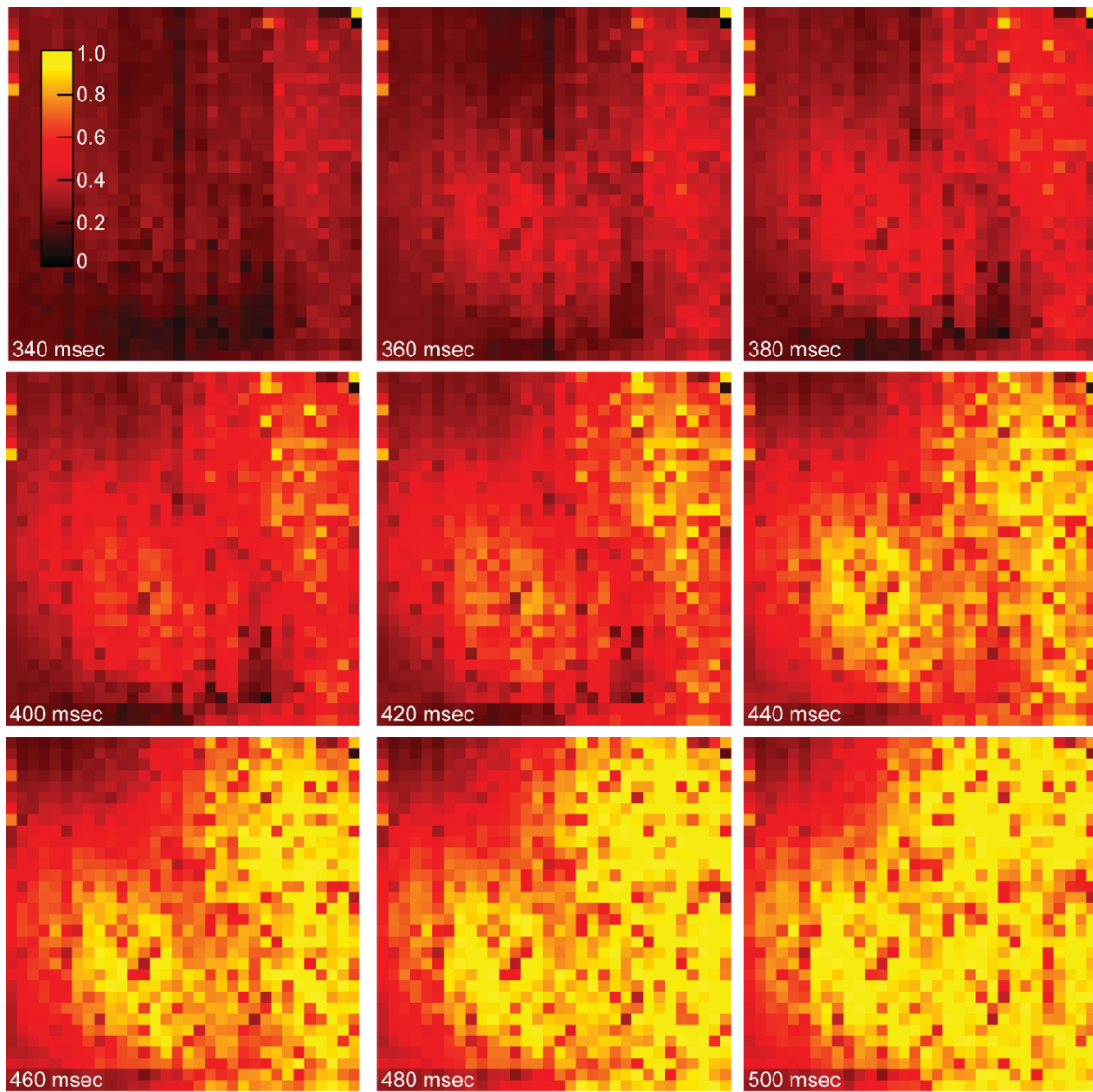
Figure 4.5: Dopamine diffusion imaging across the sensor array.

it diffuses across the array as will be seen in the same area for the hydrogen peroxide diffusion results.

Dynamic Hydrogen Peroxide Imaging: The diffusion of H_2O_2, at a concentration of 8mM, across the sensor array is presented in Fig. 4.6. In the presented diffusion imaging, the H2O2 diffuses across the sensor array starting from the left. The levels have been normalized and are

represented by the purple to blue gradient, with purple denoting the largest recorded current levels, which directly relates to the amount of peroxide detected by the sensor until its steady-state point is reached. The diffusion of the H_2O_2 is displayed in 150 millisecond intervals. From the dopamine and peroxide imaging results, we see that the sensor array is capable of providing spatiotemporal data that can be used to visualize the diffusion of an electroactive molecule across the array.
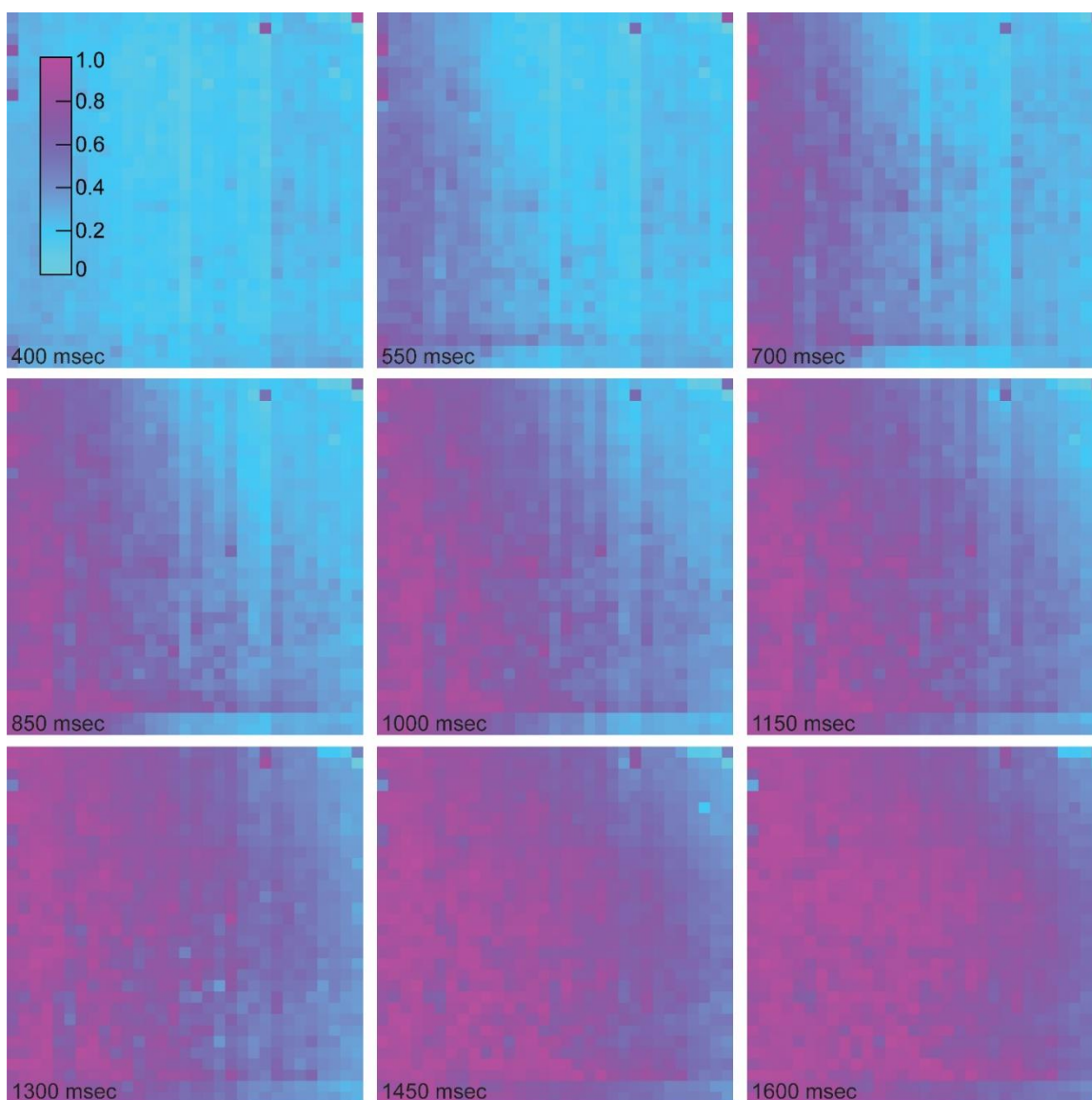
Figure 4.6: H2O2 diffusion imaging across the electrochemical sensor array.

4.5 Conclusion

In this chapter, we present an electrochemical imaging platform, which consists of an electrochemical sensor and FPGA-based data acquisition system, capable of recording a 32×32 pixel array of sensors at 40,000 frames per second, one of the fastest reported to date. The presented electrochemical detector, an integration-capacitor-based TIA with an integrated electrode, is used throughout a 32×32 array to enable large-scale electrochemical recordings. To prepare the device for electrochemical experiments, post-CMOS processing is used to integrate a platinum MEA onto the CMOS chip and the device is prepared for single-cell applications by the integration of 15 μm $\times$ 15 μm SU-8 wells. To enable the fast 40 kHz frame rate, an FPGA-based data acquisition system is designed to operate the electrochemical sensor and digitize the 32 parallel outputs of the CMOS chip. The device is used to successfully image the diffusion of dopamine and hydrogen peroxide over the 32×32 pixel array of sensors at a frame rate of 40,000 frames per second. The presented system provides significant benefits for studies that require high-throughput and high spatiotemporal resolution, such as high-throughput single-cell amperometry to study vesicle secretion, mechanisms of neurological diseases, and the dynamics of neurotransmitter release.

CHAPTER 5: SINGLE-CELL RECORDING FROM HUMAN NEUROBLASTOMA CELLS USING 1024-CH CMOS BIOELECTRONICS

5.1 Chapter Notes

In this chapter, we report the measurement and characterization of neurotransmitter secretion from human neuroblastoma cells (SH-SY5Y) using the 1024 channel CMOS neurochemical microelectrode array. Human neuroblastoma cells, SH-SY5Y, are often used as a neuronal model to study Parkinson's disease and dopamine release in the substantia nigra, a midbrain region that plays an important role in motor control. Secretions from 76 cells are simultaneously recorded by loading the CMOS device with SH-SY5Y cells. In the presented 42-second measurement, a total of 7147 single vesicle release events are monitored. The study shows the CMOS device's capability of recording vesicle secretion at a single-cell level, with 1024 parallel channels, to provide detailed information on the dynamics of dopamine release at a single-vesicle resolution. The work described in this chapter was completed with Geoffrey Mulberry, Jonhoi Smith, Manfred Lindau, Bradley A. Minch, Kiminobu Sugaya, and Brian N. Kim [*].

5.2 Introduction

Neurotransmitter release is modulated by molecular manipulations related to neurological diseases [1] and drug treatments [2]. For example, Parkinson's disease can considerably reduce the quantity of dopamine release [3] while the drug L-Dopa can increase the amount of secretion [2]. The release of neurotransmitters occurs in quantal packets when vesicles fuse with the cell membrane. By studying the secretion from individual vesicles, we gain rich information regarding

---

[*] In this chapter, we use material published in IEEE Transactions on Biomedical Circuits and Systems 2018, [24]

the dynamics of membrane fusion [4], obtain insight into the mechanisms of neurological diseases at the molecular level [5], and learn both the desirable and undesirable side effects of drug treatments [6], [7]. Neurosecretory vesicles are small, commonly less than 100 nm in diameter. Release from such a vesicle is a fast process which occurs on a time scale of milliseconds or less and is thus difficult to observe using microscopy. Thus, an electrochemical method (amperometry) is widely used to monitor neurotransmitter release with high temporal resolution by oxidizing neurotransmitters at an electrode [4]. Oxidation is the process of molecules, such as the neurotransmitters dopamine, epinephrine, norepinephrine, and serotonin, releasing electrons into the electrode, generating picoampere currents that can be measured with high-quality low-noise amplifiers. Cyclic voltammetry is also an electrochemical method which is capable of measuring neurotransmitter levels but suffers from a lower temporal resolution compared to amperometry and is adequate for detecting the neurotransmitter level in a slow dynamic system. However, amperometric measurements conducted at the single-cell level and single-vesicle level are traditionally a low-throughput method where each cell is measured individually with a microelectrode under microscopic observation, which makes the technology costly and time-consuming to acquire sufficient data to derive statistically significant conclusions.

The limitations of single-cell amperometry can be overcome by using a scalable CMOS device in which the electrodes are each directly integrated with a dedicated amplifier. Several CMOS-based monolithic biosensors have been proposed using this concept of monolithic integration [34]–[39] to perform various types of electrophysiology with enhanced spatiotemporal resolution. A device that was proposed for the application of DNA sequencing integrated a solid-state nanopore onto a CMOS chip and achieved enhanced temporal resolution as well as low noise

performance with a sampling rate of up to 20 MHz [35], [70]. For the purpose of measuring action potentials from a neuron with a high spatiotemporal resolution, a multifunctional CMOS chip with an array of 59,760 on-chip electrodes can provide a high channel count of up to 2048 electrodes for simultaneous recording [36], [42]. The multifunctional CMOS chip featured 28 amplifiers for neurotransmitter detection using cyclic voltammetry with the 100s of pA_{RMS} noise level. Using an array of 11,011 electrodes, action potentials from axons in a neuronal network were measured with high spatiotemporal resolution [37], [43]. Impedance spectroscopy with a high spatial resolution and low-noise was performed with an array of 59,760 electrodes integrated onto a multifunctional CMOS chip [44]. To study bursting events from neurons in a neuronal network, a device providing high spatial resolution with an array of 4096 electrodes was proposed [45]. Another proposed system contains 1024 pixels to provide a low-noise multifunctional CMOS device with enhanced spatiotemporal resolution for extracellular potential measurement, optical cell detection, current stimulation, and cellular impedance measuring [39]. A low-noise device with an integrated on-chip electrode array was developed for the purpose of parallel recording of neurotransmitter release with a channel count of 100, providing high-throughput amperometric measurements [34]. This monolithic integration of an on-chip electrode array onto a CMOS device has demonstrated the feasibility of recording neurotransmitter release with high-throughput and a fine spatiotemporal resolution [34]. However, the fabricated array did not provide any provision for isolating the electrodes, thus allowing multiple cells to sit atop an electrode, and secretions from adjacent cells can influence readings from the electrode of interest. To address this issue, microwells as described by [27] were incorporated into a 100-electrode amperometry chip [64]. In this chapter, we will present a monolithically integrated CMOS-based electrochemical sensor array with 1024

Figure 5.1: Schematic view of the half-shared OPA and TIA designs. One half-OPA is shared among four TIAs. In a TIA, the current induced by the oxidation of neurotransmitters (I_{elecN}) is added to an offset current (I_{offset}). The currents are integrated on an integration capacitor (C_{intN}) and read out periodically (V_{outN}). 2018 © IEEE

electrode-amplifier pairs operating at a frame rate of 10,000 per second, one of the fastest reported to date. Through the use of SU-8 in post-CMOS processing, structures are created to permit only a single-cell to rest on an electrode. Thus, the monolithic device is able to record neurotransmitter release throughout the array at a single-cell level and permit the resolution of single vesicle release events. The ability to offer a high density of single-cell measurements in a matter of minutes with the presented device offers significant benefit in regard to the study of the dynamics of neurotransmitters and the underlying mechanisms of vesicle secretion. To demonstrate the capabilities of this device, we recorded vesicle secretion from SH-SY5Y cells, a type of neuroblastoma cell that is used as an in vitro model for dopaminergic neurons. SH-SY5Y cells are often chosen for Parkinson's disease studies because of their human origin and similar catecholaminergic neuronal properties to dopaminergic neurons of the midbrain [81], [82].

In Section 5.3, we discuss the design and characterization of CMOS devices with 1024 transimpedance amplifiers (TIAs). In Section 5.4, we describe post-CMOS processing for

integrating an on-chip electrode array. In Section 5.5, we discuss on-chip recordings of SH-SY5Y's dopamine releases using the monolithic CMOS device. In Section 5.6, we analyze the measurements of neurotransmitter release.

5.3   Design of 1024-ch Transimpedance Amplifier Array

In this section, we describe the design of our CMOS device comprising a 1024-ch TIA array integrated with an on-chip array of 1024 electrodes. The resulting high-density electrode array is capable of measuring picoampere currents.

5.3.1   Half-Shared Operational Amplifier Design

Designing a small-sized TIA is a requirement to enable the integration of an array of 1024 amplifiers into a single silicon die. To use the silicon area most effectively, we adapted the half-shared operational amplifier (OPA) design of [49]. In this design, the non-inverting input is shared by several inverting inputs. The half-shared design achieves a significant reduction of cell area by almost a factor of two and reduces the power consumption by nearly half. The disadvantage of the half-shared design is the lack of individual control of the non-inverting input voltages. However, in many high-throughput applications including amperometry, individual control of the non-inverting inputs is not necessary [34], thus making the half-shared design advantageous. The half-shared design and TIA design is depicted in Fig. 5.1. The OPA uses a simple five-transistor design to minimize the area and power consumption. The current mirror, formed by M2 and M4N, closely matches the current level in all branches of sharing OPAs. The non-inverting input transistor, M1, is in the half-OPA and the inverting input transistor, M3N, is in the individual TIA. Negative feedback through M6N regulates the voltage at electrode$N$ to be the same as the non-inverting

input voltage (V_{ref}). The TIA uses a two-stage amplifier, thus the phase margin needs to be considered. The open-loop configuration without feedback is studied with M3N gate as the input and M6N source as the output. Two poles are from the M3N drain and M6N source. The dominant pole is introduced from the capacitance at the electrode and the 2nd pole can be close to the dominant pole because M3N is operating in moderate to weak inversion. Thus, a compensation capacitor (C_{compN}), a 20-fF polysilicon-insulator-polysilicon (PiP) capacitor, is used to increase the phase margin of the TIA by producing a zero (g_{m3N}/C_{compN}) which closely matches the frequency of 2nd pole from M3N. The current from the electrode (I_{elecN}) is integrated onto the integration capacitor (C_{intN}), which causes the voltage of C_{intN} to drop (ΔV). This voltage drop is readout periodically with a cycle interval (Δt) from each TIA. The cycle interval is determined by the desired sampling rate. For example, if a cycle interval of 100 µs is used, the resulting sampling rate of the TIA is 10 kS/s. During the readout, C_{intN} is reset through M7N transistor to re-initiate the next cycle of integration. The dimensions of each transistor in the TIA design are listed in Table 5-1. C_{intN} represents the total capacitance at the integrating node, including a passive PiP capacitor component and parasitic capacitors added by nearby transistors (M6N and M7N). The TIA includes two interchangeable C_{intN}s, whose estimated capacitances are 116 fF and 13 fF. The transimpedance gain of the TIA is determined by Δt and C_{intN}. The measured transimpedance gain of every 1024 amplifiers is 0.86 ± 0.03 mV/pA (standard deviation, SD) and 7.72 ± 0.99 (SD) mV/pA, for 116 fF and 13 fF, respectively. A larger deviation in gain is observed when using the 13-fF C_{intN} compared to using the 116-fF C_{intN}. This is because the small C_{intN} is largely made of parasitic capacitance at the integration node which is inconsistent across the array. The integrating capacitor is incapable of integrating negative current, thus only offering unipolar measurements.

To enable bipolar measurements, an offset current (I_{offset}) is applied in the TIA using M5N. I_{offset} is superimposed on I_{elecN} to generate I_{intN}, and when the electrode current drops below zero, I_{intN} reduces below I_{offset}. I_{elecN} can drop as low as -I_{offset} and still sustain a positive current through M6N. If I_{elecN} falls below -I_{offset}, the negative feedback will be disabled, effectively turning off the TIA. Thus, the TIA is capable of bipolar measurement with a dynamic range of -I_{offset} to + ($C_{intN}\times(V_{DD}-V_{ref})/\Delta t$) – I_{offset}. The TIA's dynamic range is -500 pA – 2516 pA with C_{intN}s of 116 fF, Δt of 100 µs, I_{offset} of 500 pA, and V_{ref} of 0.7 V.

5.3.2   Bandwidth and Noise Characteristics

The TIA is characterized by injecting known AC and DC currents into the electrode node. The TIA's frequency response is measured by applying sinusoidal voltage (AC amplitude: 200 µV – 2 mV) through a 1-MΩ resistor into the amplifier, for a range of frequencies extending beyond the Nyquist frequency. This input generates a sinusoidal current of 200 pA – 2 nA that can be measured using the TIA. We chose a 1-MΩ resistor because of a possible zero interfering with the frequency-response measurement. An introduction of the zero by the input resistor (and its parallel parasitic capacitor) in the low-frequency range can cause a larger input current which results in a misinterpretation of the frequency response. With an approximate parasitic capacitance of 500-fF across the resistor, the zero of the input resistor and the parasitic capacitor is expected to be at 318 kHz, which is beyond the frequencies of interest. As expected, the frequency response of the TIA, as a result of periodic sampling of the integration capacitor, has the characteristics of the sinc function (Fig. 5.2). When examining the characteristics of the TIA in the frequency domain, two bias conditions are tested: I_{bias} of 517 nA and 55.2 nA. The dominant pole of a sinc filter at a
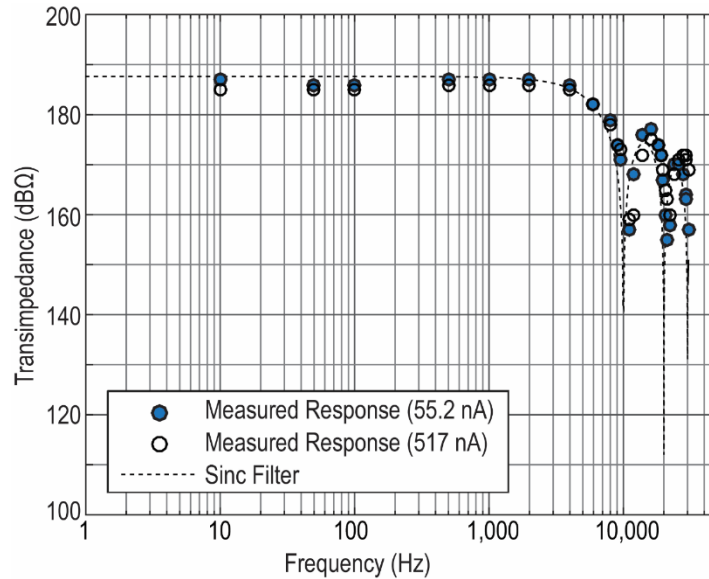
Figure 5.2: The frequency response of the half-OPA-based TIA. 2018 © IEEE

sampling rate of 10 kS/s is expected to be ~ 4.4 kHz, thus the influence of the biasing level is

limited while the sinc's dominant pole is lower than the bandwidth of the OPA. The frequency

response follows the characteristic of a sinc filter with a -3 dB point of ~4.4 kHz. The frequency

response beyond the -3 dB point still influences the sampling bandwidth, thus aliasing, however,

the frequency response sharply drops with the sinc filter. Peaks of side lobes follow an

approximately -20 dB/dec slope up until 5th sidelobe, which is equivalent to a single-pole anti-

aliasing filter. Because the sinc filter has nulls at every integer of the sampling frequency (10 kS/s),

the aliasing noise is smaller compared to a single-pole anti-aliasing filter. When the electrolytic

solution is placed on the electrode, the double-layer capacitance, which can be in the order of tens

of pF, is likely to influence the performance of the TIA. With an electrolytic solution covering the

array, an average noise of 6.16 pA$_{RMS}$ is measured with the corner frequency of the capacitive

noise ranging from 60 to 200 Hz. The test conditions are a bias level of 55.2 nA and an I$_{offset}$ of

100 pA. The presented bandwidth measurement (Fig. 5.2) is performed by using a bus that runs

across the entire array, ExConE. When ExConE is connected to the TIA, 25.81 pF of input capacitance is measured at the electrode node. This capacitance is only present to the electrode node during the bandwidth measurement and is removed by an internal switch controlled by embedded SRAMs (explained in Section 5.3.3). Therefore, the bandwidth in the presence of the electrode-electrolyte interface is expected to be comparable to the measured bandwidth.

Because of the integrating capacitor's intrinsic characteristic, noise introduced from aliasing is minimal. This built-in low-pass filter eliminates the need for an anti-aliasing filter in the readout circuitry, resulting in a smaller design area. Under these test conditions, each TIA consumes 182 nW to maintain the full bandwidth and performance. Overall, the average noise level of all 1024 amplifiers is 421.4 ± 1.1 (SD) fA$_{RMS}$ at 10 kS/s using the 13-fF C$_{intN}$. Because shot noise is expected to be 400 fA$_{RMS}$ with the 100 pA DC current, the contribution of the amplifier can be calculated to 132.6 fA$_{RMS}$. For I$_{offset}$ levels of 500 pA and 1000 pA, the measured noise levels are 1.496 ± 0.012 (SD) pA$_{RMS}$ and 1.769 ± 0.028 (SD) pA$_{RMS}$. The noise levels of the TIAs are measured at the 55.2-nA bias level. One selected TIA exhibits noise levels of 415 fA$_{RMS}$, 622 fA$_{RMS}$, and 1083 fA$_{RMS}$, at sampling rates of 10 kS/s, 20 kS/s, and 30 kS/s, respectively at the 55.2-nA bias level with I$_{offset}$ set at 100 pA (Fig. 5.3a). Compared to a high-quality electrophysiology amplifier, the Axopatch 200B with a resistor-feedback headstage and 10 mV/pA gain with a 100 pA input current, the measured noise spectral density of the TIA demonstrates comparable noise performance ($\sim 4 \times 10^{-5}$ pA^2/Hz) (Fig. 5.3). The noise simulation based on the technology-specific parameters are also presented (Fig. 5.3c). Because the noise analysis on a non-stationary circuit is impractical, a load resistor is added into the integrating node V$_{outN}$ in Fig. 5.1 to produce a stationary circuit. The simulated noise is then multiplied to a sinc function to emulate
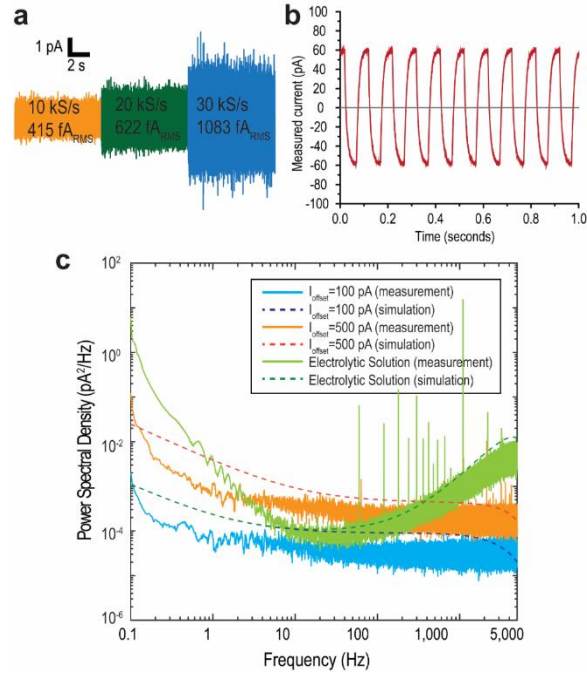
Figure 5.3: Performance of the TIA array. (a) The noise levels of the amplifier at 3 different sample rates. (b) Bipolar current measurement using the TIA. (c) The noise spectral density of the amplifier when I_{offset} is set to 100pA, 500pA, and when an electrolytic solution covers the array. 2018 © IEEE

the filtering effect from the integrating capacitor. For the electrolytic solution simulation, we added

a 25-pF input capacitor to represent the electrode-electrolytic interface capacitance. The flicker

noise matches closely between the measurement and the simulation result. Typically, the flicker

noise corner can be below 10 Hz when the input current level is deep in weak inversion [83], which

agrees with the measured noise spectral density. However, a mismatch in noise level is observed.

This may be due to the poor matching of the design parameters in the deep weak-inversion.

Designing the TIA with small-sized transistors can result in large mismatches between identical

TIAs. This is due to the manufacturing imperfection that mainly influences effective width (W)

and length (L) of fabricated transistors [84]. The OPA determines the bandwidth and V_{elecN}, and

thus transistors in the OPA need large W and L to minimize mismatch. By adapting the half-shared

OPA, investment in a large area for W and L is achievable as the inverting-half of an OPA requires only two transistors, M3N and M4N. The size selected for M3N and M4N is 10 µm × 10 µm (Table 5-1). The input-referred output is measured throughout the array, resulting in a measured variation of 1.26 mV$_{RMS}$. I$_{offset}$ is also subject to mismatch due to process variation. However, the mismatch in I$_{offset}$ across the array only affects the dynamic range by several pA which has negligible effect during the electrochemical recordings.

Table 5-1: Dimensions of transistors in the TIA design 2018 © IEEE

	M1	M2	M3N	M4N	M5N	M6N	M7N
Width	10 µm	10 µm	10 µm	10 µm	5 µm	1.2 µm	0.8 µm
Length	10 µm	10 µm	10 µm	10 µm	5 µm	1.2 µm	0.4 µm

The crosstalk between the sharing OPAs has been considered. As discussed by a previous publication [49], the response of each inverting-half of OPA is only a function of transconductance (M3N) and output impedance (M4N). Thus, as long as the sharing node (M3N_{source}) is kept constant with a constant non-inverting input, the crosstalk should be minimal. To confirm this, a 100 Hz current with 400 pA pk-to-pk is injected into an OPA while recordings are taken from three OPAs which share the inverting-half. The power loss between the original injected current and crosstalk measured from sharing OPAs is quantified. A heavy attenuation of -38.7 dB ± 3.4 dB (standard deviation) is observed. The small crosstalk may be due to the limitation of the recording setup rather than actual crosstalk through the sharing structure. The 100 Hz current is injected through a bus which runs across the entire array, which is only enabled during the electrical testing.

5.3.3   Integration of 1024-ch Amplifier Array

Fig. 5.4 shows a CMOS device containing an array of 32 × 32 amplifiers and electrodes fabricated in a standard 0.35-µm 4-metal 2-poly CMOS process. In the presented design, four TIAs
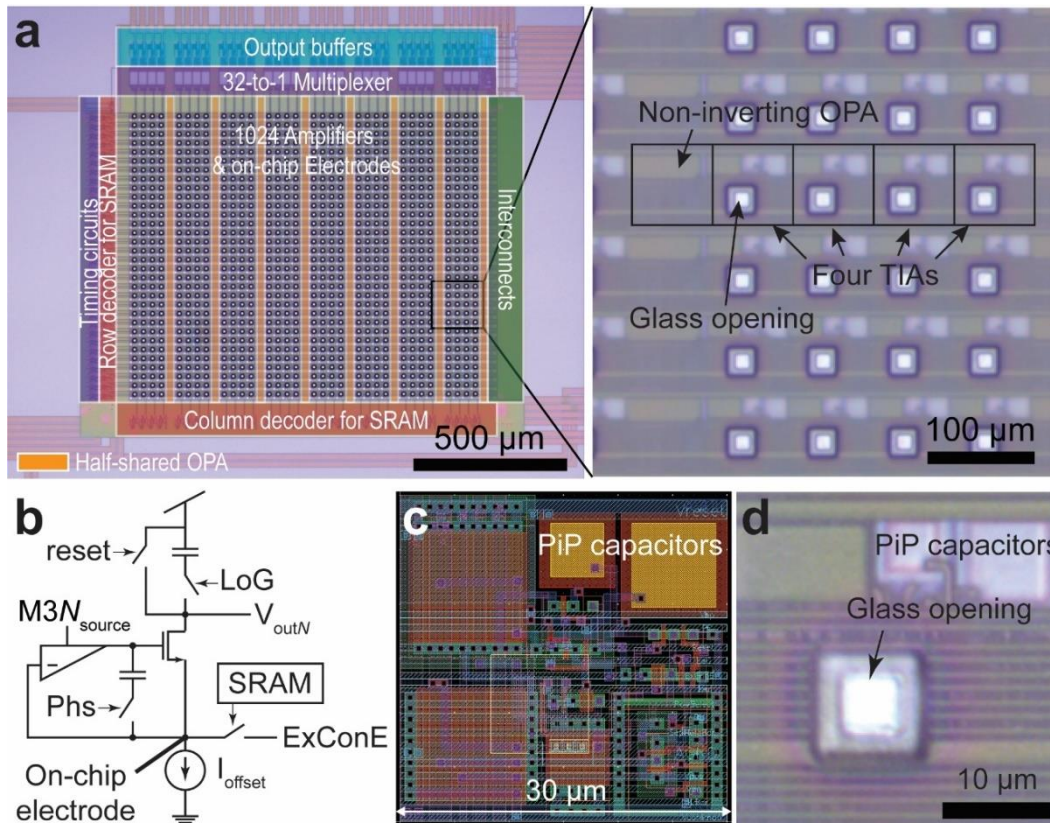
Figure 5.4: Photographs and architecture of the CMOS die and amplifier array. (a) The array has 1024 amplifiers and 1024 on-chip electrodes. The 32-to-1 multiplexer combines outputs by time-division multiplexing to condense the data. Row and column decoders allow for fully-addressable writing of embedded SRAMs in the array. (b) Each TIA has low-gain (using LoG), phase margin (using Phs) options. Also, SRAM can be programmed to connect the ExConE node to the electrode node for testing. (c) The layout of one TIA is 30 µm × 30 µm. (d) The microphotograph of the TIA is showing PiP capacitors and glass opening. 2018 © IEEE

share one non-inverting-half OPA. Each TIA occupies a $30 \times 30 \ \mu m^2$ area and includes a 1-bit SRAM. Thus, the array has a total of 1024 1-bit SRAMs. Using the column and row decoders, the embedded SRAM in each TIA is fully-addressable providing the capability to reconfigure the amplifier for unity gain, and/or enable testing circuitry. Also, global switches can be used to change the transimpedance gain and enable/disable the phase compensation capacitor.

To operate the array, two clock signals are applied to the timing circuitry and clock signals are generated to achieve time-division multiplexing, correlated double sampling (CDS), and

resetting of the integration capacitors (Fig. 5.5). The generated clocks provide the means of condensing the output of the array of 1024 sensors to 32 parallel outputs, one output per column, output(M), through time-division multiplexing. Time-division multiplexing will sequentially stagger the integration period of each row, reading out the integrated current of one TIA, ΔV_N, while the other amplifiers in the column continue to integrate their respective inputs, as previously described [34]. The array with all the peripheral circuits is compacted and only occupied ~ 1.5 mm × 1.5 mm. In this 5 mm × 5 mm silicon chip, there are also electrostatic discharge (ESD) circuits and unused testing circuits which are not visualized in the microphotograph in Fig. 5.4.

Because the CMOS chip relies on external ADCs for digitization, source-follower-based output buffers are designed to drive the capacitive load from the output line, pad, and ADC input capacitance. The overall power consumption of the chip is 12.5 mW.
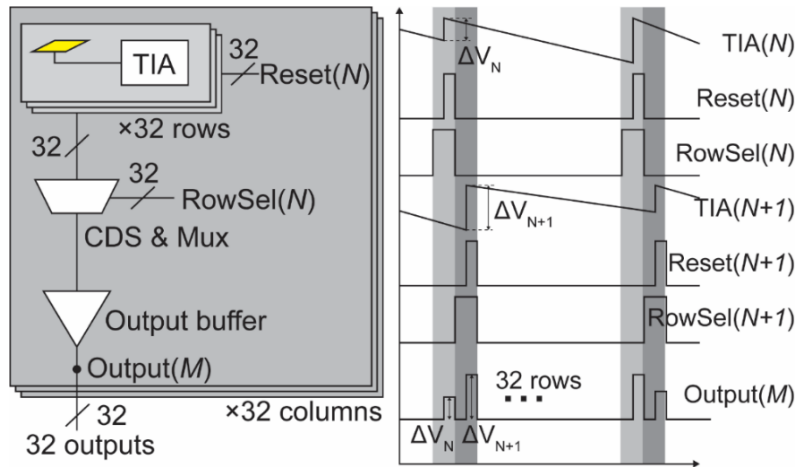
Figure 5.5: The block diagram of time-division multiplexing and timing diagram. Each gold electrode (yellow box) is connected to its respective TIA which is physically embedded directly underneath. Each row of TIA has a dedicated reset, Reset(N). The integrated voltage, ΔV_N, is generated from each TIA after each reset. Each Reset(N) is synchronized with RowSel(N) which samples the TIA output before and after each reset, thus enabling correlated double sampling. The integration periods of each TIA in every row are staggered in time to allow the time-division multiplexing without deadtime in integration. After multiplexing, output(M) includes ΔV_N of all the rows. 2018 © IEEE

86

5.4   Post-CMOS Processing

CMOS chips fabricated from foundries commonly have aluminum-copper (Al/Cu) for the top metal layer. The aluminum is highly reactive with electrolytic solutions, making the unprocessed devices intrinsically inadequate for biosensing. This reactive material not only causes large offsets in electrochemical recordings, thus introducing a high level of shot noise, but the chip can also be damaged due to water leakage. To resolve this issue, post-CMOS processing can be used to integrate polarizable electrode materials, such as gold or platinum, on top of the topmost metal layer. These materials have low reactivity, making them suitable for biological recording. \

5.4.1   On-chip Gold Electrode Array

The CMOS dies are first processed using photolithography to integrate the gold electrode array onto the surface of the chip through a lift-off process. Each die (5 mm $\times$ 5 mm) is initially attached to a coverslip (25 mm $\times$ 25 mm) to reduce the complications of handling the small CMOS chips through the standard cleanroom process. Before the chips are spin coated with photoresist, they are cleaned using acetone, isopropanol, and deionized (DI) water. A negative photoresist, NR9-1500PY, is spin coated onto the surface of the chip, exposed, and developed to create the patterns for the electrodes, leaving a sacrificial layer of photoresist on the surface where metal deposition is undesirable. The electrodes are created by first depositing 15 nm of titanium and then 150 nm of gold on the surface of the chips through sputtering (AJA Six-Gun Sputtering System, AJA International Inc., N Scituate, MA). The purpose of the deposited titanium is to provide adhesion between the Al/Cu layer on the surface of the chip and the deposited gold. To remove
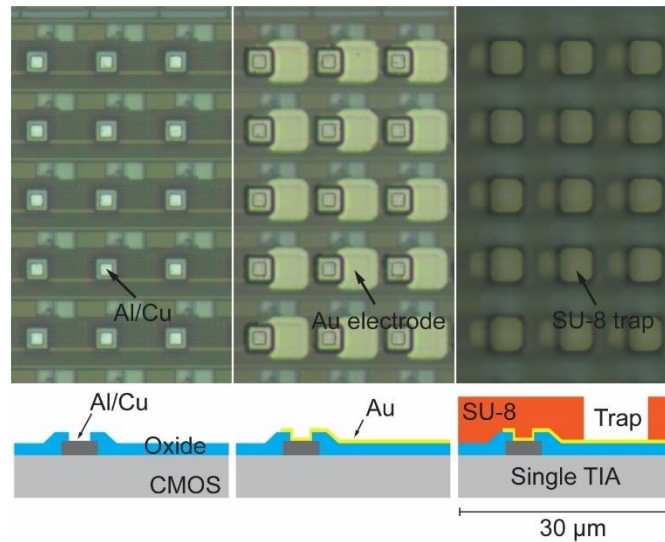
Figure 5.6: Post-CMOS processing for on-chip integration of electrodes and SU-8 wells. Initially, the CMOS die has Al/Cu as the top metal. Gold layer is patterned using lift-off process which is followed by the fabrication of SU-8 wells. The SU-8 wells are used to trap single cells. 2018 © IEEE

the sacrificial layer of photoresist, lift-off is performed by rinsing the chip with acetone. After removal of the sacrificial layer, the electrodes are patterned as intended (Fig. 5.6).

5.4.2 SU-8 Traps for Single-Cell Analysis

After lift-off has been completed, the chips are cleaned again using acetone, isopropanol, and DI water. With the array of gold electrodes integrated onto the surface of the chip, further photolithography processing is performed using SU-8 3010, a biocompatible epoxy-based photoresist. The SU-8 photoresist is used to provide isolation between each electrode in the array and to create well structures that can trap a single cell on top of an electrode [27], [64], as shown in Fig. 5.6. The estimated thickness of SU-8 traps is $20 - 30$ µm. To achieve true single-cell measurements, the SU-8 is necessary to not only prevent multiple cells from populating a single electrode, but to also prevent the influence of adjacent cells and electrodes.

5.4.3 Packaging

After the array of electrodes and SU-8 traps are integrated onto the surface of a chip, it is bonded to a PCB die holder using a silver-filled epoxy (Fig. 5.7a). Once the epoxy has cured, the chip is wire-bonded to provide an interface to the inputs and outputs of the circuitry on the chip. To protect the easily broken wire bonds when handling the PCB and from liquids during experiments, a plastic well is manufactured to cover and protect the bonds and pads exposed on the chip. The well is designed to accommodate 2 mL of liquid, 3D-printed using ABS plastic, and coated with a layer of polydimethylsiloxane (PDMS) for waterproofing and biocompatibility. The coated well is bonded to the custom PCB and the surface of the CMOS chip using additional PDMS. As shown in Fig. 5.7b, the well conceals the wire bonds, provides an opening for access to the surface of the CMOS chip, and protects external electronics from liquids used during experiments. To prepare the CMOS chip for SH-SY5Y cell measurements, the packaged devices is cleaned using a plasma cleaner (PDC-32G, Harrick Plasma, Ithaca, NY). This is necessary as there is a remaining thin film of SU-8 over some of the electrodes in the array after the resist is
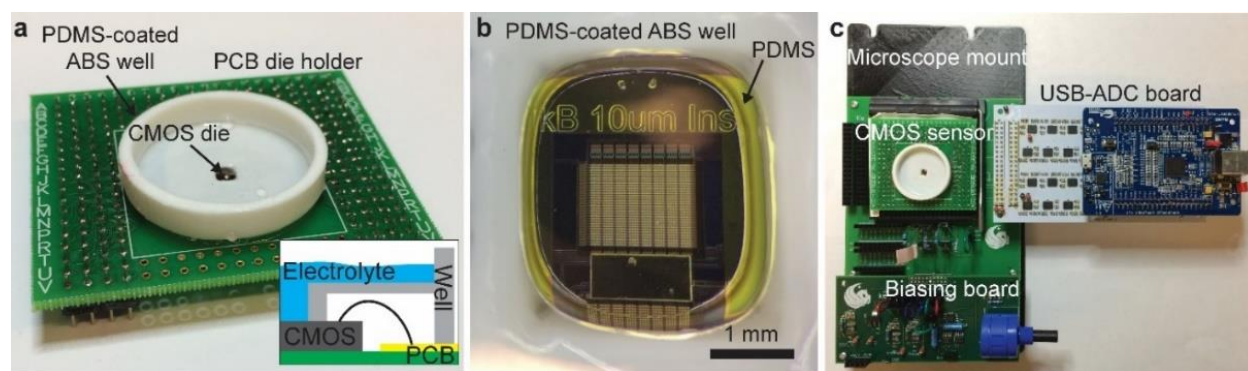
Figure 5.7: The recording setup of the CMOS chip. (a) Biocompatible packaging of the CMOS chip by using PDMS-coated 3D-printed ABS well. (b) The photograph of the electrode array opening. (c) The custom-design PCBs for biasing and data acquisition using USB 3.0. 2018 © IEEE

89

developed. After plasma cleaning, 1 mL of water is added to the surface of the chip, and the device is placed into a vacuum chamber. By vacuuming the chip with liquid on the surface, bubbles that are captured in the SU-8 traps will be eliminated. After eliminating the bubbles in the SU-8 traps, the surface of the CMOS will continue to be covered with liquid to prevent air from being captured in the SU-8 single-cell traps.

5.5   SH-SY5Y Cell Measurements
5.5.1   Recording Setup

The setup for SH-SY5Y cell recordings is shown in Fig. 5.7c. It consists of custom PCBs that hold a socket for the packaged chip, supply power and biasing to the chip, and convert and transmit analog data collected from the chip to a computer through a USB interface. The PCB die holder has pin headers to allow access to the inputs and outputs of the chip for testing and operation, as well as setting the current biasing for the TIAs in the array and the output buffers using resistors. The smaller PCB that connects to the foot of the PCB holding the socket generates the voltages needed for the chip to operate and the baseline current used for the TIAs. When operating the chip, V_{ref} is set to 0.7 V and I_{offset} is set to 500 pA.

The USB data acquisition system consists of a custom-designed PCB that has a microcontroller (Atmel SAM E70), 32 ADCs with 16-bit resolution (LTC2323-16), and a USB 3.0 controller (Cypress FX3). The Atmel chip functions as the control center for the acquisition system. All of the clocks required for the data acquisition system and the CMOS chip, are generated by this Atmel chip. The clocks generated for the CMOS chip are setup to achieve a sampling rate of 10 kHz for each amplifier and a multiplexed output rate of 320 kHz. The Atmel chip also provides the digital signals for the column and row decoders to program the SRAMs in

the array as well as the reference voltage for the amplifiers through an embedded DAC. The 32 ADCs convert the 32 parallel, time-multiplexed, signals from the CMOS chip into their binary representations at a rate of 1.3 MHz. The binary data from these ADCs are delivered directly to the USB 3.0 controller. The USB controller accumulates the data from the ADCs in its embedded memory and then transfers the data to a connected computer in packets at a rate of 106 MB/s.

5.5.2 Single-Cell Amperometry

SH-SY5Y neuroblastoma cells (ATCC# CRL-2266) are cultured in T-75 flask with 20 ml of growth media, which consists of a 1:1 ratio of MEM with L-Glutamate (Invitrogen) and F12 media (Invitrogen), 10% fetal bovine serum (FBS, Gibco) and 1% Antibiotic/antimycotic (Gibco). The cells are cultured in a 5% CO_2 incubator at 37˚C. The media is changed every 3 days. These cells mostly grow as adherent cells under these conditions. Cells are passaged when the culture becomes 80% confluent. To detach the cells, the growth media is removed, the cells washed with phosphate-buffered saline (PBS, pH7.4), and incubated with Trypsin-EDTA (Gibco, 0.25%) at 37˚C for 5 minutes, until most of the cells are detached from the flask. Trypsin is deactivated by the addition of FBS. The cells are washed twice with PBS by centrifugation at 1500 rpm for 5 minutes. The cells are then immediately used for the experiments or plated in a new T-75 flask for further expansion in the culture.

For the recording of neurotransmitter releases from SH-SY5Y cells, the 1 mL of water that is on the chip (refer to Section 5.4.3) is replaced with 1 mL of suspended SH-SY5Y cells in culture media. With the cells floating on the surface of the packaged chip, it is placed into an incubator at a temperature of 37˚ C and 5% CO_2 for one hour to provide time for the cells to be captured in the

SU-8 traps and settle onto the bottom surface. Settled cells are randomly distributed on the CMOS chip. Some cells adhere to the SU-8 surface and some cells fall into the SU-8 traps. Once the cells are trapped and adhered in the SU-8, the 1 mL of culture media is exchanged with 1 mL of recording buffer. The recording buffer contains the following concentrations at a pH level of 7.3 and an osmolality of 300 mmol/kg: 140 mM NaCl, 5 mM KCl, 1 mM $MgCl_2$, 10 mM $CaCl_2$, and 10 mM HEPES/NaOH. At this point, the chip with cells is ready for recording and is placed into the socket (Fig. 5.7c). An Ag|AgCl reference electrode connected to ground is placed in the recording buffer and then the power and clock signals are applied to the chip. To stimulate the cells, 1 mL of a high KCl stimulation buffer is added to the recording buffer. The stimulation buffer has the same pH level and osmolality of 7.3 and 300 mmol/kg, respectively, with the following concentrations: 140 mM KCl, 5 mM NaCl, 1 mM $MgCl_2$, 10 mM $CaCl_2$, and 10 mM HEPES/NaOH. The anticipated KCl concentrations after adding the stimulation buffer is 72.5 mM, which is known to cause depolarization of the cell membrane and stimulate vesicle secretions [85].

5.5.3   1024-ch Parallel Recordings of Vesicle Releases Using CMOS Chip

The diameter of a suspended SH-SY5Y cell is ~12 µm, which is marginally smaller than the 15 µm × 15 µm SU-8 single-cell traps (Fig. 5.8). Many individual SH-SY5Y cells trapped in SU-8 wells are observed (Fig. 5.8b), allowing single-cell amperometry from the respective electrodes. Multicellular clumps that are also present failed to fit into the SU-8 traps because the SU-8 trap is only large enough for a single cell (Fig. 5.8b). For this experiment, of the 1024 SU-8 traps, roughly ~10% of the electrodes in the array are covered by a single cell. The CMOS device successfully measured amperometric spikes simultaneously from 76 electrodes out of 1024
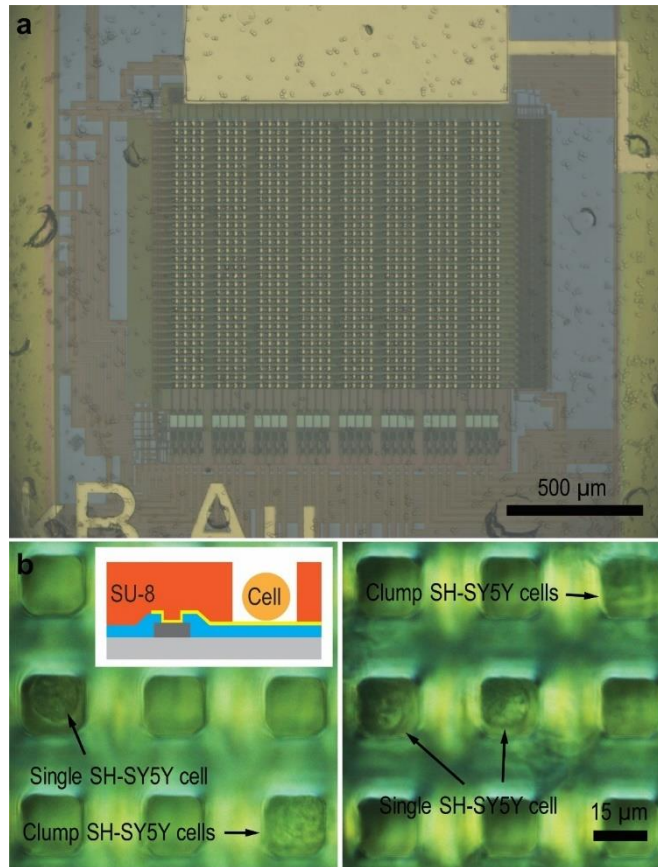
Figure 5.8: (a) Microphotograph of SH-SY5Y cells on the CMOS device. (b) Differential interference contract (DIC) image of SH-SY5Y cells on the CMOS device. Single SH-SY5Y cells are trapped in SU-8 traps. The traps allow only single cells to fall in to make contact with the electrode. The image has been processed by adjusting the contrast. 2018 © IEEE

electrodes in a single set of measurements (Fig. 5.9a). This is identified by manually monitoring the amperometric recordings from individual electrode-amplifier. Each spike corresponds to dopamine release from a single vesicle. The recorded data are read and demultiplexed using a custom-written MATLAB code. The amperometric data are then imported to Igor Pro 7 and analyzed using Quanta Analysis v8.20 [10]. In the representative measurements shown in Fig. 5.9b, vesicle secretions as small as 9.6 pA and as large as 1487 pA are observed, with an average amplitude of 132.4 pA. Within the 42 seconds of data, 333 quantal release events from this
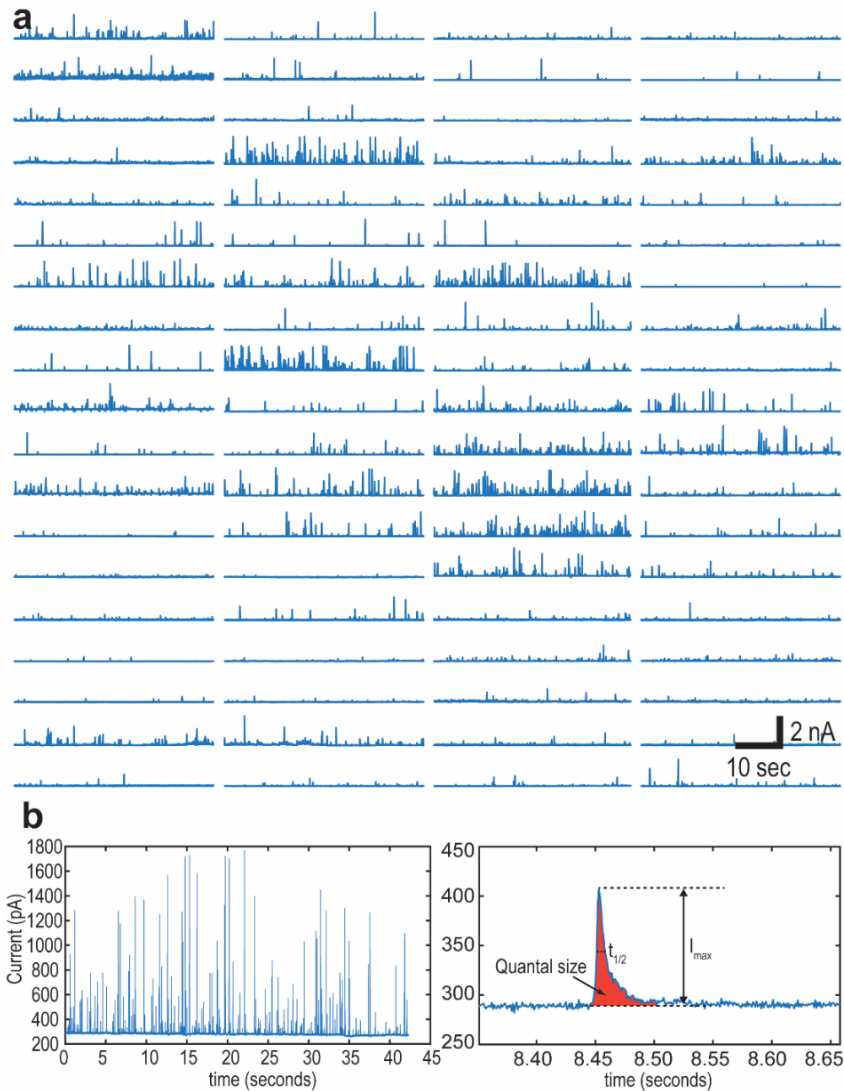
Figure 5.9: (a) Parallel recordings of 76 single-cell vesicle secretions. (b) A representative recording shows individual spikes corresponding to single vesicle release of neurotransmitters. 2018 © IEEE

particular single cell are detected. The events from this cell exhibited an average half-width of 1.26 ms. To determine the number of released neurotransmitters, the quantal size can be found by integrating the current measured from each spike. For this cell the average quantal size is 0.288 pC, corresponding to the release of ~900,000 dopamine molecules per vesicle.

5.6   Statistical Analysis of Amperometric Spikes

About 7147 vesicle secretions are detected from all 76 measurements. The characteristics of all measured spikes, including the half-width ($t_{1/2}$), maximum current (I_{max}), and amount of dopamine, are analyzed (Fig. 5.10). The average half-width is 1.63 ms with a standard deviation of 1.00 ms. With the 4.4-kHz bandwidth of the CMOS device, spikes with above 1-ms half-width can be measured reliably, however, faster spikes from rat ventral midbrain dopamine neurons, with $100 - 600$ µs half-width, may be difficult to resolve using this CMOS device [8]. This observation is consistent with measurements from other neuroblastoma cell lines [5] and neurons [86], but the half-width from SH-SY5Y cells is significantly faster than that obtained for endocrine cells, such as PC-12 and bovine chromaffin cells [7], [67], [87]. The number of events varied from zero to 419 per cell, with 94 events per cell being the average. For the 76-cell measurements, the average amount of dopamine release from a single vesicle is 1.86 attomole, corresponding to ~1.12×10^6 molecules per vesicle. The number of dopamine per vesicle in human blastoma SH-SY5Y cells is about 100 times larger than that of rat ventral midbrain neurons [8], and is about 4 times less than that of bovine chromaffin cells [17].

5.7   Conclusion

In this chapter, we present a 1024-channel monolithic CMOS bioelectronics device, enabling high-throughput recordings of vesicle secretion from SH-SY5Y cells. Each electrode in the array, 15 µm × 15 µm in size, has a dedicated TIA that has a small footprint of 30×30 µm^2 and fully addressable SRAMs to configure the sensors individually. The 1024-ch sensor array operates with a frame rate of 10,000 per second. We discussed in detail the device packaging, a
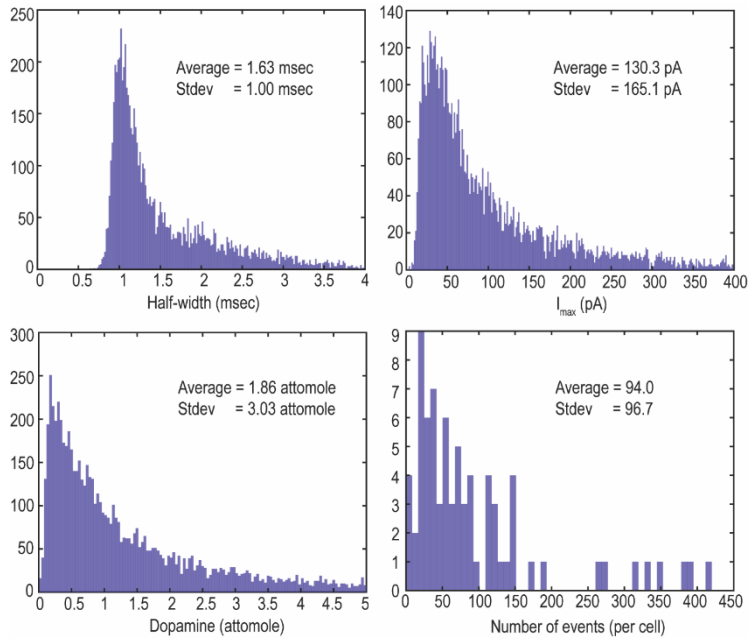
Figure 5.10: The characteristics of vesicle secretions in human neuroblastoma cells, including half-width, maximum current, the amount of dopamine released, and number of vesicle release per cell. 2018 © IEEE

completely in-house process that protects the wire bonds as well as pads, provides a reservoir to contain solutions, provides access to the electrode array on the surface of the device, and protects external electronics interfacing with the device. Monolithic integration of the gold electrodes and SU-8 single-cell traps to the surface of the CMOS bioelectronics is demonstrated to permit on-chip high-throughput single-cell amperometry. To demonstrate the feasibility of the device, SH-SY5Y cells are placed onto the sensor array to measure dopamine released from the cells after stimulation. Single-cell recordings of 76 cells and 7147 vesicle release events are captured in several minutes. This would have taken significantly longer, on the scale of months, to acquire using traditional instrumentations. The fine temporal resolution of the TIAs are able to capture the neurotransmitter secretions of the SH-SY5Y cells, which exhibited a fast half-width average of 1.63 ms. The presented system design enables the high-throughput study of vesicle secretion at the

Table 5-2: Comparison to State-of-the-Art CMOS Bioelectronics 2018 © IEEE

Reference	[8]	[12]	[13]	[15]	**This Work**
Technology Node	0.5 μm	0.18 μm	0.13 μm	0.18 μm	**0.35 μm**
Die Size	3 mm × 3 mm	5 mm × 2.65 mm	3 mm × 2 mm	12 mm × 8.9 mm	**5 mm × 5 mm**
Number of Electrodes	100	200	1024	59760	**1024**
Electrode Size	15 μm × 15 μm	10 μm × 10 μm	28 μm × 28 μm	3 μm × 7.5 μm	**15 μm × 15 μm**
Electrode Material	Platinum	CNT Coated Gold (Current channels), Gold (Voltage Channels)	Gold	Platinum	**Gold**
Current Measurement Channels	100	200	4	28[a] 32[b]	**1024**
Noise performance (Current)	~ 100 fA$_{RMS}$	480 fA$_{RMS}$ at 110 Hz filtered	56 pA$_{RMS}$	120 pA$_{RMS}$[a] 6.4 pA$_{RMS}$[b]	**415 fA$_{RMS}$**
Bandwidth (Current)	-	110 Hz - 10 kHz	700 Hz	16 kHz[b]	**4.4 kHz**
Accumulated Sample Rate (Current)	200 kS/s	200 kS/s	-	80 kS/s[a]	**10 MS/s**
Voltage Measurement Channels	-	200	4	2048	**-**
Noise performance (Voltage)	-	4.07 μV$_{RMS}$ at 100 kHz	13 μV$_{RMS}$	4.4 μV$_{RMS}$	**-**
Bandwidth (Voltage)		1 Hz - 10 kHz	-	1 Hz - 10 kHz	**-**
Accumulated Sample Rate (Voltage)	-	200 kS/s	-	640 kS/s	**-**
ADC	16-bit off-chip	10-bit on-chip	16-bit off-chip	10-bit on-chip	**16-bit off-chip**
Total Power	-	3.21 mW	-	86 mW	**12.5 mW**

Single-cell level through monolithic integration of an array of 1024 electrode-amplifier pairs with SU-8 single-cell traps, a biocompatible packaging process, and digital circuitry that enables 1024 parallel recordings at a rate of 10 kS/s/ch. The presented system design marks a significant advancement in regard to the field of single-cell electrophysiology, which is hindered by the low throughput of traditional methods. A comparison of the presented system design to recent state-of-the-art CMOS bioelectronics is presented in Table 5-2. The device is demonstrated to provide

improved benefit toward revealing the rich information regarding the dynamics of vesicle secretion and the underlying mechanisms of neurological diseases. For the study of neurological diseases and drug treatments that modulate neurotransmitter release, the presented device provides an excellent platform to obtain a significant amount of single-cell recordings to better arrive at statistically significant conclusions that must be established on the basis of a large number of measurements.

CHAPTER 6: QUANTIFYING NEUROTRANSMITTER SECRETION MODULATION USING HIGH-DENSITY CMOS NEUROCHEMICAL ELECTRODE ARRAY

6.1 Chapter Notes

In chapter 6, we apply the 1024 neurochemical microelectrode array to capture the modulation of neurotransmitter secretion to due pharmacological substances used for treating depression (desvenlafaxine) or Parkinson's disease (L-Dopa and selegiline). To the best of my knowledge, the potential modulation to neurotransmitter secretion characteristics by desvenlafaxine and selegiline have not yet been studied. Additionally, the high-throughput screening capabilities exhibited in this chapter demonstrate that the novel technology developed in this dissertation can accelerate the study of neurodegenerative disorders and new pharmacological therapies that target the dynamics of neurotransmitter secretion. The work described in this chapter was completed with Brian N. Kim[*].

6.2 Introduction

Chemical transmissions at synapses are an essential mechanism in neuronal networks, because they facilitate the propagation of information throughout the nervous system for body functions, memories, and emotions. These chemical transmissions relay information between neurons through the secretion of membrane-bound neurotransmitters, which exist in high concentrations within vesicles. Neurotransmitters are released in quantal events through a fusion pore, which are created when vesicles fuse with the plasma membrane during the exocytosis process. Quantal events are fast, typically occurring in milliseconds or less, and the quantal size is

---

[*] In this chapter, we use material published in Nature Communications, 2021 [114].

small, containing less than attomoles of neurotransmitter molecules per quantum (vesicle) [5], [8]. An electrochemical recording using amperometry can reveal rich details of individual quantal events, including the sub-millisecond dynamics of quantal secretion, quantal size (# of molecules per vesicle), frequency, as well as the kinetics of vesicle fusion [10]. In the amperometric setup an electric potential is held between two electrodes, a reference electrode and a working electrode. This setup allows electroactive molecules, such as dopamine, serotonin, epinephrine, and norepinephrine, to undergo either oxidation, the release of electrons from the molecule, or reduction, the acquisition of electrons to the molecule, and generates a current that is measurable.

Amperometric recordings using carbon fiber electrodes (CFEs) have been pivotal in studying the fundamental mechanisms of vesicle fusion [6], [8], [11], [16], [17] over many decades. Amperometry using CFEs have also been crucial for studying the molecular effects of neurological diseases and pharmacological treatments that modulate the exocytosis process [2], [18], [21]. The phenomenon of incomplete exocytosis events allowing recycling of vesicles for rapid reuse is called 'kiss-and-run' and has been studied extensively as this secretion regulation provides insights into neuronal communications and potentially the mechanisms of neuronal plasticity [11]. The study of this phenomenon is enabled by amperometry because these events require an enhanced temporal resolution to study these millisecond scale kiss-and-run events at a single vesicle scale [8], [12]–[16]. A protein that has been studied is alpha-synuclein, which has been implicated in the pathogenesis of Parkinson's disease (PD) and has been found to reduce the frequency of exocytotic events by inhibition of vesicle priming for fusion with the cellular membrane [18]. In addition to studying the vesicle-level effects of neurodegenerative diseases, amperometry is used to study or monitor biomarkers that can reveal signs of a neurological disease.

The high sensitivity and temporal resolution of amperometry has enabled *in vivo* animal study of monitoring the concentration of nitric oxide, which is linked to neuronal loss [22].

Despite the significance of the studies conducted and the discoveries made using amperometry, the CFE technique is labor-intensive [88]–[94], time-consuming [59], [91], [95], [96], and can take from weeks to several months [26] to research the effects of neurological diseases or pharmacological treatments. In these studies, it is important that amperometry is performed at the single-cell level to account for heterogeneity in the characteristics of quantal release among the cell population [10], [25]. Therefore, to compare the kinetics of quantal release and the size of vesicle secretion with statistical significance, typically more than 30 independent cell measurements are collected for both the experimental and control groups to develop meaningful conclusions. The prohibitive features of single-cell amperometry have limited the wide application of this technology to survey (or screen) the molecular effects of pharmacological modulations and neurodegenerative pathologies associated with the synaptic neurotransmitter secretion process.

To overcome the complications of traditional single-cell studies, scalable complementary metal-oxide-semiconductor (CMOS)-based biosensors are being developed with integrated on-chip electrode arrays [24], [34]. Developed CMOS-based biosensors have demonstrated their parallel recording capabilities through the mapping of the concentration of ferricyanide across a 16×16 electrode array [40], the diffusion of H_2O_2 in a 32×32 electrode array [32], and the flow injection of several analytes across a 128×128 electrode array [41]. Furthermore, these CMOS-based bioelectronic systems have been developed and used for high-throughput recordings of neurotransmitter secretion from bovine chromaffin cells with a 10×10 electrode array [26], [34]

and from human neuroblastoma cells (SH-SY5Y) using a 32×32 electrode array [24]. Using the 10×10 electrode array, the effects of the antidepressant drugs, bupropion and citalopram, on neurotransmitter secretion have been studied [26].

In this chapter, we discuss the development of a novel silicon-based electrode array, which integrates 1024 on-chip microelectrodes (Fig. 6.1a-b), and is capable of single-vesicle resolution recordings. The designed silicon-based electrode array is based on CMOS technology, which enables a large-scale integration of amplifiers and other electronic circuits. An on-chip microelectrode array is integrated directly on the surface of the designed CMOS chip using additional steps of fabrication, post-CMOS fabrication. The presented post-CMOS processing has been modified from a previous work [24] to improve the noise performance of each electrochemical sensor through the use of a silicon dioxide insulation layer that defines the effective area of the electrodes throughout the array, thus permitting the developed system to record the small amperometric signals from single vesicle secretions. With the low-noise amplifiers in the CMOS chip and the improved noise performance due to the new post-CMOS process, this work presents the first single-vesicle recordings from pheochromocytoma (PC-12) cells using monolithically integrated CMOS biosensors. The presented silicon-based bioelectronics system can capture a large pool of quantal events in the span of minutes, providing rapid results compared to the conventional amperometry technique that can take from weeks to months to amass a comparable dataset [26]. Using data collected from two experiments, the statistical analysis presented reveals the changes in the characteristics of vesicle-membrane fusion and neurotransmitter release between a control group and L-Dopa treated group of PC-12 cells. The presented device provides a platform that can be used to closely monitor any pharmaceutical

102

modifications to the synaptic transmission process by PD treatments, Alzheimer's disease treatments, alpha-synuclein deposits, depression therapies, and other therapies for neurodegenerative disorders, at the single-vesicle level.

6.3   High-density Silicon-Based Electrochemical Microelectrode Array for Quantal Analysis.

The microelectrode array is designed with each electrochemical sensor having a dedicated amplifier that permits electrochemical detection as conceptually illustrated in Fig. 6.1a. The CMOS device is fabricated using a standard 4-metal 2-poly 0.35 µm CMOS process and contains an array of 32×32 electrodes with an integrated amplifier array [24] (Fig. 6.1c). To detect the presence of neurotransmitters at an electrode, the amplifier integrates the electrons released from the electroactive molecules onto a capacitor, which results in a current-dependent voltage output, $V_{oxidation}$ (Fig. 6.1a). After the integration cycle, the output voltage is sampled and the charge across the capacitor is reset by a switch to initiate the next cycle. For efficient readout of the entire electrode array, there are 32 multiplexers (Fig. 6.1c) that handle the readout of the 32 columns of electrodes using a time-division multiplexing scheme. The multiplexers select one amplifier in the column for readout, while the other 31 amplifiers are still in their integration phase and operates in a sequentially staggered readout pattern to minimize integration dead time and maximize their sensitivity.

CMOS fabrication foundries typically use an aluminum-copper (Al/Cu) alloy for the top metal layer, which is inadequate for neurotransmitter detection as it is highly reactive to electrolytic solutions. This highly reactive metal alloy results in significant current offsets, thus increasing the shot noise of the amplifiers. To make the electrode array suitable for

103

neurotransmitter detection, platinum electrodes are integrated onto the chip to provide a polarizable electrode material (Fig. 6.1c-e).
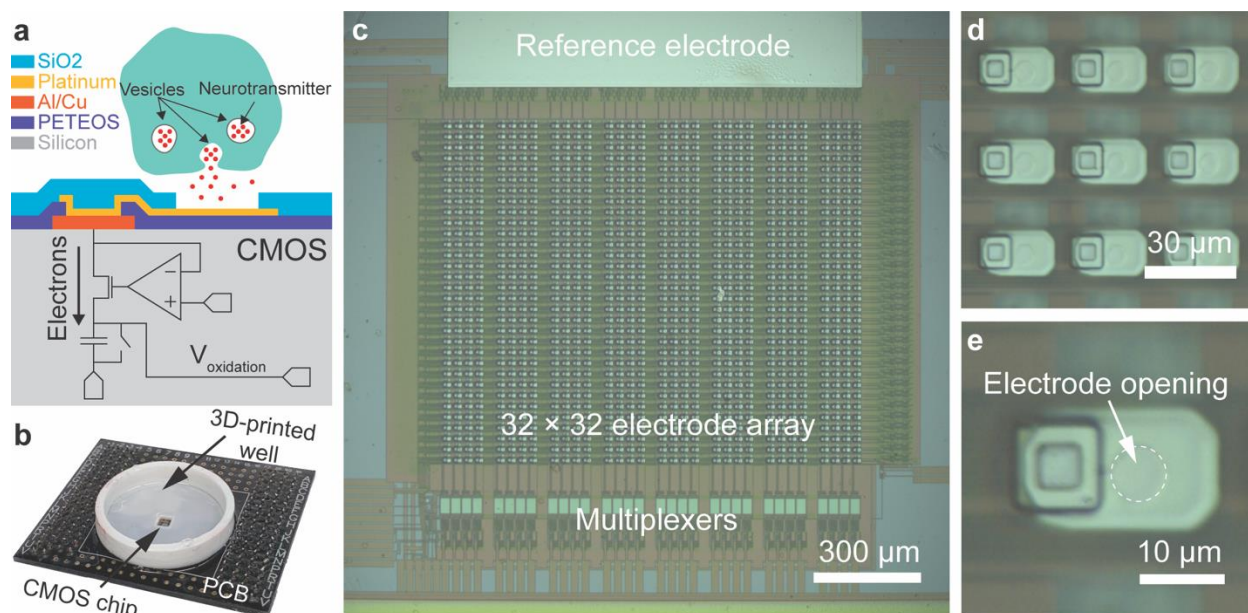
Figure 6.1: CMOS-based electrochemical detector array for high-throughput quantal analysis. (a) Neurotransmitters released from cells diffuse onto an electrode and undergo a redox reaction. The oxidation releases electrons into the electrode and results in electrical current at the amplifier, which allows a buildup of electrons onto one side of a capacitor, creating a current-dependent output, $V_{oxidation}$. The output of the amplifier is readout periodically and the capacitor is reset using a switch to begin the next detection period. (b) The device is bonded onto a PCB to interface the CMOS device to external electronics. The final packaging of the device includes a well that permits the addition of electrolytic solutions to the top of the electrode array for electrochemical experiments. (c) The CMOS-based electrochemical device contains an array of 32×32 electrode array wherein each electrode is connected to its own dedicated amplifier and a reference electrode is integrated on-chip next to the electrode array. To readout the 1024 parallel electrochemical detections of secreted neurotransmitters, each column is connected to a dedicated multiplexer. The multiplexers stagger the readout time for the amplifiers in its dedicated column, permitting the other 31 amplifiers to operate without deadtime. (d) A microphotograph of the 23 µm × 13 µm electrodes (white-colored rectangle) patterned throughout the array. (e) The oxide insulation layer is etched to provide an opening of approximately 5 µm above the platinum electrodes, providing an effective electrode area of 5 µm, which is comparable to the diameter of carbon fibers used for traditional single-cell electrophysiology techniques.

To integrate the new platinum electrodes onto the chip's surface, a post-CMOS processing is performed using a standard photolithography process. The chip is first processed using a

negative photoresist, NR9-1500PY, to create a sacrificial layer that defines where metal deposition is undesirable. After creating the sacrificial layer, 20 nm of titanium and then 200nm of platinum is deposited using sputtering (Kurt J. Lesker Multi-Source RF and DC Sputter System, Kurt J. Lesker Company, Jefferson Hills, PA). The sacrificial layer of photoresist is then removed by rinsing the chip with acetone. Once all of the photoresist is removed, the platinum electrodes are patterned as 23 x 13 µm rectangles as shown in Fig. 6.1d. A 300 nm passivation layer of silicon dioxide is then deposited onto the chip using a plasma-enhanced chemical vapor deposition machine (STS 310PC, STS Ltd., Wales, UK). To reopen the electrodes for neurotransmitter detection the chip undergoes another photolithography process using the negative photoresist NR7-1500P, resulting in a protective layer that only permits the etching of the oxide above the electrodes. After the protective layer is processed, the device is etched using a reactive ion etcher with inductively coupled plasma (Unaxis SLR, Unaxis Materials Inc., Santa Clara, CA). The etching process produces circular electrode openings through the oxide passivation layer that are approximately 5 µm in diameter as shown in Fig. 6.1e. To remove the remaining NR7 photoresist and clean the surface of the array, the device is put into a piranha solution (3:1 mixture of sulfuric acid:hydrogen peroxide). The resulting effective area of the electrodes throughout the array are comparable to the gold standard CFEs with diameters of ~5 µm [1], [4], [25], [97], [98].

After all post-CMOS processing is completed, the chip is packaged to integrate a reservoir structure that holds electrolytic solutions on the surface of the array and prevent damage to the wire bonds and interfacing electronics. The chip is first bonded to a custom-designed PCB to interface with a custom-designed multifunctional data acquisition system. Then, a 3D-printed ABS plastic well that is coated in polydimethylsiloxane (PDMS) is bonded to the surface of the electrode

array using additional PDMS. The fully packaged device is shown in Fig. 6.1b. After the device is packaged, the electrode array is coated with Poly-D-Lysine (PDL) to enhance the adhesion of cells to the electrode array during experiments as described in the methods section.

The amplifiers throughout the array have an average noise level of ~0.42 pA_{RMS} when the device is operating without electrolytic solution at a 10 kHz sampling rate and a bandwidth of ~4.4 kHz [24]. In comparison, a recent CMOS device has been developed for high-throughput recording of electrochemical current with an array of amplifiers that exhibit a noise level of 1.1 pA_{RMS} at a sampling rate of ~10 kHz with a bandwidth of ~2 kHz [99]. An electrode that is in contact with electrolytic solution suffers from an elevated noise level due to the introduced double-layer capacitance. Our previous design had an electrode area of 15 μm × 15 μm, and when electrolytic solution was placed onto the array for electrochemical experiments the noise level was 6.16 pA_{RMS} [24], which is higher than the average amplitude of PC-12 quantal events. The new post-CMOS processing presented in this chapter creates an electrode with a diameter of ~5 μm and produces an average noise of ~0.9 pA_{RMS} under the same conditions. In comparison, a study using a 5 μm diameter CFE with the Axopatch 200B amplifier, a high-quality electrophysiology amplifier, had a noise level of ~1.4 pA_{RMS} with a 10 kHz bandwidth [1]. Our electrochemical sensor array exhibits a comparable noise level to a high-quality electrophysiology setup, therefore enabling high-throughput recordings of quantal events from dopaminergic cells, such as PC-12 cells.

Based on the noise level of the presented device (~0.9 pA_{RMS}) and the typical half-width of amperometric spikes recorded from PC-12 cells (~5 ms), we can estimate the smallest quantal size that can be detected using this system. Because the integrated noise level for 5-ms events is about 0.14 pA_{RMS}, the quantal size equivalent noise level for 5-ms signal is ~2000 molecules.

6.4　On-chip Recordings at Single-vesicle Resolution.

Cells are loaded onto the surface of the electrode array as described in the methods section. Loaded cells are settled for 5 minutes to the surface of the array, then unattached cells are washed away. An example of randomly distributed cells over the electrode array is shown in Fig. 6.2a. The cells are present in single-cell form with diameters of 5-10 µm, as well as in clumps (Fig. 6.2b-c), throughout the array. Quantal events from the attached cells are recorded in parallel (Fig. 6.3a) with the electrodes throughout the array held at a potential of ~800 mV with respect to the reference electrode and the amplifiers operating at a 10 kHz sampling rate.

After a set of recordings are acquired with the device, the recorded exocytotic spikes (Fig. 6.3b) are analyzed using a quantal analysis program, Quanta Analysis v8.20 [10]. The analyzed characteristics of an exocytotic spike include the maximum amplitude of the signal (I_{max}), the duration of the signal at half of its maximum height ($t_{1/2}$), and the quantal size (Q) as illustrated in Fig. 6.3c. After 14 minutes of recording, 477 quantal events are detected from the control group (Fig. 6.4). In the control group, the average amplitude of the quantal events is 1.30 pA, the average half-width of these events is 7.33 ms, and the average quantal size is 14.3 fC.

6.5　Rapid Characterization of L-Dopa Therapy on Quantal Release in Minutes.

L-Dopa is used clinically for PD because it is known to increase the dopamine concentration in the central nervous system [2]. To validate the single-vesicle recording capability of the presented device, amperometric spikes for both untreated and L-Dopa-treated cells are measured and analyzed at the single-vesicle level. For untreated cells, the chip measured from a
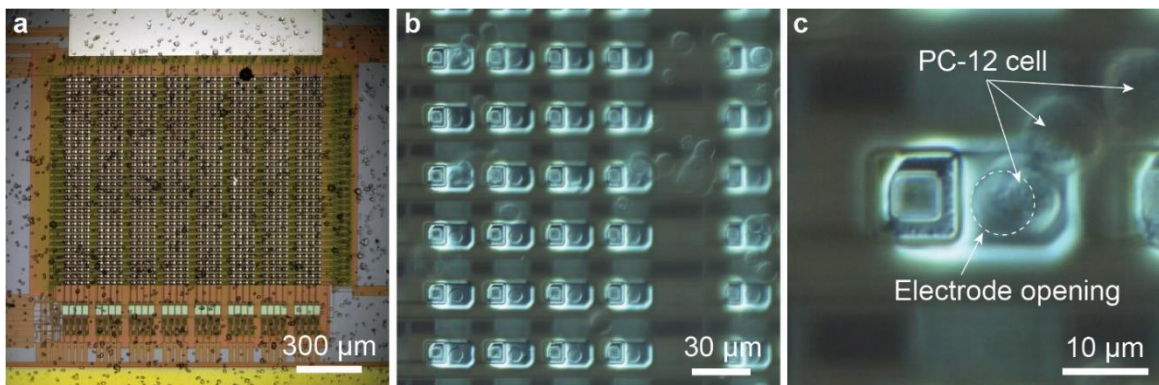
Figure 6.2: On-chip recording of PC-12 cells. (a) The settled cells on the surface of the device. (b) Cells are seen in single-cell form, as well as clumps of cells, throughout the electrode array. (c) Cells have settled atop the electrode openings, permitting electrochemical monitoring of quantal secretion.

total number of 16 cells and 477 quantal spikes in a 14-minute recording. For the L-Dopa-treated cells, a total number of 63 cells and 3534 vesicle secretions are measured, also in a 14-minute recording period. L-Dopa-treated cells have a noticeably higher number of quantal events compared to the untreated cells and the amplitude of each spike tends to be larger (Fig. 6.4a-b). The quantitative analysis on both treated and untreated cell recordings reveals significantly altered quantal release characteristics (Fig. 6.4c-f) from these short recordings. Mainly, the amplitude and the quantal size are increased with the L-Dopa treatment as anticipated because of L-Dopa's role as a dopamine precursor. The average spike amplitude for treated cells is 1.75 pA, as opposed to 1.30 pA of untreated cells (Fig. 6.4c). The half-width increased slightly after the L-Dopa treatment from 7.33 ms to 9.15 ms (Fig. 6.4d). The L-Dopa treatment increased the average quantal size by 86%, with the average quantal sizes being 26.6 fC and 14.3 fC for treated and untreated cells, respectively (Fig. 6.4e). The number of electroactive molecules contained within each vesicle is calculated as described in the methods section. The average number of molecules measured per

vesicle release for treated and untreated cells, respectively, are 83,100 and 44,600 molecules (Fig. 6.4f).

All recorded quantal events from both cell groups are also compared in histograms (Fig. 6.4g-j). Secretory cells regulate the vesicles in diameters (ϕ), and we expect to see a well-fitted Gaussian distribution of vesicle's diameter [100]. Quantal size is proportional to the volume of vesicles (ϕ^3) and plotting of (quantal size)$^{1/3}$ should produce a Gaussian distribution. As expected, the quantal size plots in attomole$^{1/3}$ show good agreements with Gaussian distributions for both treated and untreated cells as seen in Fig. 6.4j. The average quantal size in attomole$^{1/3}$ for L-Dopa treated cells is 0.50 ± 0.11 attomole$^{1/3}$ (mean $\pm$ SD) and is 0.40 ± 0.08 attomole$^{1/3}$ (mean $\pm$ SD) for the control group.
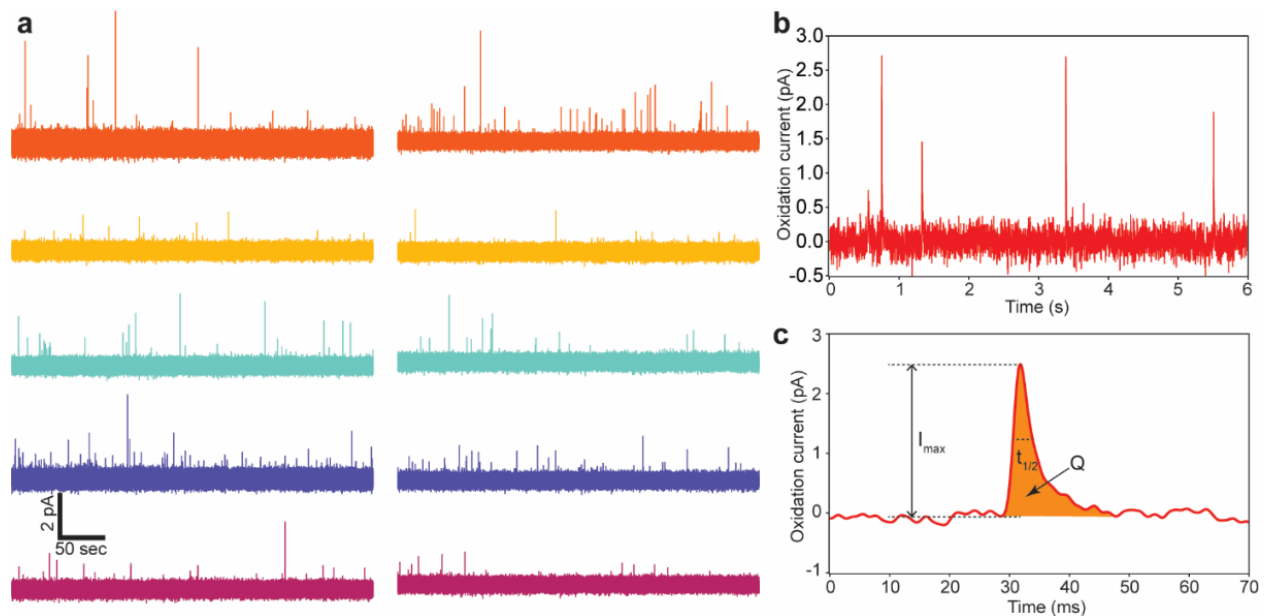
Figure 6.3: Parallel neurotransmitter secretion recordings. (a) Representative amperometric recordings from a single recording session. (b) A section of a recording showing the fast amperometric spikes related to vesicle release events. (c) Each exocytotic event is analyzed for key quantal release characteristics (maximum peak of the spike Imax, the half-width duration of the spike t1/2, and the quantal size Q).
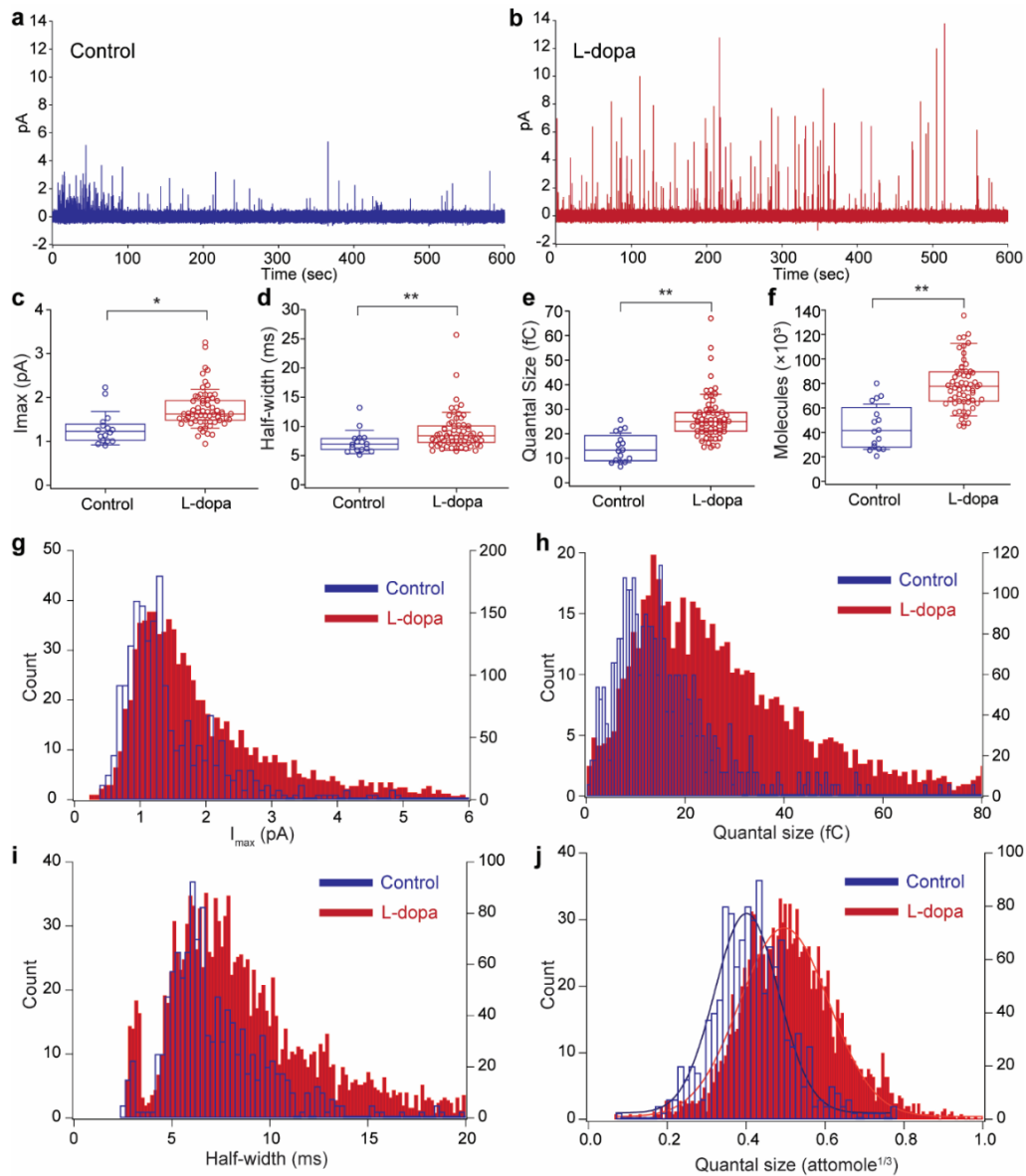
Figure 6.4: Vesicle secretion of neurotransmitter is modulated by L-Dopa treatment. (a) A representative recording from the control group. (b) A representative recording after L-Dopa treatment that exemplifies an alteration in neurotransmitter secretion characteristics. c-f After L-Dopa treatment, the quantal release characteristics of the PC-12 cells are significantly altered (n = 16 for control, n = 63 for L-Dopa, whiskers are drawn from the quartiles to the extreme values, the box is generated from the first and third quartile as well as median). (c) The average exocytotic spike amplitude increased from 1.3 pA to 1.75 pA after treatment. (d) The average half-width increased after treatment from 7.33 ms to 9.15 ms. (e) The average quantal size increased from 14.3 fC to 26.6 fC after L-Dopa treatment. (f) The change in quantal size correlates to an average molecule quantity increase from 44,600 to 83,100 for treated cells. (g-j) Histogram showing characteristics from all detected spikes. (two-tailed student t-test: * p < 0.01, ** p < 0.001)

6.6   Integration of Microwells for Isolating Single-Cells

To enable single-cell studies, a layer of SU-8 is integrated on top of each electrode, creating wells that are large enough to permit only a single cell from resting atop an electrode as shown in Fig. 6.5. The CMOS chip first undergoes the photolithography process to integrate the platinum electrode array with the integrated oxide passivation layer that creates 5 µm openings above each electrode. Then the protective photoresist used during the etching of the oxide layer is removed using resist remover RR4. The chip is cleaned using a piranha solution, Pure Strip, and then thoroughly rinsed using deionized water. The chip then undergoes a final photolithography process using SU-8 3010 to create the cell-isolating well structures that are nominally 15 µm × 15 µm. Microphotographs illustrating the isolation of single-cells to an electrode are shown in Fig. 6.6.

6.7   Desvenlafaxine and Selegiline

The new pharmacological substances that are studied in this chapter are desvenlafaxine and selegiline. Desvenlafaxine is a pharmacological substance that is used to treat depression and is a reuptake inhibitor for the neurotransmitters serotonin and norepinephrine, thus increasing extracellular levels of these neurotransmitters in the brain. On the other hand, Selegiline is a pharmacological substance that is used for Parkinson's disease as it is an inhibiter of monoamine oxidase (MAO), which oxidizes extracellular monoamines such as dopamine, and will increase extracellular levels of dopamine in the brain. To the best of my knowledge, these two pharmacological substances have not yet been studied using single-cell amperometry to reveal the effects of these drugs on the dynamics of neurotransmitter secretion.
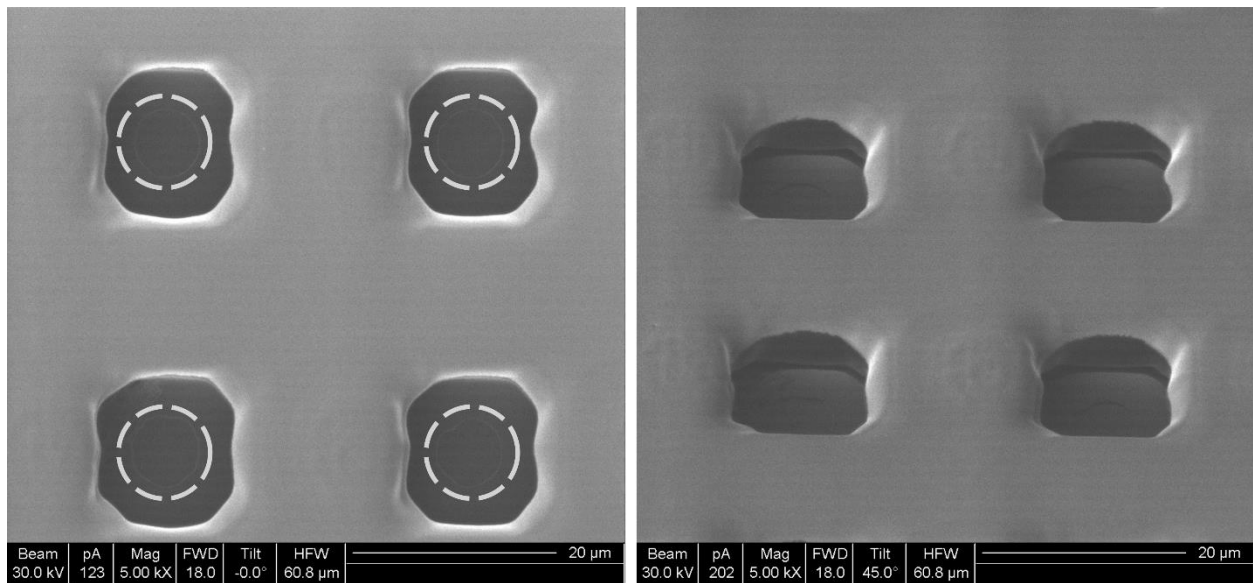
Figure 6.5: FIB imaging that shows the circular electrode openings inside the SU-8 well openings, which promote single-cell studies.
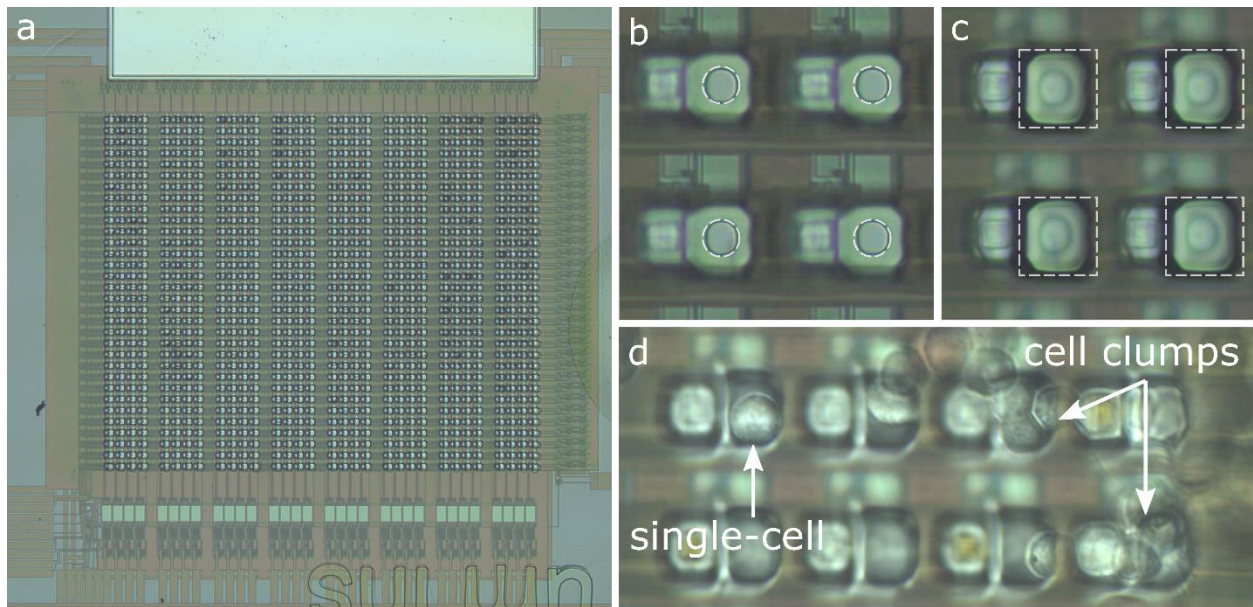
Figure 6.6: High-density neurochemical array for single-cell studies. (a) The 32×32 neurochemical array. (b) 5 µm electrode openings in the SiO_2 passivation layer. (c) ~15 µm well structures that permit a single-cell to sit atop an electrode. (d) Microphotograph of a single-cell resting in a well and cell clumps that fail to fit inside of the well.

Differentiated cells are used for this pharmacological screening and the analyzed characteristics of the recorded exocytotic events are the maximum amplitude of the signal (I_{max}), the duration of the signal at half of its maximum height ($t_{1/2}$), and the quantal size (Q) of the event. From two experimental preparations, neurotransmitter secretion was captured from 26 cells in the control group. This control group exhibits an I_{max} of 1.11 pA, a half-width of 46.0 ms, and a quantal size of 0.103 pC. Then secretion was captured from 29 cells (1 experimental preparation) in the serotonin treated group and 17 cells (1 experimental preparation) in the norepinephrine treated group. The serotonin treated group of cells show little difference compared to the control group and exhibits a lower I_{max} of 1.06 pA, a shorter half-width of 45.7 ms, and a smaller quantal size of 0.097 pC. However, the norepinephrine treated group exhibit a larger I_{max} of 1.74 pA, a shorter half-width of 20.6 ms, and a smaller quantal size of 0.061 pC, all of which are statistically significant ($p < 0.05$) compared to the control. For the new pharmacological treatment experiments, secretion was captured from 22 cells (1 experimental preparation) in the desvenlafaxine treated group and 55 cells (1 experimental preparation) in the selegiline treated group. The desvenlafaxine treated cells exhibit a larger I_{max} of 1.16 pA, a longer half-width of 64.6 ms, and a larger quantal size of 0.124 pC, of which only the half-width is different from the control with statistical significance ($p < 0.05$). For the selegiline treated cells, this group exhibits a larger I_{max} of 1.17 pA, a shorter half-width of 38.7 ms, and a smaller quantal size of 0.064 pC, all of which are similar to the control group. Plots summarizing the captured secretion characteristics are shown in Fig. 6.7.
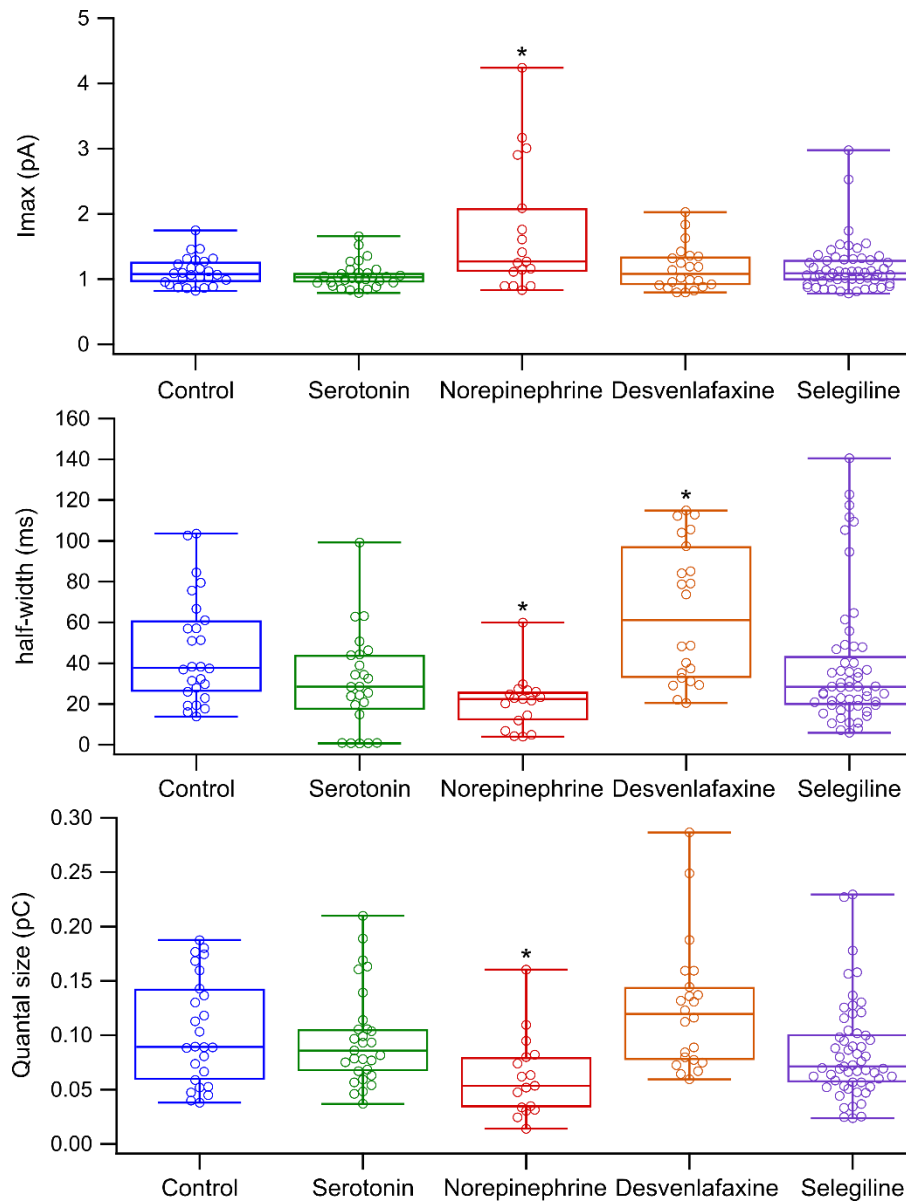
Figure 6.7: Pharmacological modulation of neurotransmitter secretion. Modulations include incubation with extracellular neurotransmitters, serotonin and norepinephrine, and treatment with pharmacological substances desvenlafaxine, an uptake inhibitor, and selegiline, a monoamine oxidase inhibitor. (a) The average amplitudes are 1.11 pA, 1.06 pA, 1.74 pA, 1.16 pA, and 1.17 pA for the control, serotonin, norepinephrine, desvenlafaxine, and selegiline experiments respectively. (b) The average half-widths are 46.0 ms, 45.7 ms, 20.6ms, 64.6 ms, and 38.7 ms for the control, serotonin, norepinephrine, desvenlafaxine, and selegiline experiments respectively. (c) The average quantal sizes are 0.103 pC, 0.097 pC, 0.061 pC, 0.124 pC, and 0.084 pC for the control, serotonin, norepinephrine, desvenlafaxine, and selegiline experiments respectively. [The boxes are generated from the first and third quartile as well as median and the whiskers are drawn from the quartiles to the extreme values.] (two-tailed student t-test: * $p < 0.05$)

6.8   Discussion

Using the presented CMOS integrated electrochemical sensors, we are able to perform hundreds of amperometric recordings in minutes as opposed to weeks using the conventional CFE approach [26]. Significant cost reduction in instrumentation for quantal release analysis will allow the rapid evaluation of existing and emerging treatments for their molecular effects on exocytosis.

Using the integrated silicon device, we were able to characterize the effects of L-Dopa treatment at the single vesicle level, and our results agreed with previous studies [2], [97], [101]–[104]. After treating PC-12 cells with L-Dopa we observed a 35% increase in I_{max} which is similar to the previous reports [101], [103]. Modulation of $t_{1/2}$ as a result of L-Dopa treatment has increased the duration of quantal events by 47% in MN9D cells [5] and by 10% [101], 38% [103], and as large as 88% [104] in PC-12 cells. Our results showed a similar increase in $t_{1/2}$ of 25% after L-Dopa treatment. Across all studies, L-Dopa treatment increases the quantal size within each vesicle; treated bovine chromaffin cells exhibited a 70% increase [105]; MN9D cells exhibited an increase of 40% [5]; PC-12 cells exhibited an increase of 20% [101], 26% [104], and 63% [103]; and our measurement showed an 86% increase in quantal size.

For the differentiated cells exposed to serotonin, the modulation in these parameters is minimal. Because PC-12 do not express serotonin, there may not be an efficient uptake mechanism compared to the naturally expressed dopamine or norepinephrine. The cells exposed to norepinephrine show an increase in I_{max} (56%) and a decrease in the half-width (55%) and quantal size (41%) with statistical significance ($p<0.05$) (Fig. 6.7). For the new pharmacological studies (Fig. 6.7), desvenlafaxine exhibits a longer half-width, 40% longer compared to the control, that is statistically significant ($p < 0.05$). However, the selegiline treatment does not exhibit statistically

significant modulation of secretion characteristics. This reveals that the selegiline exposure and dosage detailed in the methods section may not modulate secretion characteristics and higher dosage and longer exposure may reveal some unknown effects at the single-cell level.

6.9   Methods

6.9.1   Recording and Stimulation Solutions

The recording bath solution consists of 150 mM of NaCl, 5mM of KCl, 2 mM of $CaCl_2$, 1.2 mM of $MgCl_2$, 10 mM of HEPES, and 11 mM of Glucose. Additional glucose was added to adjust the osmolality of the recording solution to 320 mmol/kg and the pH was adjusted to 7.3 using NaOH. The high K^+ stimulation solution consists of 55 mM of NaCl, 100mM of KCl, 5 mM of $CaCl_2$, 2 mM of $MgCl_2$, 10 mM of HEPES, and 10 mM of Glucose. The stimulation solution's osmolality was adjusted to 320 mmol/kg by adding glucose to match the osmolality of the recording bath solution and the pH was adjusted to 7.3 using NaOH. Both solutions were prepared using water from a purification system and then further filtered after preparation to ensure their sterility.

6.9.2   PC-12 Cell Culture

The PC-12 cells were obtained from the American Type Culture Collection (ATCC) (Manassas, VA) and were cultured using T-75 flasks in an incubator at 37ºC with 5% CO_2. The culture media consists of RPMI-1640 (Gibco) media that was supplemented with 10% heat-inactivated horse serum (Gibco), 5% fetal bovine serum (ATCC), and 1% penicillin-streptomycin (Gibco). The media was changed every 2-3 days and the cells were subcultured when the cell density was approximately 4×10^6 cells/mL. The cells used for the control group and the L-Dopa

treated group are first split from one flask into two separate flasks the day of, or before the on-chip measurement.

For the experiments using differentiated cells, cells are treated with 5 µM of dexamethasone, a differentiation path that has been found to enhance the excitability of PC-12 cells when stimulated [107]. These differentiated cells are treated and loaded onto the neurochemical microelectrode array for monitoring neurotransmitter secretion on days 5-8 after differentiation is initiated.

6.9.3   Experimental Procedure

Cells were first detached from their flasks by a washing process using culture media and the cell concentration was adjusted to approximately 2×10^6 cells. The detached cells were first spun down to a pellet in a centrifuge at 200g for 5 minutes. The supernatant was discarded, 5 mL of the recording solution was added, and the cells are resuspended using a 20 mL syringe with a 22-gauge needle. The cells were once again spun down to a pellet at 200g for 5 minutes, the supernatant was discarded, and 1 mL of new recording solution was added. The approximate 2×10^6 cells were resuspended once more and then 20 µL of this cell solution was loaded directly onto the electrode array. Once loaded onto the device, the cells were given 5 minutes to settle to the surface of the array. During this settling period, a prepared Ag|AgCl wire reference electrode was placed into the well. Any unattached cells were removed from the device by washing the array with more recording solution using a perfusion system. To treat the electrode array with PDL (Gibco), the device was incubated with 0.1-mg/mL PDL solution on top of the array for 1 hour.

The device was then rinsed thoroughly using deionized water and dried for at least 1 hour before the array's first electrochemical experiment.

A brief recording of the quantal release from non-stimulated cells resting on the electrode array was performed before the high K^+ stimulation solution was added to the electrode array. The stimulation solution was then added using a perfusion system, which was operated for about 1 minute to saturate the cells with the exocytosis-inducing stimulant. The recording lasted for 14 minutes after the first stimulation. After the cells have rested for at least 5 minutes following the first stimulation, the perfusion system was used again to add more of the high K^+ stimulant to re-stimulate the cells halfway through the recording period. When performing experiments with L-Dopa treated cells, the cells are exposed to 100 µM of L-Dopa for 1 hour prior to executing the cell loading process. To determine the viability of the cells during the recordings of neurotransmitter secretion, trypan blue was added to the electrode array after all recordings are complete. The solution on the array was first exchanged with fresh recording bath solution and then drained until 1 mL of solution remains. Then, 1 mL of trypan blue was added to the well to stain any dead cells atop the array. After 5 minutes of cell staining, the trypan blue was removed by perfusion and exchanged with new recording solution and the array was inspected using a microscope.

For experiments using differentiated cells, the cells are first removed from the flask and then spun down to a pellet in a centrifuge at 200g for 5 minutes. Then the media is removed and the cells are treated with 2 ml of Trypsin (0.25% EDTA) for 2 minutes and are lightly aspirated using a pipette. Then 8 mL of culture media is used to neutralize the Trypsin and the cells are spun down to a pellet in a centrifuge at 200g for 5 minutes. The supernatant is then removed, 5 mL of

fresh media is added, and the cells are resuspended using a 20 mL syringe with a 22-gauge needle. Then 20 mL of fresh media is added and cells are removed for counting. After counting, approximately 2×10^6 cells are removed and spun down to a pellet in a centrifuge at 200g for 5 minutes. The supernatant is removed and1 mL of calcium and magnesium-free phosphate-buffered saline is added to inhibit cell clumping during the loading procedure. The cells are resuspended using a 20 mL syringe with a 22-gauge needle. Then the 20 µL of cells are loaded onto the array and given 10 minutes to settle into the SU-8 wells (Fig. 6.6d).

For these experiments, the differentiated cells undergo the following treatments. To study the reuptake inhibition effects of desvenlafaxine, an experimental group of cells are treated with 10 µM of serotonin for 30 min. Then for the desvenlafaxine group of cells, they are first treated with 5 µM of desvenlafaxine for 30 min and then 10 µM of serotonin is introduced to the cells for 30 min. Another uptake experiment is performed using the PC-12 cells to address concerns about the efficiency of serotonin uptake from these cells as they do not naturally express serotonin in their vesicles, but they do express norepinephrine and dopamine. The second uptake experiment exposes the cells to 100 µM of norepinephrine for 60 min. The selegiline group of cells are treated with 5 µM of selegiline for 30 min.

6.9.4   Statistical Analysis

All of the cell recordings are analyzed in Igor Pro 8 using Quanta Analysis version v8.20 [10]. All recordings are filtered with a 1 Hz high pass filter, to remove low-frequency fluctuations resulted from perfusion steps, and a low pass binomial smoothing set to 100 Hz. Signals are detected as quantal events when the signal's first-order time derivate is 5 times greater than the

standard deviation of the background noise. All individual exocytotic spikes are analyzed for their quantal size, amplitude, half-width, and number of molecules. The quantal size was calculated based on the integration of the electrochemical current induced during an exocytotic spike in pico-coulomb (pC). The amplitude is determined from the baseline to the peak of each spike in pico-ampere (pA). The number of molecules released per vesicle can be calculated by dividing the quantal size by 2q (q is the electron charge). Exocytotic events from individual cells are heterogeneous and overrepresentation is possible from cells that are highly active [102]. In order to prevent the overrepresentation of highly-active cells, the median value of all the spikes from a single cell is used as n (each sample) in the statistical analysis, rather than using individual spikes as n. This method is consistent with other amperometric studies[24], [34], [108], [109].

6.10 Conclusion

Using the presented CMOS integrated electrochemical sensors, we are able to acquire numerous amperometric recordings in an experiment, providing rapid results compared to the conventional amperometry technique that can take from weeks to months to amass a comparable dataset [26]. Using the integrated silicon device, we were able to characterize the effects of L-Dopa treatment at the single vesicle level and we were able to study the secretion modulation by serotonin uptake, norepinephrine uptake, desvenlafaxine treatment, and selegiline treatment at the single-cell level. This chapter illustrates the high-throughput screening capabilities of the system developed in this dissertation. Using this novel technology, we can significantly accelerate the study of neurodegenerative disorders, such as Parkinson's disease and Alzheimer's disease, as well

as new pharmacological treatments that affect neurotransmitters in the brain at the single-cell level, such as drugs for depression or Parkinson's disease.

CHAPTER 7: NEUROTRANSMITTER-MEDIATED BIOHYBRID SYNAPSE

7.1   Chapter Notes

Bio-inspired computing revolutionizes machine learning and artificial intelligence by mimicking the efficient biological systems. Artificial neural networks (ANNs) are inspired by the brain, in which the synaptic connectivity between neurons achieves complex classification and data processing tasks. Although ANNs closely emulate the biological neural network (BNN), the BNN relies heavily on neurochemical synaptic transmission which contributes to the stochastic computing of the brain. In biological synapses, membrane-bound neurotransmitters are released in quantal events to the extracellular space at the synaptic clefts. In this chapter, a new biohybrid synapse that produces quantal neurotransmitter secretion to relay information to the artificial postsynaptic receptor is discussed. The neurochemical biohybrid synapse paves the way for a new generation of brain-inspired computing by enabling single biological cell to single artificial neuron connectivity. We also demonstrate the dynamic synaptic weighting in the biohybrid synapse which affects synaptic activities. The work described in this chapter was completed with Mingjie Lin and Brian N. Kim.

7.2   Introduction

The brain excels in sophisticated learning and control tasks compared to the modern computing machinery, despite using significantly less computation resources. Neurons receive inputs from thousands of excitatory synapses which enables them to recognize multiple independent patterns despite the presence of noise and pattern variation. Recent advances in bio-inspired computing mimic certain aspects of biological neural networks, such as parallel

distributed information processing, spike-time encoding, synaptic plasticity, and homeostasis. However, artificial intelligence needs new hardware, not just new algorithms, to advance the dimensionality of synaptic connectivity. The scalability of silicon circuits is limited as we reach the end of Moore's law and there is no clear solution to form thousands of synaptic connections from each processing unit. The vision of our work here is to take advantage of biological intricacy and sophistication as parts of the computing solution, rather than to view them as complex problems. As such, biological tissues, such as the cortex neural layer, are no longer seen as unfathomable living materials, but rather as potential computational resources.

Artificial neural networks (ANNs) are inspired by the brain, wherein the synaptic connectivity between neurons achieves complex classification and data processing tasks. Although ANNs closely emulate the biological neural network (BNN), one important distinction between the two is that the BNN relies heavily on neurochemical synaptic transmission which contributes to the stochastic computing of the brain. In biological synapses, intracellular neurotransmitters are bound in vesicles (quanta) which are then released in quantal events to the extracellular space through exocytosis at the synaptic clefts (Fig. 7.1a). Although the exocytotic events are moderately coordinated with neuronal excitation, the number of vesicles that participates in neurotransmitter secretions, and the timing of exocytosis, appear to be random in nature. Also, some portion of neurotransmitter secretions is non-regulated and can occur without any excitation. These characteristics are referred to as synaptic noise and are attributed to the imprecise operation of the human brain [110], [111]. Nonetheless, the stochasticity is one of the defining qualities of the human brain that enables energy- and resource-efficient computing.

Previous work has demonstrated the biohybrid concept to merge biological tissue into electronic devices [112]. Neuroendocrine cells are interfaced with a PEDOT:PSS transistor, which serves as the post-synaptic cleft. The published work has demonstrated short-term and long-term modulation of a biohybrid synaptic channel by voltage pulse induced ion flow into the synaptic channel and irreversible modulation of the synaptic channel due to oxidation of neurotransmitters, such as dopamine, respectively. However, this biohybrid synapse does not approach emulation of neural synapses as a single postsynaptic connection interfaces with multiple presynaptic cells. Also, it does not capture the individual vesicular secretion events, which is a key characteristic of synaptic transmission in a biological synaptic cleft.

In this chapter, we introduce a new biohybrid synapse that communicates through vesicular secretion, which mirrors the neuronal synaptic communications, to relay information to the artificial postsynaptic receptor (Fig. 7.1b). The biohybrid synapses pave the way for a new generation of brain-inspired computing by enabling single biological cell to single artificial neuron connectivity. The proposed biohybrid technology can achieve two purposes: (1) serving as a part of artificial intelligence interconnecting a biological layer to an artificial layer (Fig. 7.1c), (2) being an independent reservoir computing device that can utilize the complex biological synaptic connectivity (Fig. 7.1d) (1000s of synaptic connections per neuron, compared to 10s in an artificial neural network), which is crucial in the efficient computing of the human brain.

7.3 Neurochemical Biohybrid Synapse

Each biohybrid synapse integrates a neuroendocrine single cell (PC-12) and a neurochemical microelectrode. The neuroendocrine cells natively release dopamine molecules in quantal events

which is identical to dopaminergic neurons [113]. The integration of single cells enables the biohybrid synapse to connect one biological cell to an individual artificial neuron. Thusly, the neurochemical sensor must be able to detect and quantify the fast neurotransmitter release events which are occurring at the single-vesicle level.
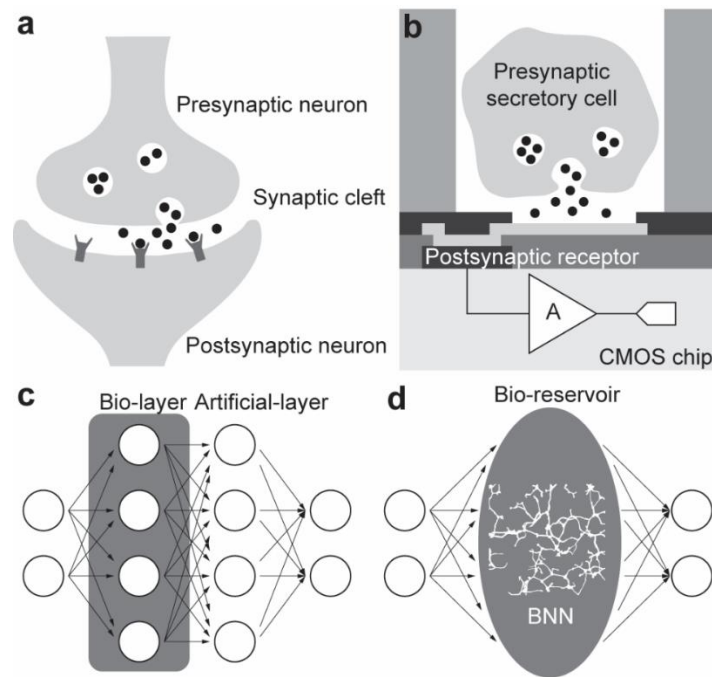
Figure 7.1: Neurotransmitter-mediated biohybrid synapse using single-cell neurochemical sensor. (a) In the synaptic cleft, neurotransmitters are released in quantum (vesicle). (b) The new biohybrid synapse integrates a presynaptic secretory cell which can secrete neurotransmitters in quantal events. Each biohybrid synapse measures neurochemical secretions at a quantum resolution which can then be used to interact with the artificial neural network. (c) Using biohybrid synapses, biological tissue can be integrated as a part of a neural network which can achieve computing tasks. (d) Also, reservoir computing using a biological neural network can be achieved using biohybrid synapses as the interface.

7.3.1   Design of Biohybrid Synapse

To achieve this, we have previously designed a neurochemical microelectrode array (MEA) using complementary metal-oxide-semiconductor (CMOS) technology which is capable of resolving neurotransmitter secretion events with single-vesicle resolution [24], [34], [51], [61],

[114], [115]. To the best of our knowledge, our neurochemical CMOS-MEA has the lowest noise level ($\sim$0.4 pA$_{RMS}$ at 10 kS/s) for a large MEA [114]. The CMOS-MEA integrates 1024 neurochemical sensors into a single device which can be used to establish high-throughput connectivity between BNNs and ANNs. The CMOS device is first fabricated using a standard 0.35 µm CMOS process. The CMOS chip contains 1024 integrated transimpedance amplifiers in a 32 $\times$ 32 array. The integrated transimpedance amplifiers are based on an integrating capacitor design in which the electrode node is regulated by the negative feedback of an operational amplifier. The oxidation current caused by the electroactive neurotransmitter molecules is integrated in the capacitor which results in a current-dependent voltage output. This output voltage is readout by a time-division multiplexer which reads from 32 amplifiers in a column. Each column of 32 amplifiers has its own dedicated multiplexer. The on-chip MEA is integrated directly on the CMOS chip by post-CMOS processing. The post-CMOS processing is performed using a standard photolithography process. First, the platinum layer is patterned using a lift-off process. Then, a thin silicon dioxide (300 nm) layer is deposited and etched to pattern an electrode passivation layer. Small openings to the platinum layer formed by the silicon dioxide layer define the effective microelectrode size (5 µm in diameter). After the integration of the on-chip MEA, a 20-µm layer of SU-8 is patterned above the neurochemical CMOS-MEA. The SU-8 layer serves as a single-cell isolator, which filters cells by size and only permits single cells to make contact with the neurochemical sensors to form the hybrid synapse. Clumps of cells will be rejected by the SU-8 because they will be too large to fit through the SU-8-defined openings (Fig. 7.2).

The electrode passivation layer enables the detection of neurotransmitter secretion with single-vesicle resolution by reducing the effective area of the electrode. The reduced electrode area
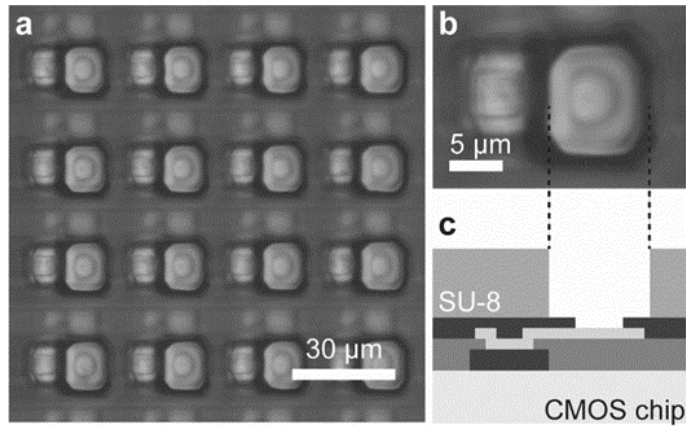
Figure 7.2: High-density single-cell neurochemical sensor array. (a) The neurochemical sensor integrates on-chip electrodes. The electrode opening is defined by a layer of SiO2. Subsequently, a layer of SU-8 is patterned on the neurochemical sensor to produce single-cell biohybrid synapses. (b-c) The SiO2 opening is 5 µm in diameter. The SU-8 opening is 12 µm in diameter. The single-cell diameter of PC-12 cells is ~7 – 10 µm and therefore the cells will fit into the SU-8 opening.

confines the area of the electrode-electrolyte interface, which directly affects the double-layer capacitance at this interface. This double-layer capacitance significantly affects the noise response of the transimpedance amplifier. Without the electrode passivation, the 15 μm electrode area has exhibited an average noise level of ~6.16 pA$_{RMS}$ (Fig. 7.3) [24]. When introducing the passivation layer that defines an active area of 5 μm, the electrodes exhibit an average noise level of ~0.9 pA$_{RMS}$ (Fig. 7.3) [114]. This significant noise improvement enables the detection of single-vesicle neurotransmitter secretion from PC-12 cells which have small quantal content.

7.3.2   Neurotransmitter-mediated Synaptic Transmission

Using the single-cell neurochemical sensor, we demonstrate the neurotransmitter-mediated biohybrid synapse (Fig. 7.4). For *in-vitro* models of presynaptic neuron cells, neuroendocrine PC-12 cells are used. The cells are cultured at 37˚C in RPMI-1640 media supplemented with 10% horse serum, 5% fetal bovine serum, and 1% penicillin-streptomycin. Additionally, the cells are

127
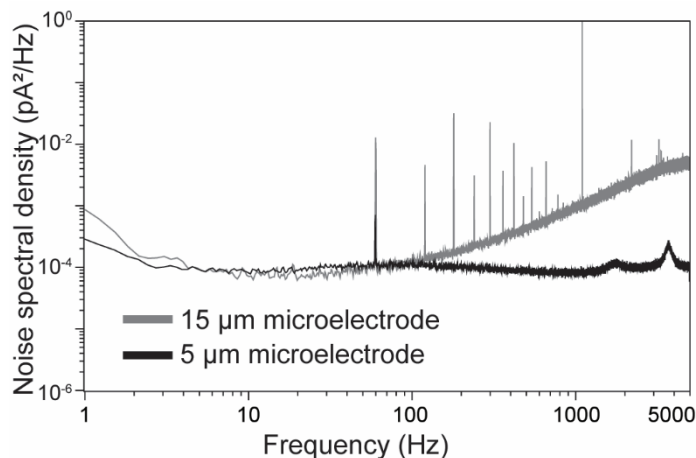
Figure 7.3: Noise spectral density of a 15 µm microelectrode and 5 µm microelectrode. The large electrode experiences a large double-layer capacitance from the electrode-electrolyte interface. The large input capacitance attached to the transimpedance amplifier contributes to the high-frequency noise, which is significant in the 15 µm microelectrode. The small 5 µm microelectrode does not exhibit any high-frequency noise from the input capacitance within the measurable bandwidth.

differentiated with 5 µM of dexamethasone, which enhances the excitability of the cells to stimulation [107]. On days 5-8 after differentiation is initiated, the PC-12 cells are loaded onto the chip and single PC-12 cells are contained atop a neurochemical microelectrode (Fig. 7.4a). The PC-12 cells spontaneously release dopamine molecules without any stimulation. Each quantal release is measured by a spike, which corresponds to a single-vesicle neurotransmitter release from the cell membrane (Fig. 7.4b).

The observed neurochemical secretions are stochastic, and the size of each quantal secretion is also random. The amplitude of spikes varies from 0.5 – 15 pA with an average of 4.47 pA. The average half-width (duration) is 38.3 ms, ranging from 8 – 122 ms. Using the integration of the oxidation current measured from each spike, we can estimate the quantal size of each vesicle. The average quantal size is 0.31 pC, which corresponds to 9.77×10^5 neurotransmitter molecules
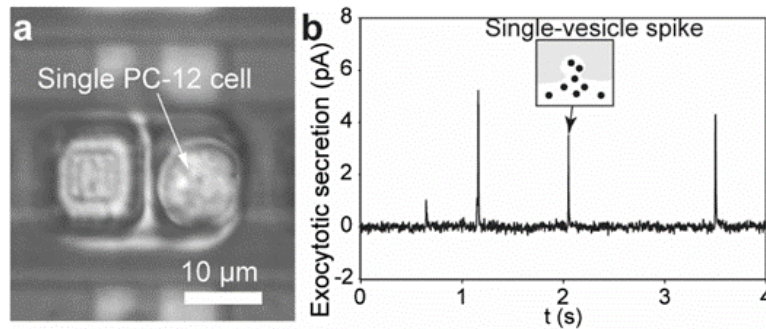
Figure 7.4: Single-cell biohybrid synapse. (a) Microphotography of a single PC-12 cell loaded into the SU-8 well. (b) The exocytotic events within the biohybrid synapse are mediated by the same vesicle fusion process, which mediates the neurotransmitter signal transmission within a biological synaptic cleft. Each spike monitored corresponds to a single vesicle secretion event.

per vesicle. Based on this experiment, this biohybrid synapse closely mimics the mechanism of synaptic transmissions which are neurotransmitter mediated.

7.4   Synaptic Plasticity in Biohybrid Synapse

For the biohybrid synapses to be applicable to be a part of computation machinery, it is crucial to demonstrate synaptic plasticity. In biological cells, multiple approaches can be adapted to show synaptic plasticity, either short-term or long-term. For example, neurons can commonly be triggered to increase synaptic activities by inducing calcium influx. This effect is short-term and, therefore, neurons can recover to the pre-stimulated condition in a few minutes. Pharmacological modulations can have long-term effect in synaptic transmission which affects underlying mechanisms of vesicle trafficking and exocytosis. For example, L-Dopa, a Parkinson's disease treatment, can increase the number of neurotransmitters in each vesicle, and therefore, increase the quantal size as well as the amplitude of each spike [2].

In this section, we demonstrate the dynamic short-term synaptic plasticity by triggering calcium influx (Fig. 7.5a-b). At the start of the neurochemical recording, the biohybrid synapse
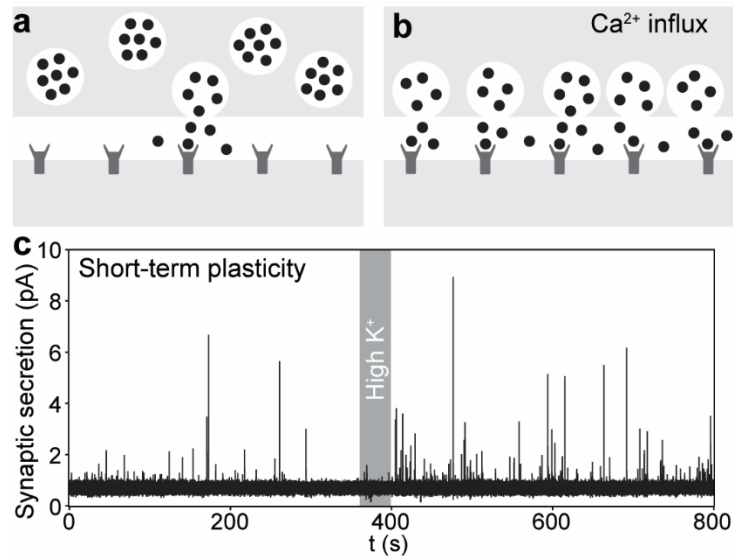
Figure 7.5: Dynamic synaptic plasticity in biohybrid synapses. (a) In the synaptic cleft, vesicles undergo spontaneous release which causes neurotransmitter secretion. (b) Upon calcium influx, a greater population of vesicles undergoes exocytosis which results in a significant extracellular neurotransmitter concentration. (c) In the biohybrid synapses, the calcium influx can be used to modulate the synaptic weight, causing a temporary increase of exocytotic activities. This experiment shows the short-term plasticity of biohybrid synapses.

exhibits the spontaneous release of neurotransmitters (Fig. 7.5c). At around 380 seconds, a calcium influx is induced by introducing a high concentration of potassium (70 – 140 mM) in the extracellular space for ~60 seconds. By triggering calcium influx, vesicle populations primed at the membrane undergo exocytosis to release their neurochemical content. After the modulation, the synaptic activity is increased with frequent single-vesicle secretion events compared to the pre-modulation condition. The increased synaptic activity is temporary as it is expected to return to the spontaneous level in a few minutes.

7.5   Conclusion

This biohybrid approach has several unique advantages over ANNs: (1) the integration of living neural tissues with natural computing power into functional computing machinery, (2) the

neurochemical synaptic transmission closely mimics neuronal synaptic connectivity, (3) the synaptic plasticity is non-deterministic which enables the stochastic computing of the human intelligence in *in vitro* electronic devices. By implementing biohybrid synapses into computing machinery, we will be able to generate stochastic computing architectures which are highly fault-tolerant and resilient, because any local perturbations of computing accuracy can dissipate globally and remain inconsequential to the output [116], [117].

In an effort to interface with a large neural network, the presented work provides a highly scalable technology. Because the biohybrid synapse is designed in a CMOS chip, tens of thousands of identical biohybrid synapses can be fabricated in a small surface (~a few mm^2) in order to interface with a complex BNN.

7.6   Discussion

Our future goal is to use this biohybrid synapse technology to stitch the biological fabric (BNN) and the artificial fabric (ANN) into a single computing machinery, enabling a new paradigm of biocomputing. To achieve this, we are investigating scalable methods to establish input to interface with the biohybrid synapse. One approach is to add the input layer to these neurotransmitter-mediated biohybrid synapses using a form of voltage stimulation.

CHAPTER 8: CONCLUSION AND FUTURE DIRECTION

The presented monolithic CMOS-based neurotransmitter detection system can capture a large pool of quantal events in the span of minutes, providing rapid results compared to the conventional amperometry technique that can take from weeks to months to amass a comparable dataset [26]. Using this novel technology, we can significantly accelerate the study of neurodegenerative disorders, such as Parkinson's disease and Alzheimer's disease, as well as new pharmacological treatments that affect neurotransmitters in the brain at the single-cell level, such as drugs for depression or Parkinson's disease. One of the future goals of this system is to reveal the unknown modulation of neurotransmitter secretion at the single-cell level by a pharmacological substance. By understanding the effects that pharmacological substances have at the single-cell level, drugs may become applicable for new therapeutic cases. Another future goal is to use this biohybrid synapse technology to stitch the biological fabric (BNN) and the artificial fabric (ANN) into a single computing machinery, enabling a new paradigm of biocomputing.

APPENDIX: PERMISSION LETTERS TO REPRINT ARTICLES IN THIS DISSERTATION

IEEE reprint permission letter for [24], [61], [115]

Dear Kevin White,

. The IEEE does not require individuals working on a dissertation/thesis to obtain a formal reuse license however, you must follow the requirements listed below:

Textual Material

Using short quotes or referring to the work within these papers) users must give full credit to the original source (author, paper, publication) followed by the IEEE copyright line © [Year of publication] IEEE.

In the case of illustrations or tabular material, we require that the copyright line © [Year of original publication] IEEE appears prominently with each reprinted figure and/or table.

If a substantial portion of the original paper is to be used, and if you are not the senior author, also obtain the senior author's approval.

Full-Text Article

If you are using the entire IEEE copyright owned article, the following IEEE copyright/ credit notice should be placed prominently in the references: © [year of original publication] IEEE. Reprinted, with
permission, from [author names, paper title, IEEE publication title, and month/year of publication]

Only the **accepted** version of an IEEE copyrighted paper can be used when posting the paper or your thesis on-line. You may not use the **final published** version

In placing the thesis on the author's university website, please display the following message in a prominent place on the website: In reference to IEEE copyrighted material which is used with permission in this thesis, the IEEE does not endorse any of [university/educational entity's name goes here]'s products or services. Internal or personal use of this material is permitted. If interested in reprinting/republishing IEEE copyrighted material for advertising or promotional purposes or for creating new collective works for resale or redistribution, please go to

http://www.ieee.org/publications_standards/publications/rights/rights_link.html

to learn how to obtain a License from RightsLink.

If applicable, University Microfilms and/or ProQuest Library, or the Archives of Canada may supply single copies of the dissertation.

Kind regards,

M.E. Brennan

Springer Nature reprint permission letter for [114]

Dear Kevin,

Thank you for your recent Springer Nature permissions request.

As an author, you retain certain non-exclusive rights over the 'Published Version' for which no permissions are necessary as long as you acknowledge and reference the first publication. These include:

- The right to reuse graphic elements contained in the Article and created by you in presentations or other works you author
- The right of you and your academic institution to reproduce the Article for course teaching. Note, this does not include the right to include in course packs for resale by libraries or by the institution
- To reproduce, or allow a third party to reproduce the Article in whole or in part in any printed volume (book or thesis) authored by you.
-

You may also wish to refer to our 'Reprints and Permissions' FAQs on Springer.com: https://www.springernature.com/gp/partners/rights-permissions-third-party-distribution

-
Best wishes,
Bod

Bod Adegboyega
Permissions Assistant
Springer Nature

LIST OF REFERENCES

[1]   E. N. Pothos, V. Davila and D. Sulzer, "Presynaptic recording of quanta from midbrain dopamine neurons and modulation of the quantal size.," *J. Neurosci.*, vol. 18, no. 11, pp. 4106–18, Jun. 1998.

[2]   E. Pothos, M. Desmond and D. Sulzer, "L-3,4-dihydroxyphenylalanine increases the quantal size of exocytotic dopamine release in vitro.," *J. Neurochem.*, vol. 66, no. 2, pp. 629–36, Nov. 1996.

[3]   B. Scatton, F. Javoy-Agid, L. Rouquier, B. Dubois and Y. Agid, "Reduction of cortical dopamine, noradrenaline, serotonin and their metabolites in Parkinson's disease," *Brain Res.*, vol. 275, no. 2, pp. 321–328, Sep. 1983.

[4]   R. M. Wightman, J. A. Jankowski, R. T. Kennedy, K. T. Kawagoe, T. J. Schroeder, D. J. Leszczyszyn, J. A. Near, E. J. Diliberto and O. H. Viveros, "Temporally resolved catecholamine spikes correspond to single vesicle release from individual chromaffin cells.," *Proc. Natl. Acad. Sci. U. S. A.*, vol. 88, no. 23, pp. 10754–8, Dec. 1991.

[5]   Y. Dong, M. L. Heien, M. M. Maxson and A. G. Ewing, "Amperometric measurements of catecholamine release from single vesicles in MN9D cells.," *J. Neurochem.*, vol. 107, no. 6, pp. 1589–95, Dec. 2008.

[6]   M. Criado, A. Gil, S. Viniegra and L. M. Gutiérrez, "A single amino acid near the C terminus of the synaptosome-associated protein of 25 kDa (SNAP-25) is essential for exocytosis in chromaffin cells," *Proc. Natl. Acad. Sci. U. S. A.*, vol. 96, no. 13, pp. 7256–7261, Jun. 1999.

[7]   Q. Fang, Y. Zhao, A. D. Herbst, B. N. Kim and M. Lindau, "Positively charged amino acids at the SNAP-25 C terminus determine fusion rates, fusion pore properties, and energetics of tight SNARE complex zippering.," *J. Neurosci.*, vol. 35, no. 7, pp. 3230–3239, Feb. 2015.

[8]   R. G. W. W. Staal, E. V. Mosharov and D. Sulzer, "Dopamine neurons release transmitter via a flickering fusion pore," *Nat. Neurosci.*, vol. 7, no. 4, pp. 341–346, Apr. 2004.

[9]   D. Evanko, "Primer: spying on exocytosis with amperometry," *Nat. Methods*, vol. 2, no. 9, pp. 650–650, Sep. 2005.

[10]   E. V Mosharov and D. Sulzer, "Analysis of exocytotic events recorded by amperometry.," *Nat. Methods*, vol. 2, no. 9, pp. 651–8, Sep. 2005.

[11]   N. Wittenberg, M. Maxson, D. Eves, A.-S. Cans and A. G. Ewing, "Electrochemistry at the Cell Membrane/Solution Interface," *Electrochem. Methods Neouroscience*, pp. 285–314, 2007.

[12]   E. Alés, L. Tabares, J. M. Poyato, V. Valero, M. Lindau and G. A. De Toledo, "High calcium concentrations shift the mode of exocytosis to the kiss-and-run mechanism," *Nat. Cell Biol.*, vol. 1, no. 1, pp. 40–44, 1999.

[13]   D. M. Omiatek, Y. Dong, M. L. Heien and A. G. Ewing, "Only a fraction of quantal content is released during exocytosis as revealed by electrochemical cytometry of secretory vesicles," *ACS Chem. Neurosci.*, vol. 1, no. 3, pp. 234–245, Mar. 2010.

[14]   G. T. H. Van Kempen, H. T. Vanderleest, R. J. Van Den Berg, P. Eilers and R. H. S. Westerink, "Three distinct modes of exocytosis revealed by amperometry in neuroendocrine cells," *Biophys. J.*, vol. 100, no. 4, pp. 968–977, Feb. 2011.

[15] L. J. Mellander, R. Trouillon, M. I. Svensson and A. G. Ewing, "Amperometric post spike feet reveal most exocytosis is via extended kiss-and-run fusion," *Sci. Rep.*, vol. 2, no. 1, pp. 1–6, Nov. 2012.

[16] R. Trouillon and A. G. Ewing, "Actin controls the vesicular fraction of dopamine released during extended kiss and run exocytosis," *ACS Chem. Biol.*, vol. 9, no. 3, pp. 812–820, Mar. 2014.

[17] Q. Fang, K. Berberian, L. W. Gong, I. Hafez, J. B. Sørensen and M. Lindau, "The role of the C terminus of the SNARE protein SNAP-25 in fusion pore opening and a model for fusion pore mechanics," *Proc. Natl. Acad. Sci. U. S. A.*, vol. 105, no. 40, pp. 15388–15392, Oct. 2008.

[18] K. E. Larsen, Y. Schmitz, M. D. Troyer, E. Mosharov, P. Dietrich, A. Z. Quazi, M. Savalle, V. Nemani, F. A. Chaudhry, R. H. Edwards, L. Stefanis and D. Sulzer, "α-Synuclein overexpression in PC12 and chromaffin cells impairs catecholamine release by interfering with a late step in exocytosis," *J. Neurosci.*, vol. 26, no. 46, pp. 11915–11922, Nov. 2006.

[19] B. M. Manning, R. P. Hebbel, K. Gupta and C. L. Haynes, "Carbon-fiber microelectrode amperometry reveals sickle-cell-induced inflammation and chronic morphine effects on single mast cells," *ACS Chem. Biol.*, vol. 7, no. 3, pp. 543–551, Mar. 2012.

[20] A. S. Darvesh, R. T. Carroll, A. Bishayee, N. A. Novotny, W. J. Geldenhuys and C. J. Van Der Schyf, "Curcumin and neurodegenerative diseases: A perspective," *Expert Opinion on Investigational Drugs*, vol. 21, no. 8. Taylor & Francis, pp. 1123–1140, Aug-2012.

[21] X. Li, A. S. Mohammadi and A. G. Ewing, "Single cell amperometry reveals curcuminoids

modulate the release of neurotransmitters during exocytosis from PC12 cells," *J. Electroanal. Chem.*, vol. 781, pp. 30–35, Nov. 2016.

[22] R. M. Barbosa, C. F. Lourenço, R. M. Santos, F. Pomerleau, P. Huettl, G. A. Gerhardt and J. Laranjinha, "Chapter 20 In Vivo Real-Time Measurement of Nitric Oxide in Anesthetized Rat Brain," in *Methods in Enzymology*, vol. 441, Academic Press Inc., 2008, pp. 351–367.

[23] F. T. C. Moreira, M. G. F. Sale and M. Di Lorenzo, "Towards timely Alzheimer diagnosis: A self-powered amperometric biosensor for the neurotransmitter acetylcholine," *Biosens. Bioelectron.*, vol. 87, pp. 607–614, Jan. 2017.

[24] K. A. White, G. Mulberry, J. Smith, M. Lindau, B. Minch, K. Sugaya and B. N. Kim, "Single-Cell Recording of Vesicle Release from Human Neuroblastoma Cells using 1024-ch Monolithic CMOS Bioelectronics," *IEEE Trans. Biomed. Circuits Syst.*, vol. 12, no. 6, pp. 1345–1355, 2018.

[25] L. Colliver, J. Hess, N. Pothos, §david Sulzer and G. Ewing, *Quantitative and Statistical Analysis of the Shape of Amperometric Spikes Recorded from Two Populations of Cells*, vol. 74, no. 3. 2000, pp. 1086–1097.

[26] M. Huang, S. S. Rathore and M. Lindau, "Drug testing complementary metal-oxide-semiconductor chip reveals drug modulation of transmitter release for potential therapeutic applications," *J. Neurochem.*, vol. 151, no. 1, pp. 38–49, Oct. 2019.

[27] X. Liu, S. Barizuddin, W. Shin, C. J. Mathai, S. Gangopadhyay and K. D. Gillis, "Microwell device for targeting single cells to electrochemical microelectrodes for high-throughput amperometric detection of quantal exocytosis," *Anal. Chem.*, vol. 83, no. 7, pp. 2445–2451,

Apr. 2011.

[28]   J. Wang, R. Trouillon, J. Dunevall and A. G. Ewing, "Spatial resolution of single-cell exocytosis by microwell-based individually addressable thin film ultramicroelectrode arrays," *Anal. Chem.*, vol. 86, no. 9, pp. 4515–4520, May 2014.

[29]   L.-M. Li, W. Wang, S.-H. Zhang, S.-J. Chen, S.-S. Guo, O. Franc -Ais, J.-K. Cheng and W.-H. Huang, "Integrated Microdevice for Long-Term Automated Perfusion Culture without Shear Stress and Real-Time Electrochemical Monitoring of Cells," *Anal. Chem*, vol. 83, pp. 9524–9530, 2011.

[30]   A. Yakushenko, E. Kä Telhö and B. Wolfrum, "Parallel On-Chip Analysis of Single Vesicle Neurotransmitter Release," 2013.

[31]   N. Kasai, A. Shimada, T. Nyberg and K. Torimitsu, "An electrochemical sensor array and its application to real-time brain slice imaging," *Electron. Commun. Japan*, 2009.

[32]   J. Rothe, O. Frey, A. Stettler, Y. Chen and A. Hierlemann, "Fully Integrated CMOS Microsystem for Electrochemical Measurements on 32×32 Working Electrodes at 90 Frames Per Second," *Anal. Chem.*, vol. 86, no. 13, pp. 6425–6432, Jul. 2014.

[33]   D. L. Bellin, H. Sakhtah, Y. Zhang, A. Price-Whelan, L. E. P. P. Dietrich and K. L. Shepard, "Electrochemical camera chip for simultaneous imaging of multiple metabolites in biofilms," *Nat. Commun.*, vol. 7, no. 1, pp. 1–10, Jan. 2016.

[34]   B. N. Kim, A. D. Herbst, S. J. Kim, B. A. Minch and M. Lindau, "Parallel recording of neurotransmitters release from chromaffin cells using a 10×10 CMOS IC potentiostat array with on-chip working electrodes," *Biosens. Bioelectron.*, vol. 41, pp. 736–744, 2013.

[35]   J. K. Rosenstein, M. Wanunu, C. A. Merchant, M. Drndic and K. L. Shepard, "Integrated nanopore sensing platform with sub-microsecond temporal resolution," *Nat. Methods*, vol. 9, no. 5, pp. 487–492, Mar. 2012.

[36]   V. Viswam, J. Dragas, A. Shadmani, Y. Chen, A. Stettler, J. Muller and A. Hierlemann, "Multi-functional microelectrode array system featuring 59,760 electrodes, 2048 electrophysiology channels, impedance and neurotransmitter measurement units," *Dig. Tech. Pap. - IEEE Int. Solid-State Circuits Conf.*, vol. 59, pp. 394–396, 2016.

[37]   D. J. Bakkum, U. Frey, M. Radivojevic, T. L. Russell, J. Müller, M. Fiscella, H. Takahashi, A. Hierlemann, Y. Shu, A. Hasenstaub, A. Duque, Y. Yu, D. A. McCormick, H. Alle, J. R. Geiger, T. Sasaki, N. Matsuki, Y. Ikegaya, D. J. Bakkum *et al.*, "Tracking axonal action potential propagation on a high-density microelectrode array across hundreds of sites," *Nat. Commun.*, vol. 4, pp. 761–765, Jul. 2013.

[38]   J. Guo, W. Ng, J. Yuan, S. Li and M. Chan, "A 200-Channel Area-Power-Efficient Chemical and Electrical Dual-Mode Acquisition IC for the Study of Neurodegenerative Diseases," *IEEE Trans. Biomed. Circuits Syst.*, 2016.

[39]   J. S. Park, M. K. Aziz, S. Li, T. Chi, S. I. Grijalva, J. H. Sung, H. C. Cho and H. Wang, "1024-Pixel CMOS Multimodality Joint Cellular Sensor/Stimulator Array for Real-Time Holistic Cellular Characterization and Cell-Based Drug Screening," *IEEE Trans. Biomed. Circuits Syst.*, 2018.

[40]   T. Kuno, K. Niitsu and K. Nakazato, "Amperometric electrochemical sensor array for on-chip simultaneous imaging," in *Japanese Journal of Applied Physics*, 2014, vol. 53, no. 4

SPEC. ISSUE, p. 04EL01.

[41] W. Tedjo and T. Chen, "An Integrated Biosensor System with a High-Density Microelectrode Array for Real-Time Electrochemical Imaging," *IEEE Trans. Biomed. Circuits Syst.*, vol. 14, no. 1, pp. 20–35, Feb. 2020.

[42] J. Dragas, V. Viswam, A. Shadmani, Y. Chen, R. Bounik, A. Stettler, M. Radivojevic, S. Geissler, M. E. J. Obien, J. Müller and A. Hierlemann, "In Vitro Multi-Functional Microelectrode Array Featuring 59 760 Electrodes, 2048 Electrophysiology Channels, Stimulation, Impedance Measurement, and Neurotransmitter Detection Channels," *IEEE J. Solid-State Circuits*, 2017.

[43] M. Radivojevic, F. Franke, M. Altermatt, J. Müller, A. Hierlemann and D. J. Bakkum, "Tracking individual action potentials throughout mammalian axonal arbors," *Elife*, vol. 6, Oct. 2017.

[44] V. Vijay, B. Raziyeh, S. Amir, D. Jelena, B. J. Alicia, B. Axel, M. Jan, C. Yihui and H. Andreas, "High-density CMOS microelectrode array system for impedance spectroscopy and imaging of biological cells," in *2016 IEEE SENSORS*, 2016, pp. 1–3.

[45] D. Lonardoni, S. Di Marco, H. Amin, A. Maccione, L. Berdondini and T. Nieus, "High-density MEA recordings unveil the dynamics of bursting events in Cell Cultures," in *2015 37th Annual International Conference of the IEEE Engineering in Medicine and Biology Society (EMBC)*, 2015, vol. 2015, pp. 3763–3766.

[46] Michael L. A. V. Heien, and Michael A. Johnson and R. M. Wightman*, "Resolving Neurotransmitters Detected by Fast-Scan Cyclic Voltammetry," 2004.

[47]   D. L. Robinson, B. J. Venton, M. L. A. V Heien and R. M. Wightman, "Detecting subsecond dopamine release with fast-scan cyclic voltammetry in vivo.," *Clin. Chem.*, vol. 49, no. 10, pp. 1763–73, Oct. 2003.

[48]   K. T. Kawagoe, J. B. Zimmerman and R. M. Wightman, "Principles of voltammetry and microelectrode surface states," *J. Neurosci. Methods*, vol. 48, no. 3, pp. 225–240, Jul. 1993.

[49]   S. Ayers, K. D. Gillis, M. Lindau and B. A. Minch, "Design of a CMOS Potentiostat Circuit for Electrochemical Detector Arrays," *IEEE Trans. Circuits Syst. I Regul. Pap.*, vol. 54, no. 4, pp. 736–744, Apr. 2007.

[50]   J. Kim, K. Pedrotti and W. B. Dunbar, "An area-efficient low-noise CMOS DNA detection sensor for multichannel nanopore applications," *Sensors Actuators, B Chem.*, vol. 176, pp. 1051–1055, 2013.

[51]   K. A. White, G. Mulberry and B. N. Kim, "Rapid 1024-pixel Electrochemical Imaging at 10,000 Frames per Second using Monolithic CMOS Sensor and Multifunctional Data Acquisition System," *IEEE Sens. J.*, pp. 1–1, 2018.

[52]   J. Allen, "Photoplethysmography and its application in clinical physiological measurement," *Physiol. Meas.*, vol. 28, no. 3, pp. R1–R39, Mar. 2007.

[53]   A. K. Y. Wong, K.-P. Pun, Y.-T. Zhang and K. N. Leung, "A Low-Power CMOS Front-End for Photoplethysmographic Signal Acquisition With Robust DC Photocurrent Rejection," *IEEE Trans. Biomed. Circuits Syst.*, vol. 2, no. 4, pp. 280–288, Dec. 2008.

[54]   V. Rybynok, J. M. May, K. Budidha and P. A. Kyriacou, "Design and development of a novel multi-channel photoplethysmographic research system," in *2013 IEEE Point-of-Care*

Healthcare Technologies (PHT), 2013, pp. 267–270.

[55] M. Tavakoli, L. Turicchia and R. Sarpeshkar, "An Ultra-Low-Power Pulse Oximeter Implemented With an Energy-Efficient Transimpedance Amplifier," *IEEE Trans. Biomed. Circuits Syst.*, vol. 4, no. 1, pp. 27–38, Feb. 2010.

[56] J. K. Rosenstein, S. Ramakrishnan, J. Roseman and K. L. Shepard, "Single Ion Channel Recordings with CMOS-Anchored Lipid Membranes," *Nano Lett.*, vol. 13, no. 6, pp. 2682–2686, Jun. 2013.

[57] H. Li, S. Parsnejad, E. Ashoori, C. Thompson, E. K. Purcell and A. J. Mason, "Ultracompact Microwatt CMOS Current Readout With Picoampere Noise and Kilohertz Bandwidth for Biosensor Arrays," *IEEE Trans. Biomed. Circuits Syst.*, vol. 12, no. 1, pp. 35–46, Feb. 2018.

[58] E. Ashoori, S. Dávila-montero and A. J. Mason, "Compact and Low Power Analog Front End with in-situ Data Decimator for High-Channel-Count ECoG Recording," *Circuits Syst. (ISCAS), 2018 IEEE Int. Symp.*, vol. 2, pp. 6–10, 2018.

[59] C. I. Dorta-Quinones, M. Huang, J. C. Ruelas, J. Delacruz, A. B. Apsel, B. A. Minch and M. Lindau, "A Bidirectional-Current CMOS Potentiostat for Fast-Scan Cyclic Voltammetry Detector Arrays," *IEEE Trans. Biomed. Circuits Syst.*, vol. 12, no. 4, pp. 894–903, Aug. 2018.

[60] C.-Y. Wu, C.-C. Hsieh, F.-W. Jih, T.-P. Sun and S.-J. Yang, "A new share-buffered direct-injection readout structure for infrared detector," *Spie*, vol. 2020, no. Infrared Technology XIX, pp. 57–64, 1993.

[61] G. Mulberry, K. A. White and B. N. Kim, "Analysis of Simple Half-Shared Transimpedance

Amplifier for Picoampere Biosensor Measurements," *IEEE Trans. Biomed. Circuits Syst.*, vol. 13, no. 2, pp. 387–395, Apr. 2019.

[62] K. Niitsu, S. Ota, K. Gamo, H. Kondo, M. Hori and K. Nakazato, "Development of Microelectrode Arrays Using Electroless Plating for CMOS-Based Direct Counting of Bacterial and HeLa Cells," *IEEE Trans. Biomed. Circuits Syst.*, vol. 9, no. 5, pp. 607–619, Oct. 2015.

[63] J. Yao, X. A. Liu and K. D. Gillis, "Two approaches for addressing electrochemical electrode arrays with reduced external connections," *Anal. Methods*, vol. 7, no. 14, pp. 5760–5766, Jul. 2015.

[64] M. Huang, J. B. Delacruz, J. C. Ruelas, S. S. Rathore and M. Lindau, "Surface-modified CMOS IC electrochemical sensor array targeting single chromaffin cells for highly parallel amperometry measurements," *Pflügers Arch. - Eur. J. Physiol.*, vol. 470, no. 1, pp. 113–123, Jan. 2018.

[65] R. F. Lane and A. T. Hubbard, "Differential Double Pulse Voltammetry at Chemically Modified Platinum Electrodes for in vivo Determination of Catecholamines."

[66] J. O. Zerbino and M. G. Sustersic, "Ellipsometric and Electrochemical Study of Dopamine Adsorbed on Gold Electrodes," 2000.

[67] K. Berberian, K. Kisler, Q. Fang and M. Lindau, "Improved Surface-Patterned Platinum Microelectrodes for the Study of Exocytotic Events," *Anal. Chem.*, vol. 81, no. 21, pp. 8734–8740, Nov. 2009.

[68] O. Simoska, M. Sans, M. D. Fitzpatrick, C. M. Crittenden, L. S. Eberlin, J. B. Shear and K.

J. Stevenson, "Real-Time Electrochemical Detection of *Pseudomonas aeruginosa* Phenazine Metabolites Using Transparent Carbon Ultramicroelectrode Arrays," *ACS Sensors*, vol. 4, no. 1, pp. 170–179, Jan. 2019.

[69]   J. Elliott, O. Simoska, S. Karasik, J. B. Shear and K. J. Stevenson, "Transparent Carbon Ultramicroelectrode Arrays for the Electrochemical Detection of a Bacterial Warfare Toxin, Pyocyanin," *Anal. Chem.*, vol. 89, no. 12, pp. 6285–6289, Jun. 2017.

[70]   S. Shekar, D. J. Niedzwiecki, C.-C. Chien, P. Ong, D. A. Fleischer, J. Lin, J. K. Rosenstein, M. Drndić and K. L. Shepard, "Measurement of DNA Translocation Dynamics in a Solid-State Nanopore at 100 ns Temporal Resolution," *Nano Lett.*, vol. 16, no. 7, pp. 4483–4489, Jul. 2016.

[71]   J. Dunlop, M. Bowlby, R. Peri, D. Vasilyev and R. Arias, "High-throughput electrophysiology: an emerging paradigm for ion-channel screening and physiology," *Nat. Rev. Drug Discov.*, vol. 7, no. 4, pp. 358–368, Apr. 2008.

[72]   D. A. Borton, M. Yin, J. Aceros and A. Nurmikko, "An implantable wireless neural interface for recording cortical circuit dynamics in moving primates.," *J. Neural Eng.*, vol. 10, no. 2, p. 026010, Apr. 2013.

[73]   Y. Chen, E. Yao and A. Basu, "A 128-Channel Extreme Learning Machine-Based Neural Decoder for Brain Machine Interfaces," *IEEE Trans. Biomed. Circuits Syst.*, vol. 10, no. 3, pp. 679–692, Jun. 2016.

[74]   V. W. Leung, J. Lee, S. Li, S. Yu, C. Kilfovle, L. Larson, A. Nurmikko and F. Laiwalla, "A CMOS Distributed Sensor System for High-Density Wireless Neural Implants for Brain-

Machine Interfaces," in *ESSCIRC 2018 - IEEE 44th European Solid State Circuits Conference (ESSCIRC)*, 2018, pp. 230–233.

[75] W. Zheng, R. Liu, M. Zhang, G. Zhuang and T. Yuan, "Design of FPGA based high-speed data acquisition and real-time data processing system on J-TEXT tokamak," *Fusion Eng. Des.*, vol. 89, no. 5, pp. 698–701, May 2014.

[76] C. Yang, W. Zheng, M. Zhang, T. Yuan, G. Zhuang and Y. Pan, "A Real-Time Data Acquisition and Processing Framework Based on FlexRIO FPGA and ITER Fast Plant System Controller," *IEEE Trans. Nucl. Sci.*, 2016.

[77] J. P. Grinias, J. T. Whitfield, E. D. Guetschow and R. T. Kennedy, "An Inexpensive, Open-Source USB Arduino Data Acquisition Device for Chemical Instrumentation HHS Public Access," *J Chem Educ July*, vol. 12, no. 937, pp. 1316–1319, 2016.

[78] F. J. Ferrero Martín, M. Valledor Llopis, J. C. Campo Rodríguez, J. R. Blanco González and J. Menéndez Blanco, "Low-cost open-source multifunction data acquisition system for accurate measurements," *Measurement*, vol. 55, pp. 265–271, Sep. 2014.

[79] J. P. Kinney, J. G. Bernstein, A. J. Meyer, J. B. Barber, M. Bolivar, B. Newbold, J. Scholvin, C. Moore-Kochlacs, C. T. Wentz, N. J. Kopell and E. S. Boyden, "A direct-to-drive neural data acquisition system," *Front. Neural Circuits*, vol. 9, p. 46, Sep. 2015.

[80] R. Rajpal, H. Mandaliya, J. Patel, P. Kumari, P. Gautam, V. Raulji, P. Edappala, H. . Pujara and R. Jha, "Embedded multi-channel data acquisition system on FPGA for Aditya Tokamak," *Fusion Eng. Des.*, vol. 112, pp. 964–968, Nov. 2016.

[81] H. Xicoy, B. Wieringa and G. J. M. Martens, "The SH-SY5Y cell line in Parkinson's disease

research: a systematic review," *Mol. Neurodegener.*, vol. 12, no. 1, p. 10, Dec. 2017.

[82] S. J. Chinta and J. K. Andersen, "Dopaminergic neurons," *Int. J. Biochem. Cell Biol.*, vol. 37, no. 5, pp. 942–946, May 2005.

[83] R. Sarpeshkar, T. Delbruck and C. A. Mead, "White noise in MOS transistors and resistors," *IEEE Circuits Devices Mag.*, vol. 9, no. 6, pp. 23–29, Nov. 1993.

[84] P. R. Kinget, "Device mismatch and tradeoffs in the design of analog circuits," *IEEE J. Solid-State Circuits*, vol. 40, no. 6, pp. 1212–1224, Jun. 2005.

[85] L.-Y. . Huang and E. Neher, "Ca2+-Dependent Exocytosis in the Somata of Dorsal Root Ganglion Neurons," *Neuron*, vol. 17, no. 1, pp. 135–145, Jul. 1996.

[86] Z. Zhou and S. Misler, "Amperometric detection of stimulus-induced quantal release of catecholamines from cultured superior cervical ganglion neurons," *Proc. Natl. Acad. Sci.*, vol. 92, no. 15, 1995.

[87] S. Y. Yang, B. N. Kim, A. A. Zakhidov, P. G. Taylor, J.-K. Lee, C. K. Ober, M. Lindau and G. G. Malliaras, "Detection of Transmitter Release from Single Living Cells Using Conducting Polymer Microelectrodes," *Adv. Mater.*, vol. 23, no. 24, pp. H184–H188, Jun. 2011.

[88] P. Chen, B. Xu, N. Tokranova, X. Feng, J. Castracane and K. D. Gillis, "Amperometric detection of quantal catecholamine secretion from individual cells on micromachined silicon chips," *Anal. Chem.*, vol. 75, no. 3, pp. 518–524, 2003.

[89] W. F. Gillis, C. A. Lissandrello, J. Shen, B. W. Pearre, A. Mertiri, F. Deku, S. Cogan, B. J.

Holinski, D. J. Chew, A. E. White, T. M. Otchy and T. J. Gardner, "Carbon fiber on polyimide ultra-microelectrodes," *J. Neural Eng.*, vol. 15, no. 1, p. 016010, 2018.

[90] S. Barizuddin, X. Liu, J. C. Mathai, M. Hossain, K. D. Gillis and S. Gangopadhyay, "Automated targeting of cells to electrochemical electrodes using a surface chemistry approach for the measurement of quantal exocytosis," *ACS Chem. Neurosci.*, vol. 1, no. 9, pp. 590–597, 2010.

[91] D. J. Fischer, M. K. Hulvey, A. R. Regel and S. M. Lunte, "Amperometric detection in microchip electrophoresis devices: Effect of electrode material and alignment on analytical performance," *Electrophoresis*, vol. 30, no. 19, pp. 3324–3333, 2009.

[92] A. Sen, S. Barizuddin, M. Hossain, L. Polo-Parada, K. D. Gillis and S. Gangopadhyay, "Preferential cell attachment to nitrogen-doped diamond-like carbon (DLC:N) for the measurement of quantal exocytosis," *Biomaterials*, vol. 30, no. 8, pp. 1604–1612, 2009.

[93] X. Sun and K. D. Gillis, "On-chip amperometric measurement of quantal catecholamine release using transparent indium tin oxide electrodes," *Anal. Chem.*, vol. 78, no. 8, pp. 2521–2525, 2006.

[94] S. Ayers, K. Berberian, K. D. Gillis, M. Lindau and B. A. Minch, "Post-cmos fabrication of working electrodes for on-chip recordings of transmitter release," *IEEE Trans. Biomed. Circuits Syst.*, vol. 4, no. 2, pp. 86–92, 2010.

[95] K. D. Gillis, X. A. Liu, A. Marcantoni and V. Carabelli, "Electrochemical measurement of quantal exocytosis using microchips," *Pflügers Arch. - Eur. J. Physiol.*, vol. 470, no. 1, pp. 97–112, Jan. 2018.

[96] K. Berberian, K. Kisler, Q. Fang and M. Lindau, "Improved Surface-Patterned Platinum Microelectrodes for the Study of Exocytotic Events," *Anal. Chem.*, vol. 81, no. 21, pp. 8734–8740, Nov. 2009.

[97] K. D. Kozminski, D. A. Gutman, V. Davila, A. David Sulzer and A. G. Ewing, "Voltammetric and Pharmacological Characterization of Dopamine Release from Single Exocytotic Events at Rat Pheochromocytoma (PC12) Cells," vol. 70, no. 15, pp. 3123–3130, 1998.

[98] R. M. Wightman, T. J. Schroeder, J. M. Finnegan, E. L. Ciolkowski and K. Pihel, "Time course of release of catecholamines from individual vesicles during exocytosis at adrenal medullary cells," *Biophys. J.*, vol. 68, no. 1, pp. 383–390, Jan. 1995.

[99] J. Abbott, T. Ye, K. Krenek, L. Qin, Y. Kim, W. Wu, R. Gertner, H. Park and D. Ham, "The Design of a CMOS Nanoelectrode Array With 4096 Current-Clamp/Voltage-Clamp Amplifiers for Intracellular Recording/Stimulation of Mammalian Neurons," *IEEE J. Solid-State Circuits*, vol. 55, no. 9, pp. 2567–2582, 2020.

[100] C. P. Grabner and D. Zenisek, "Amperometric resolution of a prespike stammer and evoked phases of fast release from retinal bipolar cells," *J. Neurosci.*, vol. 33, no. 19, pp. 8144–8158, May 2013.

[101] T. L. Colliver, S. J. Pyott, M. Achalabun and a G. Ewing, "VMAT-Mediated changes in quantal size and vesicular volume.," *J. Neurosci.*, vol. 20, no. 14, pp. 5276–82, 2000.

[102] R. H. S. Westerink, A. De Groot and H. P. M. Vijverberg, "Heterogeneity of catecholamine-containing vesicles in PC12 cells," *Biochem. Biophys. Res. Commun.*, vol. 270, no. 2, pp.

625–630, Apr. 2000.

[103] Y. Dong, G. Ning, A. G. Ewing and M. L. Heien, "Pituitary Adenylate Cyclase Activating Polypeptide Modulates Catecholamine Storage and Exocytosis in PC12 Cells," *PLoS One*, vol. 9, no. 3, p. e91132, Mar. 2014.

[104] L. A. Sombers, M. M. Maxson and A. G. Ewing, "Loaded dopamine is preferentially stored in the halo portion of PC12 cell dense core vesicles," *J. Neurochem.*, vol. 93, no. 5, pp. 1122–1131, Apr. 2005.

[105] L. W. Gong, I. Hafez, G. Alvarez de Toledo and M. Lindau, "Secretory vesicles membrane area is regulated in tandem with quantal size in chromaffin cells," *J. Neurosci.*, vol. 23, no. 21, pp. 7917–7921, Aug. 2003.

[106] L. A. Sombers, H. J. Hanchar, T. L. Colliver, N. Wittenberg, A. Cans, S. Arbault, C. Amatore and A. G. Ewing, "The Effects of Vesicular Volume on Secretion through the Fusion Pore in Exocytotic Release from PC12 Cells," *J. Neurosci.*, vol. 24, no. 2, pp. 303–309, Jan. 2004.

[107] A. Elhamdani, M. E. Brown, C. R. Artalejo and H. C. Palfrey, "Enhancement of the dense-core vesicle secretory cycle by glucocorticoid differentiation of PC12 cells: Characteristics of rapid exocytosis and endocytosis," *J. Neurosci.*, vol. 20, no. 7, pp. 2495–2503, Apr. 2000.

[108] K. Kisler, B. N. Kim, X. Liu, K. Berberian, Q. Fang, C. J. Mathai, S. Gangopadhyay, K. D. Gillis and M. Lindau, "Transparent Electrode Materials for Simultaneous Amperometric Detection of Exocytosis and Fluorescence Microscopy," *J. Biomater. Nanobiotechnol.*, vol. 03, no. 02, pp. 243–253, May 2012.

[109] I. Hafez, K. Kisler, K. Berberian, G. Dernick, V. Valero, M. G. Yong, H. G. Craighead and M. Lindau, "Electrochemical imaging of fusion pore openings by electrochemical detector arrays," *Proc. Natl. Acad. Sci. U. S. A.*, vol. 102, no. 39, pp. 13879–13884, Sep. 2005.

[110] E. O. Neftci, B. U. Pedroni, S. Joshi, M. Al-Shedivat and G. Cauwenberghs, "Stochastic synapses enable efficient brain-inspired learning machines," *Front. Neurosci.*, vol. 10, no. JUN, pp. 1–16, 2016.

[111] J. P. Hayes, "Introduction to stochastic computing and its challenges," *Proc. - Des. Autom. Conf.*, vol. 2015-July, no. c, pp. 2–4, 2015.

[112] S. T. Keene, C. Lubrano, S. Kazemzadeh, A. Melianas, Y. Tuchman, G. Polino, P. Scognamiglio, L. Cinà, A. Salleo, Y. van de Burgt and F. Santoro, "A biohybrid synapse with neurotransmitter-mediated plasticity," *Nat. Mater.*, vol. 19, no. 9, pp. 969–973, Sep. 2020.

[113] B. Wiatrak, A. Kubis-Kubiak, A. Piwowar and E. Barg, "PC12 Cell Line: Cell Types, Coating of Culture Vessels, Differentiation and Other Culture Conditions," *Cells*, vol. 9, no. 4, Apr. 2020.

[114] K. A. White and B. N. Kim, "Quantifying neurotransmitter secretion at single-vesicle resolution using high-density complementary metal–oxide–semiconductor electrode array," *Nat. Commun.*, vol. 12, no. 1, pp. 1–8, Dec. 2021.

[115] K. A. White, G. Mulberry and B. N. Kim, "Parallel 1024-ch Cyclic Voltammetry on Monolithic CMOS Electrochemical Detector Array," *IEEE Sens. J.*, vol. 20, no. 8, pp. 4395–4402, Apr. 2020.

[116] M. Alawad and M. Lin, "Survey of stochastic-based computation paradigms," *IEEE Transactions on Emerging Topics in Computing*, vol. 7, no. 1. IEEE Computer Society, pp. 98–114, Jan-2019.

[117] M. Alawad and M. Lin, "Stochastic-Based Deep Convolutional Networks with Reconfigurable Logic Fabric," *IEEE Trans. Multi-Scale Comput. Syst.*, vol. 2, no. 4, pp. 242–256, Oct. 2016.